UNIVERSITY OF PUERTO RICO

RIO PIEDRAS CAMPUS

STUDIES ON MULTIFUNCTIONAL MATERIALS APPLIED TO ENERGY STORAGE

By

Ivan W. Castillo Cisneros

Submitted in Partial Fulfillment of the Requirements for the Degree of

DOCTOR OF PHILOSOPHY IN CHEMICAL PHYSICS

Supervised by

Professor Ram S. Katiyar

Department of Physics

College of Natural Science

University of Puerto Rico

San Juan, PR, USA

July 31, 2023

STUDY OF MULTIFUNCTIONAL MATERIALS APPLIED TO ENERGY STORAGE

ACCEPTED BY FACULTY OF THE CHEMICAL PHYSICS PROGRAM, OF THE UNIVERSITY OF THE UNIVERSITY OF PUERTO RICO, RIO PIEDRAS CAMPUS. IN PARTIAL FULFILLMENT OF THE REQUIREMENTS FOR THE DEGREE OF DOCTOR OF PHYLOSOPHY IN CHEMICAL PHYSISCS.

_____

Dr. Ram S. Katiyar

Department of Physics

THESIS ADVISOR

_____

Dr. Gerardo Morell Marrero

Department of Physics

THESIS COMMITTEE MEMBER

_____

Dr. Marvin J. Bayro

Department of Chemistry

THESIS COMMITTEE MEMBER

Abstract

Structure, phonon, and energy storage density in Sr^{2+}-substituted lead-free ferroelectric $Ba_{1-x}Sr_xTiO_3$ (BST_x) for compositions x= 0.1, 0.3, and 0.7 were investigated using X-ray diffraction, Raman, and ferroelectric polarization measurements as a function of temperature. The samples were tetragonal for x = 0.1 with a large c/a ratio. The tetragonal anisotropy was decreased upon increasing x and transforming to cubic for x = 0.7. The changes in structural and ferroelectric properties were found to be related to the c/a ratios. The temperature-dependent phonon spectroscopy results indicated a decrease in tetragonal-cubic phase transition temperature, Tc, upon increasing x due to a reduction in the lattice anisotropy. The intensity of ~303 cm^{-1} E(TO2) mode decreased gradually with temperature and that finally disappeared around the tetragonal ferroelectric to cubic paraelectric phase at about 100 ℃ and 70 ℃ for x = 0.1 and 0.3, respectively. A gradual reduction in the band gap E_g of BST_x with x was evident from the analysis of UV-Visible absorption spectra. The energy storage density (U_{dis}) of the ferroelectric capacitors for x = 0.7 was ~0.20 J/cm^3 with an energy storage efficiency of ~88% at an applied electric field of 104.6 kV/cm. Nearly room temperature transition temperatures T_C and reasonably fair energy storage density of the BST_x capacitors were found.

The energy storage density of these thin film capacitors was estimated using the measured polarization hysteresis loops and were compared. For x = 0.7, a larger energy storage density (U_{re}) ~29 J/cm^3 with efficiency of ~48 % was estimated at an applied voltage of 1.1 MV/cm. Nearly room temperature transition temperature T_c, larger dielectric constant, and high energy density values of our BST_x thin film capacitors indicate its possible application in high energy storage devices.

In this study we are reporting electrochemical performance of $Ba_{0.9}Sr_{0.1}TiO_3$ (BST) having polarization of 14.58 μC/cm^2 doped sulfur/carbonblack/polyvinylidenefluoride(S/BST/CB/PVDF) composite as cathode materials for Li-S batteries. The performance of fabricated cathodes in terms of structural, electronic, morphological, and electrochemical response have been tested at various concentrations of BST doping. Considering that polar substances have good affinity towards polysulfide and can provide a more stable reacting environment in the cathodic site, trapping polysulfide intermediates via induced permanent dielectric polarizability. It is expected that spontaneous polarization induced by asymmetric crystal structure of ferroelectrics provide internal electric fields and increase chemisorption with heteropolar reactivity. X-ray diffraction spectra confirms tetragonal symmetry (c/a=1.0073), Raman spectroscopic study confirms Raman modes ($A_1(TO_1)$, $A_1(TO_2)$, $A_1(TO_3)$ and $A_1(LO_3)$) of the tetragonal orientation for BST modified composites. All the compositional cations are observed from SEM images confirm homogeneous distribution of BST in the sulfur cathode system having grain sizes (1-1.5 μm) which is based on microscopic analysis. BST coupled C-S composite cathodes improve the electrochemical performance in comparison with the cathodes composed of C-S. The high capacity for S/BST/CB/PVDF composites of the order of 820 mAh/g @ 100 mA/g have been achieved for the $S_{50}BST_{30}CB_{10}PVDF_{10}$ composite cathode and very stable response till 100th cycles attributes polysulfide migration is effectively reducing due to ferroelectric particles doping in the composite cathode. Two plateaus were observed in between 2.3V to 2.0 V and 2.0 V to 1.5 V in the charge/discharge characteristics and high cyclic stability substantiate the superior performance of the designed ferroelectric nanoparticles doped S/CB composite cathode materials due to the efficient reduction in the polysulfide shuttle effect in these

composite cathodes. In this study we are reporting the electrochemical performance of $Ba_{0.9}Sr_{0.1}TiO_3$ (BST) having polarization of 14.58 $\mu C/cm^2$ as an anode for Li-ion batteries. Perovskite structure (ABO_3) anode materials have received much attention because of their mixed electronic and ionic conduction behaviours that make the triple-phase boundary (TPB) extend to the entirely exposed anode surface. Among the variety of these oxides, $SrTiO_3$-based perovskite compounds are promising Ni-free anode candidates due to their high chemical stability at high temperatures under both oxidizing and reducing atmospheres, and strong resistance to carbon deposition. X-ray diffraction spectra confirm tetragonal symmetry (c/a=1.0073), Raman spectroscopic study confirms Raman modes ($A_1(TO_1)$, $A_1(TO_2)$, $A_1(TO_3)$ and $A_1(LO_3)$) of the tetragonal orientation for BST. SEM images confirm homogeneous surface of BST having grain sizes (1-1.5 μm). Carbon black was used as the conductive additive PVDF as binder, $LiPF_6$ as an electrolyte for charge-discharge performance and contribution to the electrochemical properties of the cell in terms of lithium intercalation and de-intercalation. At slow discharge rate, a capacity of approximately 240 mAh g^{-1} achieved. It is found that Ba on $SrTiO_3$ surface helps to facilitate electron transfer thereby improving the capacity and rate performance of BST as Li-ion battery anode material. These results show us that the BST is applicable for the development of lithium-ion batteries. For improving the negative electrode of lithium metal has serious problems as secondary battery use, since it does not have a long enough cyclic life and their safety aspects that need to be considered due to the dendrite formation on the surface of lithium metal electrode during charge/discharge cycles. To solve these problems a locking-chair concept has established, in which the intercalation phenomena has used as an anode reaction for lithium-ion secondary batteries.

Acknowledgements

Grateful for all the support and assistance I have received in my graduate studies. First, I would like to express my sincere thanks to my supervisor, Dr. Ram S. Katiyar, for his continuous support, teaching, dedication and for always believing in me, thank you very much. I also want to thank my tutors in this and other projects, Dr. Karuna K. Mishra, and Dr. Balram Tripathi, for instilling in me an unreserved interest in research, for your friendship and guidance, I am forever grateful. My research partner, Dr. Danilo Barrionuevo, was instrumental in defining the path of my research. To my friend Jencarlos del Valle, for his unconditional help in the experiments, and to all my colleagues at the SPECLAB laboratory, for their support.

I am grateful to all those with whom I have had the pleasure of working on this and related projects. A special thanks to William Perez, laboratory technician, for his passion for our shared laboratory and research facilities and for his constant encouragement. My most sincere thanks also to Dr. Marvin J. Bayro and Dr. Gerardo Morell, who gave me the opportunity to grow beyond being a researcher in science.

I also want to thank my parents and siblings, whose support was unconditional throughout this process. That thanks to your constant support it was possible to achieve the goal.

This work would not have been possible without the financial support of Department of Defense, USA (DoD Grant No. #FA9550-20-1-0064) and PR NASA EPSCoR Research Infrastructure Development (Award No. # 80NSSC22M0025).

“I dedicate this thesis to my father, mother, and brothers, who with love and effort have accompanied me in this process, without hesitating at any moment of seeing my dreams come true, which are also their dreams”.

Table of contents

CHAPTER 2

Experimental methods and characterization techniques

CHAPTER 3

Phase transition and energy storage density in lead-free ferroelectric $Ba_{1-x}Sr_xTiO_3$ (x = 0.1, 0.3, and 0.7) capacitor

CHAPTER 4

Control of polysulfide shuttle: An approach via ferroelectric ($Ba_{0.9}Sr_{0.1}TiO_3$) nanoparticles doped sulfur cathode for high-capacity Li-S batteries.

CHAPTER 5

Switchable macroscopic polarization ($Ba_{0.9}Sr_{0.1}TiO_3$) induced polysulfides adsorption in sulfur cathode for high energy density Li-S batteries.

CHAPTER 6

Highlights and perspective

List of figures

List of tables

PUBLICACION AND PRESENTATIONS

PUBLICATIONS

1. B. Tripathi, C.C.Z. Gomez, **Ivan Castillo**, R. Katiyar, G. Morel, B. Weiner, Ram S. Katiyar. Bi_2O_3 Intercalated SWCNT/Sulphur (S) Composite Electrodes for Stable & High-Performance Li-S Battery. *(Under review)*
2. **Ivan Castillo**, B. Tripathi, R. Katiyar, V. Dorvilien, Danilo B. Diestra, Karuna K. Mishra, J. Rivera Del Valle, G. Morel and Ram S. Katiyar. Control of polysulfide shuttle: An approach via ferroelectric ($Ba_{0.9}Sr_{0.1}TiO_3$) nanoparticles doped sulfur cathode for high-capacity Li-S batteries. *(Under review)*.
3. **Ivan Castillo**, B. Tripathi, R. Katiyar, V. Dorvilien, Danilo B. Diestra, Karuna K. Mishra, J. Rivera Del Valle, G. Morel and Ram S. Katiyar. Switchable macroscopic polarization ($Ba_{0.9}Sr_{0.1}TiO_3$) induced polysulfides adsorption in sulfur cathode for high energy density Li-S batteries. *(Under review)*.
4. A. Luis Matos, Tej B. Limbu, **Ivan Castillo,** M**.** Shehzad Sultan, Balram Tripathi, Ram S. Katiyar, Brad R. Weiner, and Gerardo Morell. Optimization of graphene layers grown on Pt/Ti/SiO_2 by hot filament chemical vapor deposition. Macromolecular Symposia xxx, xxx (2023).
5. **Ivan Castillo**, Karuna K. Mishra, and Ram S. Katiyar. Phase Transition and Energy Storage Density in Lead-Free Ferroelectric $Ba_{1-x}Sr_xTiO_3$ (x=0.1, 0.3, and 0.7) capacitor. *Crystals* **13,** 630(2023).

6. **Ivan Castillo**, Karuna K. Mishra, and Ram S. Katiyar. Characterization of V_2O_3 Nanoscale Thin Films Prepared by DC Magnetron Sputtering Technique. *Coating*, **12**, 649(2022).

PRESENTATIONS

1. **Ivan Castillo**, B. Tripathi, J. Del Valle, K.K. Mishra, G. Morel, and R.S. Katiyar. Ba-Doped $SrTiO_3$ ($Ba_{0.9}Sr_{0.1}TiO_3$) Perovskite with Superior Polarization as Anode Material for Li-Ion Batteries. *CARIBMAT 2023*, PR, Oct. 18-21, 2023.
2. B. Tripathi, C.C. Zuluaga Gomez, **Ivan Castillo,** R. Katiyar, and R. S. Katiyar. Bi_2O_3 Intercalated SWCNT/Sulphur (S) Composite Electrodes for Stable & High-Performance Li-S Batteries. *243rd ECS Meeting*, Boston, MA, May. 28-Jun. 2, 2023.
3. **Ivan Castillo**, K. K Mishra, and Ram S. Katiyar. Ferroelectric ordering and electrical energy storage in lead-free ferroelectric $Ba_{1-x}Sr_xTiO_3$ capacitor. *Pan America Ceramics Congress and Ferroelectric Meetings of Americas (PACC-FMAS)*, Panama, July 24-28, 2022.
4. **Ivan Castillo**, K. K Mishra, and Ram S. Katiyar. Studies on Electrical Storage Density in Lead-Free Ferroelectric $Ba_{1-x}Sr_xTiO_3$ (x=0.1, 0.3, and 0.7) Capacitors. *241st ECST Meeting*, Canada, Vancouver, May. 29-Jun. 2, 2022.
5. **Ivan Castillo**, K. K Mishra, and Ram S. Katiyar. Thin Films Deposition and Energy Storage Density in Lead-Free Ferroelectric $Ba_{1-x}Sr_xTiO_3$ (x = 0.1, 0.3, 0.7) Thin Film Capacitors. *241st ECST Meeting*, Canada, Vancouver, May. 29-Jun. 2, 2022.
6. Karuna K. Mishra, **Ivan Castillo,** and Ram Katiyar. Room temperature $0.55Pb(Zr_{0.52}Ti_{0.48})O_3$-$0.45Pb(Fe_{0.67}W_{0.33})O_3$ Nanoscale Multiferroic Thin Films

Prepared by Pulsed Laser Deposition Technique. *Materials Research Society Fall Meeting*, Boston, MA, Nov. 30-Dec. 7, 2021.

7. **Ivan Castillo**, K. Karuna Mishra, Ram S. Katiyar. Energy storage density in lead-free ferroelectric $Ba_x - Sr_{1-x}TiO_3$ thin films capacitor prepared using pulsed laser deposition technique. *International Conference on Advances in Functional Materials,* Los Angeles, CA, Aug. 18-20, 2021.
8. K. K. Mishra, **Ivan Castillo**, Ram S. Katiyar. Ferroelectricity and Enhance Energy Storage Density in $0.70Pb(Zr_{0.52}TiO_{0.48})O_3 - 0.30Pb(Fe_{0.5}Nb_{0.5})O_3$ Nanoscale Ferroelectric Thin Film Prepared by Pulsed Laser Deposition Technique. *Materials Research Society Spring Meeting*, Boston, MA, Apr. 17-23, 2021.
9. **Ivan Castillo**, K. K. Mishra, Ram S. Katiyar. Metal-Insulator phase transition and spin ordering in Nanoscale V_2O_3 films. *International Congress of the Dominican Society of Physics (CI-SoDoFi-2021)*, Santo Domingo, Dominican Republic, Jan. 18-22, 2021.
10. **Ivan Castillo** and Ram S. Katiyar. X-ray Photoelectron Spectroscopy (XPS). *Seminar of the Department of Natural Sciences (UPR-RP)*, San Juan, PR, May 25-27, 2018.

POSTER PRESENTATION:

1. **Ivan Castillo**, K. K. Mishra, V. Dorvilien, B. Tripathi, J. Rivera Del Valle, R. Katiyar, and R.S. Katiyar. Lead-Free Ferroelectric $Ba_{0.9}Sr_{0.1}TiO_3$ Coupled Polysulfide Trapping on Sulfur Cathode in Stable and High Energy Density Lithium-Sulfur (Li-S) Batteries. *243rd ECS Meeting*, Boston, MA, May. 28-Jun. 2, 2023.
2. R. Katiyar, C.C. Zuluaga, **Ivan Castillo,** B. Tripathi, G. Morell, B.R. Weiner, and R.S. Katiyar. Cqds@S/SWCNTS Composite Cathodes and Ferroelectric Coated Separator an

Accelerating Agent of Li- Ions for High Performance Li-S Batteries. *243rd ECS Meeting*, Boston, MA, May. 28-Jun. 2, 2023.

3. **Ivan Castillo**, Karuna K. Mishra, and Ram Katiyar. Nanoscale V_2O_3 films prepared by magnetron DC sputtering: Metal-Insulator phase transition and magnetic ordering. *Materials Research Society Fall Meeting*, Boston, MA, Dec. 1-7, 2019.

CHAPTER 1

(Ba, Sr) TiO_3: Ferroelectric material and applications

1.1 Introduction

Ferroelectricity is defined as the spontaneous alignment of electric dipoles by their mutual interaction, which show polarization even without an external applied electric field. Also, a ferroelectric may be formally defined as a pyroelectric material that has a reversible, or switchable, polarization.[1] Property presented by non-centromeric crystals (21 classes), but they exhibit a great variety of physical properties of technological importance (Energy Storage).[2] These classes may have several polar axes, which make it possible to show piezoelectric effects. Ferroelectric materials are one branch of pyroelectric materials. When an external electric field is applied on the ferroelectric crystal, it can reverse the spontaneous polarization of the sample. Thus, only from crystalline characterization view, one cannot be sure with the ferroelectric materials. For the phenomenon of reversing spontaneous polarization, the experiment result will show it as a hysteresis loop. The shape of this hysteresis loop is quite like that of ferromagnetic materials.[3] For example Perovskites ferroelectric materials (ABO_3), such as barium strontium titanate ($Ba_{1-x}Sr_xTiO_3$) have been extensively investigated because of their interesting ferroelectric properties, the structure-properties relationships.[4] The importance of ferroelectric (lead-free) materials in recent research on sustainable energy. It requires the design and development of new materials for their applications in energy storage devices such as dielectric capacitors and batteries.

The dielectric capacitor continues to store energy even when it is disconnected from its charging circuit, a feature that allows it to be used in rechargeable energy storage systems, which has been widely used in high power and pulsed power systems. It has the advantages of high-power density and long-life cycle, but with the disadvantage of low power density and large dissipation, which contrasts with batteries, which have high energy density but low power density. [5,6] In the process of maximizing the maximum charge that a capacitor can store; the material must have the following properties: high permittivity and high dielectric breakdown voltage. Currently, commercial dielectric for high-power applications is dominated by polymers or ceramics, which usually exhibit a limited energy density of less than 2 J cm^{-3}.[7] For example, the latest generation metallized film capacitor only offers an energy density limit of 1-2 Jcm^{-3} using biaxially oriented polypropylene as the dielectric. Research has currently focused on the design of materials and processes for the manufacture of capacitors, but with limited success, in the challenge of further increasing the energy density. Shows a perspective for the development of capacitors, taking advantage of various materials and manufacturing techniques. The characteristics of advanced projected capacitors should offer high voltage in the kV range, energy density of 15–30 J cm^{-3}, and discharge time of <1 μs to be competitive with supercapacitors.[8]

Among the different types of dielectrics that can be used to develop high energy density devices. In general ceramics exhibit high permittivity but low tensile strength while polymers and glass matrices have high breaking strength but low permittivity.[9] Other options are fuel cells (200-1000 Wh/Kg) and batteries (10-300 Wh/Kg), which offer high energy density, but both also offer low energy density power (500 W/Kg) due to the slow

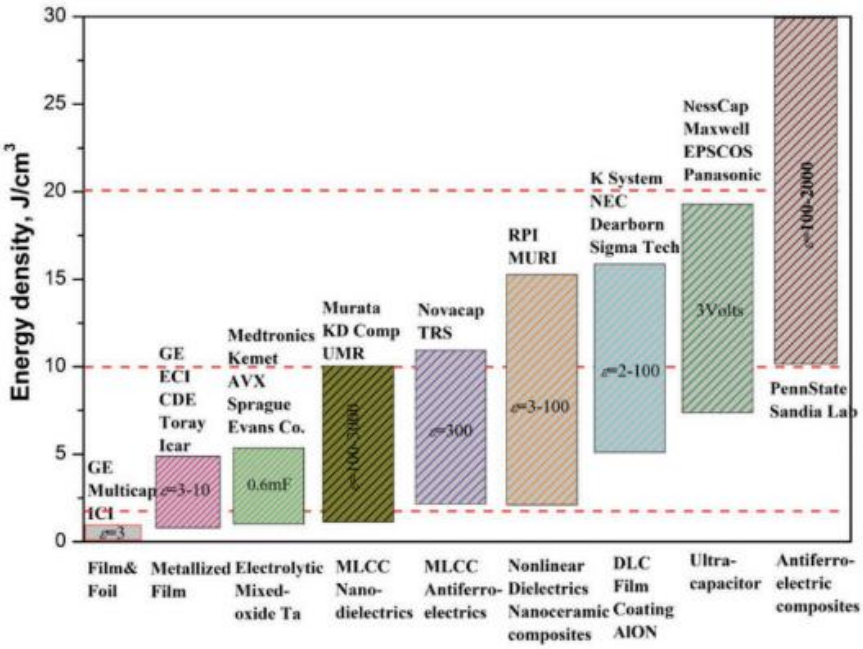

Figure 1.1. *Approaches to high-energy-density capacitor technology.[9]*

movement of their charge carriers, which limits their applications in many high-power systems. Electrochemical supercapacitors have moderate energy density (0.04-30 Wh/Kg) or high-power density (101-106 W/Kg), but they require long upload processes (second or even tens of seconds). Quite the opposite that occurs with dielectric capacitor, they have faster charge and discharge of the order of ~ns and a much higher power density up to 108 W/Kg, which meets the requirement for application in electronics systems of super high power, such as: hybrid electric vehicles, medical defibrillators, spacecraft, satellites, and electrical weapon system. But the potential applications of dielectric capacitor are severely limited by their low energy density, which is at least an order of magnitude lower than that of batteries, fuel cell, and electrochemical capacitor, as shown in figure 1.1. Dielectric capacitors are used in more than 25% of the volume and weight of power electronic as pulsed power system.[10] That is why it is urgent to improve the dielectric properties of

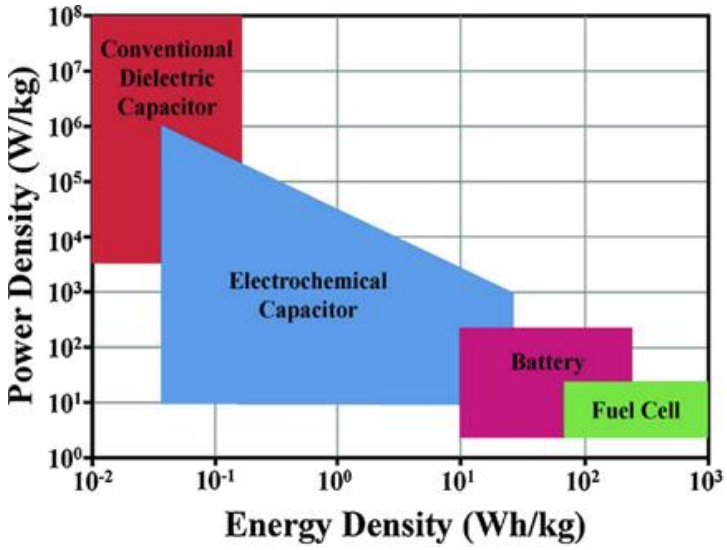

Figure 1.2 . *Representation of power density and function of energy density in different energy storage devices.[11]*

materials, to improve the energy density of dielectric capacitor. But what is important today is to find alternative lead-free dielectric materials with excellent energy storage properties. Although many relevant papers have been published, a comprehensive review of the current state of research on lead-free dielectric materials for energy storage applications does not exist to date. We focus here on recent progress in the development of various types of lead-free dielectric materials in the form of ceramics. We analyze the energy storage properties of these materials to improve guidance for the design of new lead-free dielectric materials whit high energy density and storage efficiency. In addition, new strategies are proposed to further improve the energy storage capacity of lead-free dielectric materials.

1.2 Barium strontium titanate

Ferroelectric materials exist in two phases: ferroelectric (polar) phase and paraelectric phase (nonpolar). All ferroelectrics have a perovskite structure (ABO_3) as show in Figure 1.3, where A and B are atoms with structure and can be occupied by Ba^{2+} and Sr^{2+} in the A-sites of the barium titanate lattice. Barium strontium titanate ($Ba_{1-x}Sr_xTiO_3$, BST_x) is a

continuous solid solution of $BaTiO_3$ (BTO) and $SrTiO_3$ (STO) over the entire range of concentration x. The high dielectric constant and conductivity of BST_x may be caused by the ionic displacement.[12] BST_x system only experiences an electronic displacement with the changing applied electric field. It can be seen from Figure 1.3 that the Ti ions are surrounded by six oxygen atoms.

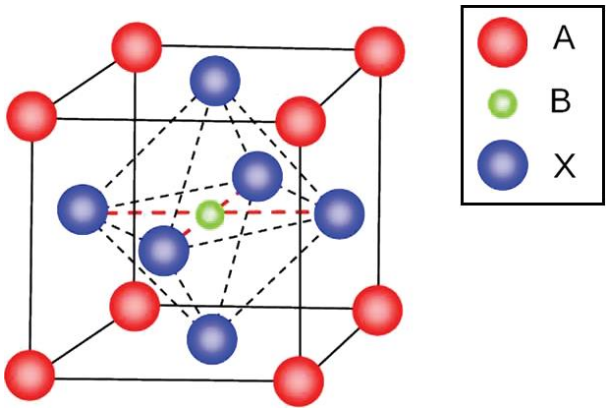

Figure 1.3. *Perovskite structure.[12]*

1.2.1 Structural properties of (Ba, Sr) TiO_3

The structure-property relationship in (Ba,Sr) TiO_3 compound with an ABO_3 perovskite-type structure has been well established in the literature. [13,14] Interesting ferroelectric ceramic compositions compound by BTO and STO are typical ferroelectric materials, but at room temperature STO is in the paraelectric state whit no apparent phase segregation. It is known that the Curie temperature (Tc) of BST_x can be varied by adjusting the Ba/Sr ratio. For phase shifting ceramics, it is desirable that the device in the paraelectric region of BTO is around 125 °C, while the transition temperature for ferroelectric state to paraelectric state hence the desire for low Tc for STO is around -233 °C. In BST_x system, the structure, dielectric and ferroelectric properties mainly depend on the Ba to Sr ratio.[14] According to Figure 1.4, the function of Curie temperature based on Ba/Sr ratio in bulk

BST_x is exhibited. As the Ba content increases, the Curie temperature of BST_x increases linearly. This means, the tetragonality of BST_x system increases with increasing Ba content. The Ba rich phases are ferroelectric and tetragonal at room temperature. It is reported that at room temperature BST is ferroelectric when the Ba content is over 65%. For example, at room temperature, the $Ba_{0.65}Sr_{0.35}TiO_3$ has the highest dielectric constant because its tetragonal to cubic transformation occurs approaching room temperature. And $Ba_{0.67}Sr_{0.33}TiO_3$ as the basic composition because of its combinations of low Tc, high dielectric constant.[13]

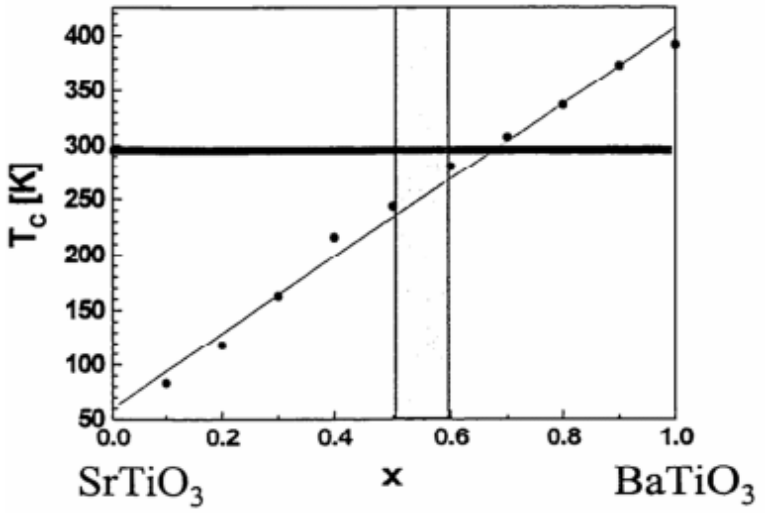

Figure 1.4. *Curie temperature (Tc) BST_x vs. composition. [13]*

The analysis of the lattice parameters (a and c) of the BST_x compound as a function of the amount of Sr at room temperature is given in Figure 1.5, a tetragonal structure for high Ba content is also shown, while the cubic structure is sample on the high Sr side. The transition from cubic to tetragonal occurs at around 0.3 of the STO content, which is consistent with the results of the dielectric test.[13]

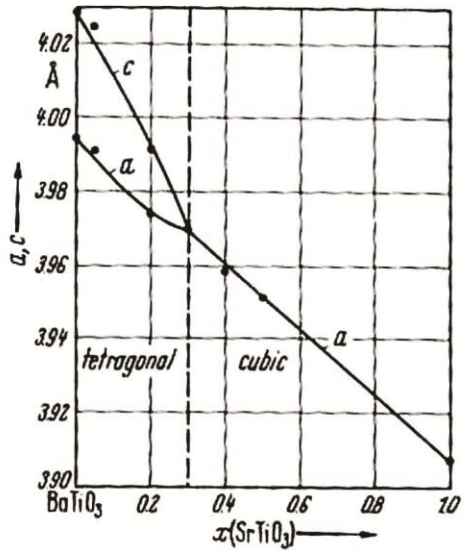

Figure 1.5. *Room Temperature (RT) lattice parameter of BST_x vs. composition.[13]*

Figure 1.6 shows the relationship of dependence on temperature vs. the BST_x dielectric constant for different compositions. The constant dielectric constant is relatively large for the BST_x. As shown in Figure 1.6, the maximum dielectric constant of $Ba_{0.6}Sr_{0.4}TiO_3$ is around 15000. The relatively large dielectric constant makes BST_x ceramics one of the promising materials for bulk capacitor fabrication.[13]

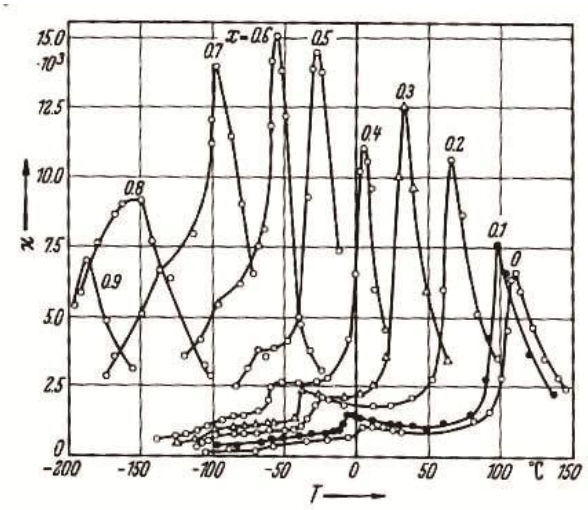

Figure 1.6. *Temperature dependence of dielectric constant of BST_x with different composition.[13]*

1.3 Ferroelectric phase transition

A ferroelectric phase transition is a structural phase transition which results in the ability of the crystal to sustain a spontaneous polarization, caused by the relative displacement of the ions of each unit cell of the crystal.[16] The ferroelectric phase transition occurs at a temperature T_C, analogous to the Curie temperature of a ferromagnet. Above the Curie temperature, the crystal is usually a centrosymmetric paraelectric. Below the Curie temperature the crystal is no longer centrosymmetric, which results in ferroelectric behavior. In the ferroelectric phase, at least one set of ions in the crystal sits in a double well potential, where either of two positions is equally energetically favorable. [15] Above TC, the particles in the double well have enough kinetic energy to move back and forth over the barrier that separates the wells, so that the time average position of the atom is midway between the wells. Figure 1.7 shows the thermodynamic potential of the system as a function of the atom position.

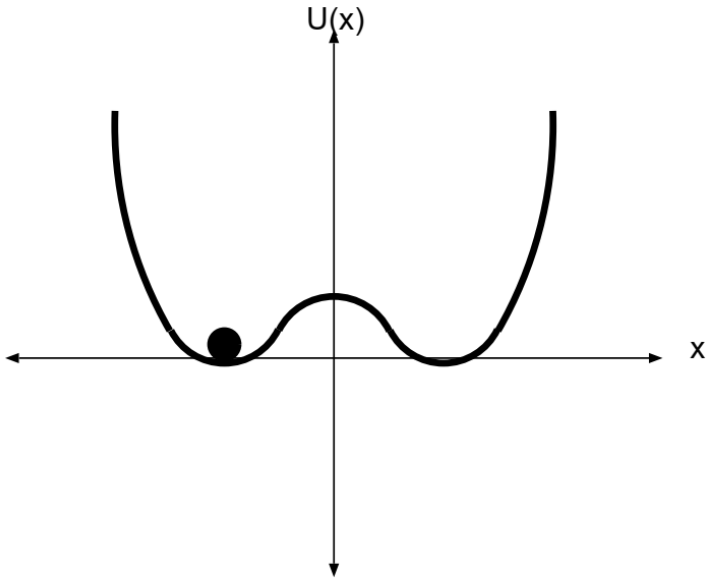

Figure 1.7. *Thermodynamic potential as a function of atom position for a ferroelectric material below its Curie temperature. Conceptual atom sitting in one of two equally energetically favorable positions.[16]*

If the shape of the well stays the same above Tc, but the ion kinetic energy k_BT becomes large, the transition is an order-disorder phase transition. If the minima of the well actually move together to form a single well above Tc, then the transition is displacive. These are the extrema of the phase transition phenomena; most ferroelectric phase transitions are a combination of displacive and order-disorder transitions.[16]

1.4 P-E hysteresis

Ferroelectric (FE) materials, in the absence of an external electric field, change spontaneous polarization within a certain temperature range. Above the Curie temperature, this spontaneous polarization disappears and the ferroelectric phase transitions to a non-ferroelectric phase (paraelectric phase), where the material exhibits linear dielectric behavior.[17] High electric-field breakdown strength, large maximum polarization, small remnant polarization, and slim P–E loops all contribute to obtaining high U_{dis} and η. Although linear dielectric materials usually have higher breakdown strength and lower energy loss, their small maximum polarization (which is proportional to the dielectric constant) prevents them from being used in high-energy storage applications.[18] Importantly polar nanoregions or nanodomains would influence energy storage performance.[19] The energy storage properties of FE materials in the FE state are explained in Figure 1.8 (a), (b) and (c); low remanent bias and large peak bias, high breakdown strength is also the key to obtaining dielectric materials with superior energy storage performance. Obtaining a high breakdown state requires high quality FE ceramics with low porosity, fine and uniform grain size distributed all along the compound.

Relaxor ferroelectrics, particularly crossed ferroelectrics, show thin, high-permittivity P-E hysteresis loops, which is important for high-energy storage applications.

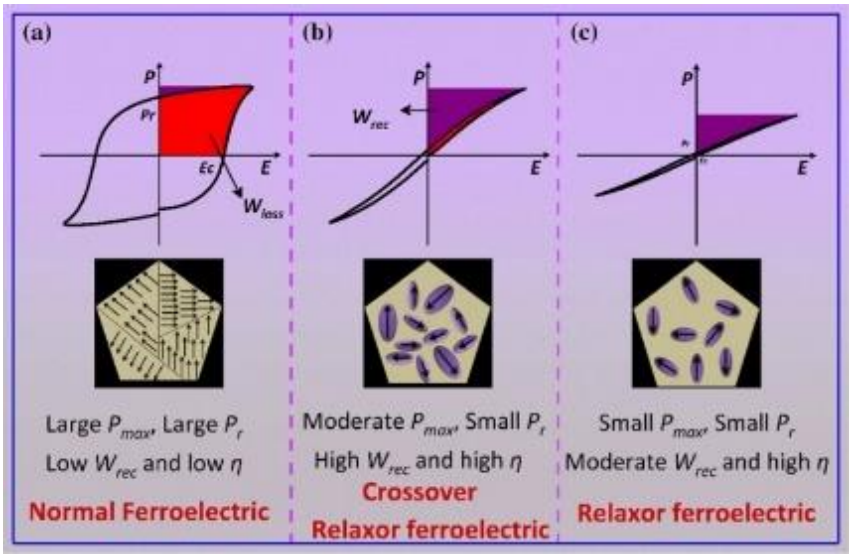

Figure 1.8. *Diagram energy storage hysteresis loops for (a) normal ferroelectric, (b) crossover relaxor, (c) relaxor ferroelectric. Whit different domain morphologies.[20]*

Noting that polar nanoregions or nanodomains would influence the performance of energy storage. In Figure 1.8(a) and (b), the ferroelectrics show much higher P_{max} and P_r. Also, less nonlinear characteristics over the temperature range, and lower W_{rec} and η are obtained. relaxor ferroelectric, as shown in Figure 1.8(c), displays higher η due to more nonlinear characteristics and existence of nanodomains, but with a moderate W_{rec} because of the smaller polarization. The crossed ferroelectrics have in their domain morphologies are also considered nanodomains, which have a little larger polarization when compared to the relaxor ferroelectrics. As shown in Figure 1.8(b), crossover ferroelectric has both high P_{max} and small P_r and produce a higher W_{rec} and η. The above analysis indicates that these are the prerequisites to designing an effective dielectric material for practical use with high efficiency and high recoverable energy-storage density. These three requirements need to be satisfied simultaneously: small remnant polarization, large saturation polarization, and high electric breakdown field.[20]

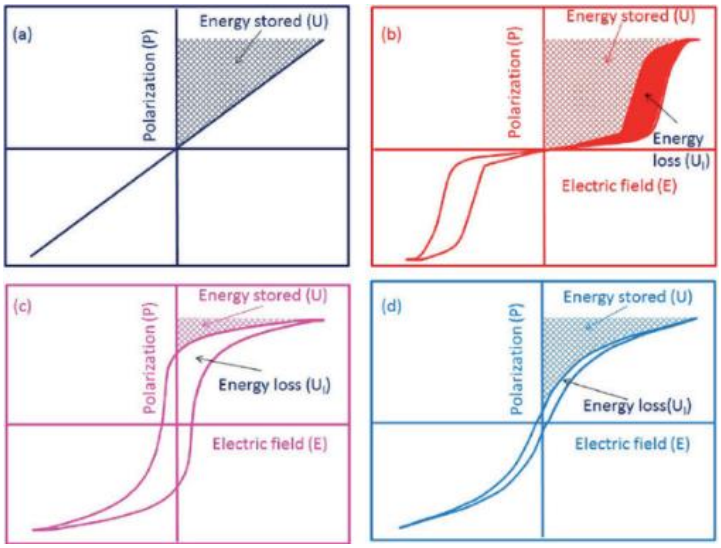

Figure 1.9. *Schematic description the energy storage characteristics of (a) linear dielectric, (b) antiferroelectric, (c) ferroelectric, and (d) relaxor ferroelectric ceramic.[21]*

Figure 1.9 (a)-(d) representative D-E loop graphs for the four types of dielectrics applied to energy storage (a) linear dielectric with constant permittivity (b) antiferroelectric with zero net remnant polarization (c) ferroelectric with spontaneous polarization and (d) relaxor ferroelectric with nanosized domains. Linear dielectrics have lower energy losses and higher breakdown fields, the small bias values resulting from the use of low permittivity dielectrics can reduce their effectiveness for high energy storage purposes. Ferroelectrics generally have moderate electric field strengths and larger saturated biases; however, due to their larger remnant biases, they are often less efficient and have smaller energy storage densities. Figure 1.9 demonstrates that antiferroelectric and relaxing ferroelectrics are more attractive for high energy storage due to their relatively moderate breakdown fields, smaller remnant polarizations, and larger saturated polarizations.[21] It is found that the antiferroelectric (AFE) materials are very promising due to their large P_{max} and low P_r, and their unique polarization versus electric field characteristic, that is, a large recoverable polarization involved during charging and discharging processes.

1.5 Lead-free ceramics

To pursue electrostatic capacitors with high energy density and large energy storage efficiency, lead-free relaxor are often explored as promising materials because of their slim P-E loop feature (i.e., maximum P_{max} and small P_r). The order-disorder cation in relaxor ferroelectric establishes local and heterogeneous polar states in the nanoscale range known as the polar nanoregions (PNRs) and the nucleation and growth of these PNRs are widely accepted as the reason behind the establishment of the slim P-E loop. High-performance ceramic-based capacitors have received much attention as the critical components in pulsed power device, due to ultra-fast charge and discharge speed, wide temperature range of application, long life, and low cost. The energy storage density of capacitor is relatively low.[22]

Dielectric ceramics are usually classified into four types: linear dielectric ($SrTiO_3$, $CaTiO_3$),[23] ferroelectric ($BaTiO_3$,[13] and $BiFeO_3$[24]), relaxor ferroelectric ($Bi_{0.5}Na_{0.5}TiO_3$-based,[25] $BaTiO_3$-based,[26] $K_{0.5}Na_{0.5}NbO_3$-based,[27]) and antiferroelectric (lead-based $NaNbO_3$[28], $AgNbO_3$[29]). Although a large breakdown strength is usually obtained in linear dielectric, the limit of smaller polarization makes it a lower energy storage density. Ferroelectrics show the smaller value of (P_{max}-P_r) and relative lower breakdown electric fields due to the existence of domains, internal defects, stress, electrostriction effect, etc. Antiferroelectric exhibits relatively higher energy storage density and efficiency due to the properties of double P-E hysteresis loops and a negligible P_r in the antiferroelectric state. However, the electric hysteresis effect usually results in a high loss and limits the energy efficiency of antiferroelectric in a deficient value (<80%), such as in PLZT, PLZST, $AgNbO_3$.[30] For these displayed, relaxing properties

ferroelectric (relaxor) are considered as promising candidates for high-performance energy storage applications, such as advanced pulsed power capacitors. Lead-free ferroelectric materials are considered as one of the most promising piezoelectric with reasonable electrostriction field. Figure 1.10 illustrates the reduction in P_r via the incorporation of BT-BLT ceramics into the host lattice of the $SrTiO_3$ perovskite structure, show enhancement of recoverable energy density (1.93 Jcm^{-3}), improved breakdown strength (300 $kVcm^{-1}$) simultaneously with relatively high efficiency (η= 81%). In the (1-x)$SrTiO_3$-x(0.88$BaTiO_3$-0.12$Bi(Li_{0.5}Ta_{0.5})O_3$ [(1-x)ST-x(BT-BLT)] lead-free ceramics the phase and microstructure exhibits a highly stable perovskite structure along with defect-free dense and compact morphology. The broadened dielectric permittivity anomaly and deviation from curie-Weiss law further evidenced relaxor-ferroelectric nature of the (1-x)ST-x(BT-BLT) ceramics. Novel lead-free dielectric materials are strongly desired to implement the outstanding energy-storage properties in terms of temperature, frequency, and fatigue resistance. The outcomes in this study will deliver a standard for emerging other lead-free dielectric ceramics with both tremendously high energy-storage properties and excellent electric field endurance, which are of pragmatic importance for advanced pulsed power capacitor.[31]

$BaTiO_3$ (BTO) is a well-studied ferroelectric compound stabilized in a tetragonal phase at room temperature. However, a large leakage current is inferred in BTO due to its poor densification. To improve the ferroelectric behavior different cationic dopants such as Na, Sr, Ca, and N had been doped in BTO earlier. However, the study of energy storage capacitive behavior of Sr-substitution on the *A*-site of BTO compound is limited. Ba_{1-}

$_xSr_xTiO_3$ (BST_x) is known to be a good ferroelectric material stabilized in the ABO_3-type perovskite phase.

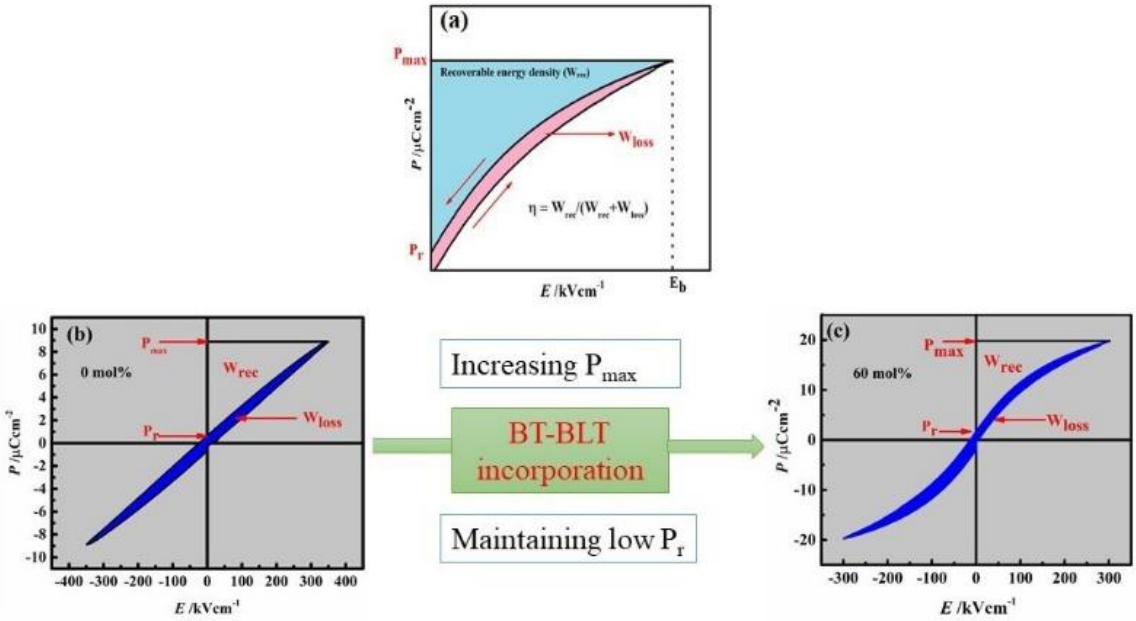

Figure 1.10. *Schematic representation (a) P-E loop relaxor-ferroelectric (recovery). Explain process charging and discharging. (b) Transformation from the paraelectric state to relaxor- ferroelectric state, enhancement of P_{max} and higher W_{rec} with suppressed P_r. [31]*

The *A*-site of the perovskite is occupied by Ba and Sr cations, *B*-site by T_i cation, and that stabilizes in a tetragonally distorted ferroelectric phase. Eventually, ferroelectric BST_x transforms to a paraelectric cubic phase around T_C 96 °C.[32] It exhibited good dielectric behavior with low tangential loss in the microwave frequency range. The study of such high-performing dielectric materials is important for high-frequency device applications. In recent years, advances in dielectric capacitor technology have attracted significant research interest in developing lead-free eco-friendly electronic materials for energy storage applications.

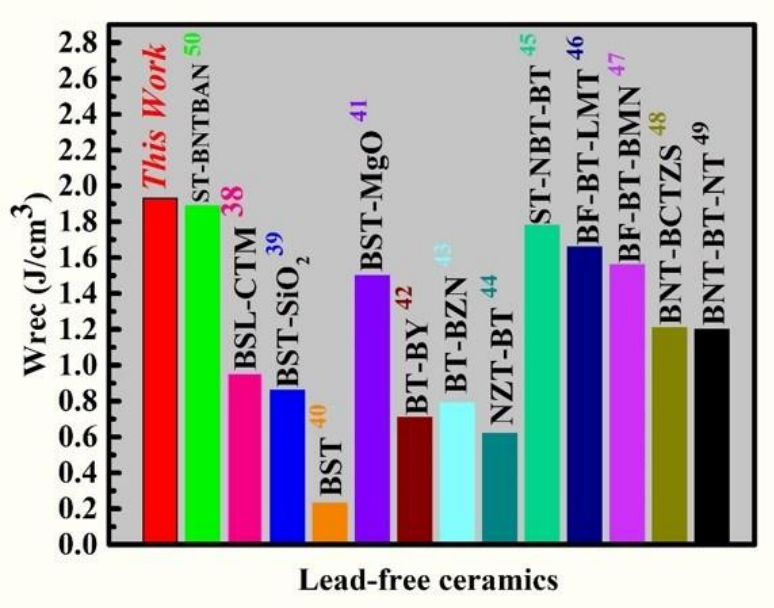

Figure 1.11. *Energy-storage performance of some reported promising eco-friendly ceramics. [31]*

In this thesis, I will be reporting on the fabrication of $Ba_{1-x}Sr_xTiO_3$ (BST_x) for x = 0.1, 0.3, and 0.7, coined as BST1, BST3, and BST7, respectively capacitors using the conventional solid-state method and investigation of their structures, vibrational, ferroelectric polarization, and capacitive storage energy density using X-ray diffraction, Raman spectroscopy, and ferroelectric polarization measurements. The bandgap energy and leakage current behavior of these samples have also been studied for the sake of completeness.

1.6 Synthesis barium strontium titanate (BST_x)

At present, several methods are presented for the synthesis of Barium strontium titanate (BST_x) nano powders with different morphology and properties. Each of these (BST_x) has an individual characterization that makes it suitable for a special application. Every method has a special quality, it makes it take precedence over other methods. Low

processing temperature is a desired point that most methods are intended to achieve. Below are some BST_x properties and summary manufacturing routes.

At present, great attention has been paid to the synthesis and characterization of nanomaterials due to their novel chemical and physical properties related to density and the quantum size effect, compared to the bulk material.[33] Finding that the BST_x received great attention due to its chemical stability, high permittivity, high tunability and low dielectric losses.[34] The physicochemical properties of these nanomaterials are highly sensitive to their size, shape, and composition. These properties strongly depend on the composition and characteristics of raw materials.[35] BST_x has been the most intensively investigated because of its high dielectric constant, low dielectric loss and good thermal stability.[36] The properties of nanostructures differ from that of bulks due to the small sizes and large surface-to volume ratios. However, BST_x powders were commonly prepared by solid-state reaction. Managing to synthesize nanometric powders, a fundamental requirement to obtain the mentioned properties, for their application in devices. This is achieved by mixing the $BaCO_3$, $SrCo_3$ and TiO_2 powders in a high energy ball mill (500 rpm), in isopropanol. Then it goes to the temperature optimization process in the calcination process. Verifying with the XRD, the formation of the perovskite as Barium titanate ($BaTiO_3$) and Strontium titanate ($SrTiO_3$) are crystallized in perovskite structure. Figure 1.12 shows the perovskite structure for $BaTiO_3$. When $SrTiO_3$ is added to $BaTiO_3$, Ba ions can be replaced with Sr ions to form the BST_x in the mentioned structure.

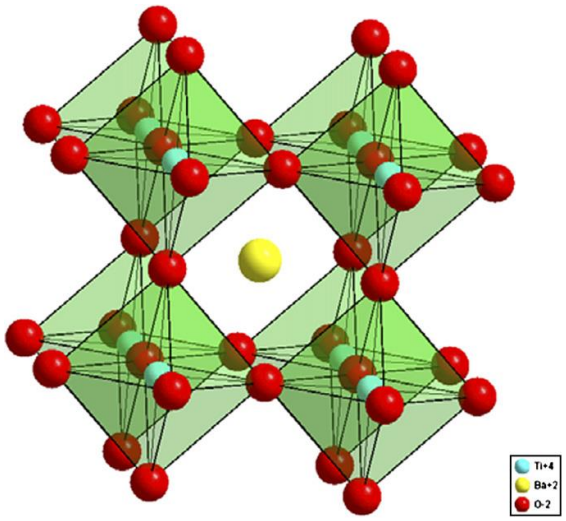

Figure 1.12. *Perovskite structure.*

1.7 (Ba, Sr) TiO_3 Ferroelectric ceramics for capacitor

1.7.1 Principles and measurement method

With the manufacture of capacitors with dielectric materials, electric energy can be stored by applying an electric field. A typical dielectric capacitor consists of two electrode plates sandwiching a dielectric material, as shown in Figure 1.13. The maximum applicable electric field is related to the dielectric breakdown strength of the dielectric. Capacitance, which quantifies the energy storage capacity of dielectric capacitor, is determined by geometry and permittivity. And the energy storage capacity of the capacitors, can be calculated using,

$$C = \varepsilon_0 \varepsilon_r \frac{A}{d} \quad \text{..... (1)}$$

In Equation (1), C is the capacitance, A is the area of the overlapping conductive plates, ε_r is the relative permittivity, ϵ_0 is the vacuum permittivity (~8.85×10^{-12} Fm^{-1}), and d is the distance between the two conductivity plates.

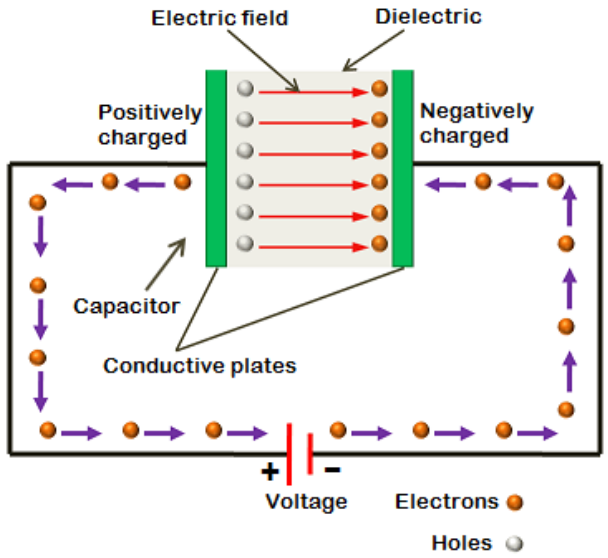

Figure 1.13. *Diagram dielectric polarization during charging process.[37]*

Electrical polarization within a dielectric occurs when an external voltage V is applied, generating accumulated charges in the surfaces of the conductive plates. The process ends when the electric potential induced by accumulating charges ± Q on the surfaces of the plates is equal to the applied voltage V. The capacitance, *C*, can be defined according to the increment change of charge with respect to voltage:

$$C = \frac{\mathrm{dQ}}{\mathrm{dV}} \quad \text{..... (2)}$$

The total energy W storage density during charging is, [38]

$$W = \int_0^Q V dq \quad \text{..... (3)}$$

The surface charge density (Q/A) on the plates is equal to the electrical displacement D = $\varepsilon_0 \varepsilon_r E$ characteristic of dielectric materials. According to Equation (3), the energy storage density U_{st} can be expressed as:

$$U_{st} = \frac{W}{Ad} = \frac{\int_0^{Qmax} vdq}{Ad} = \int_0^{Dmax} EdD \quad \text{..... (4)}$$

where E is the electric field, equal to *v/d*, and D_{max} is the electric displacement under the maximum field (E_{max}). When the dielectric has high permittivity (D is equal to the polarization P) equation (4) can be written as,

$$U_{st} = \int_0^{P_{max}} EdP = \int_0^{E_{max}} \varepsilon_0 \varepsilon_r EdE \ldots\ldots\ldots\ldots\ldots\ldots (5)$$

The energy storage density U_{dis} is calculated by integrating the effective area between the polarization axis and the discharge curve of the polarization-electric field (P-E) loops, shown by the yellow shaded area in Figure 1.14. Schematic of dielectric energy storage. The I to II process illustrates the charging (polarization) of a dielectric layer, in which pristine randomly oriented dipoles are aligned and stretched by the electric field; the II to III process represents the discharging process.[39]

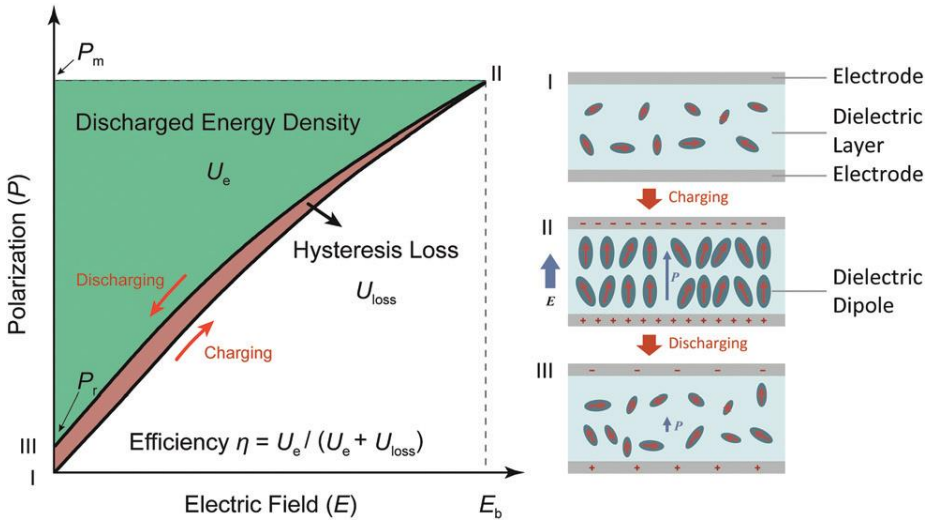

Figure 1.14. *Schematic sketch illustrates the charging and hysteresis loss of storage energy density at an electric field of* E_{max}*. [39]*

In other words, the amount of recovery energy storage density dissipated during the discharge process is defined as U_{dis}, illustrated by the yellow shaded area in the Figure 1.14, [40]

$$U_{dis} = \int_{P_r}^{P_{max}} EdP \ldots\ldots\ldots\ldots\ldots\ldots\ldots\ldots\ldots\ldots\ldots\ldots\ldots \text{(6)}$$

and the energy storage efficiency (η) can be written:

$$(\eta) = \frac{U_{dis}}{U_{st}} \ldots\ldots\ldots\ldots\ldots\ldots\ldots\ldots\ldots\ldots\ldots\ldots\ldots\ldots\ldots \text{(7)}$$

For device application of ferroelectric capacitors, both a high storage energy density and a high storage energy efficiency (η) are crucial. During the electric field action period, the electric field varies from zero to maximum E_{max} resulting in increment of the ferroelectric polarization to the maximum P_{max}, and that stored electric energy in ferroelectric capacitor known as the charge energy storage density U_{st}. Upon decrease of the electric field from maximum E_{max} to zero, the recoverable energy storage density is released from the capacitor called the discharge energy density U_{dis}. However, the energy density stored between the charge and discharge process is unrecovered due to the hysteresis loss, called loss energy density U_{loss}.

The energy storage behavior of ferroelectric capacitors is studied from the electric field dependence of energy-storage density estimated from P-E hysteresis loops using the Equation (5), (6) and (7). Where P_{max}, P_r and E denote the maximum field-induced polarization, remnant polarization, and applied electric field, respectively. It is critical to have higher dielectric breakdown strength (BDS) and large polarization difference (P_{max}-P_r) to achieve high energy performance ceramic based on Equation (5), (6) and (7). Therefore, the stored energy is $U_{st} = U_{dis} + U_{loss}$, which can be calculated for applied field increases from 0 to E_{max}. For clarity, a schematic sketch illustration of the charging, discharging and loss storage energy density of a ferroelectric capacitor at a maximum electric field of E_{max} is shown in Figure 1.14.

1.7.2 Energy-storage performance BST_x

The fundamental characteristics of ferroelectric-relaxor materials in high electric fields, and how this impacts energy storage operations. Table 1.1 shows typical BST_x electricity parameters for energy storage. From the point of view of a real application, it is reasonable that not only the energy density, but also the energy efficiency of a material should remain equal for use in high-energy capacitors.

Table 1.1. *The parameters of important dielectric materials for energy storage.*

Materials	Modification or state	Breakdown Strength [$kVcm^{-1}$]	Dielectric constant	Dielectric loss	Energy density [Jcm^{-3}]	Energy efficiency	Ref.
$BaTiO_3$-$SrTiO_3$	Layer structure	157	-	1-2%	1.16	-	[41]
$(Ba_{0.4}Sr_{0.6})TiO_3$	Bulk state	197	990	0.01	1.3	-	[42]
$Ba_{0.4}Sr_{0.6}TiO_3$	Bulk state	91.9	992	-	0.37	-	[43]

In recent investigations it has been reported that the energy density of the ferroelectric materials used in ceramic capacitors can be experimentally optimized, using their: electrical properties, spontaneous polarization, Curie temperature and the rupture force.[44] The substitution of modification is one such approach to tailor the electrical properties of ferroelectric materials. Thus Ca^{2+}(or Sr^{2+}) and Zr^{4+} to replace Ba^{2+} and Ti^{4+}, have been introduced into barium titanate at the Ba site or Ti site to adjust the electrical breakdown and polarization behavior.[45] Among these modified materials, barium strontium titanate (BST_x) is considered one of the most promising candidates for ceramic devices for its excellent characteristics of high dielectric permittivity, low leakage current, and tunable permittivity or bias by switching compositions between BT and ST. It has also been reported that $(Ba_{0.4}Sr_{0.6})TiO_3$ ceramics synthesized by solid state reaction, adjustable grain sizes (0.3–3.4 μm) have been obtained. The dielectric breakdown strength is obviously adjustable from 108 kV cm^{-1} to 197 kV cm^{-1} and then decreased to 154 kV cm^{-1}

with decreasing grain size show Figure 1.15, representing the change in energy density from 0.49 J cm^{-3} to 1.3 J cm^{-3}.[42] It can be concluded that the dielectric breakdown depends not only in the interfacial polarization that originates from the significant increase in oxygen vacancies, but also in the grain boundary density, which is related to the grain size.

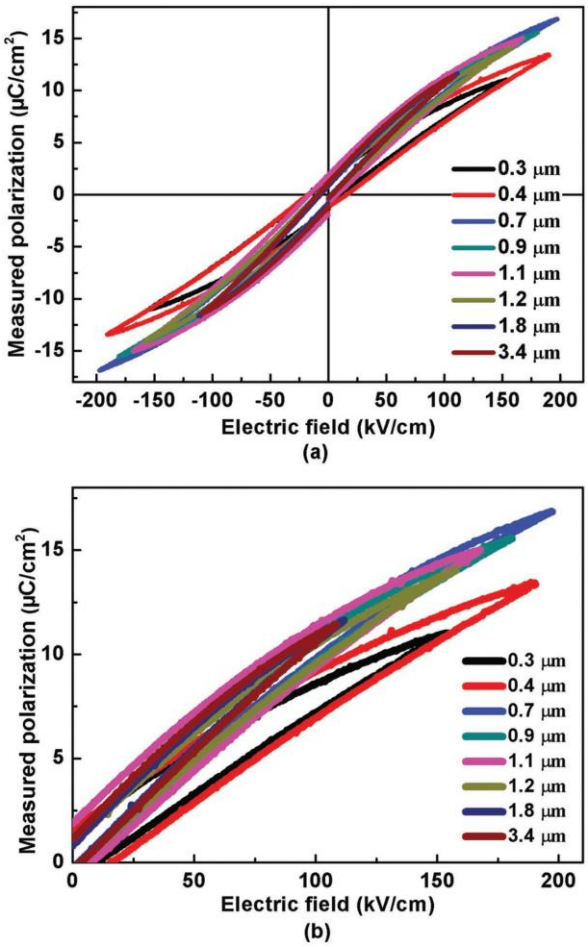

Figure 1.15. a) *The hysteresis loops of $Ba_{0.4}Sr_{0.6}TiO_3$ ceramics with various grain sizes.* ***b)*** *The corresponding Emax values in the first quadrant.[46]*

For energy storage applications, good electric field endurance is one of the crucial factors to consider. The critical breakdown strength is the very electric field before the BST ceramics had electric breakdown during P-E loop measurement. The critical breakdown

strength of the BST ceramics sintered in N_2 (11.97 kV/mm), air (13.97 kV/mm) and O_2 (16.72 kV/mm) is increased with the increasing oxygen partial pressure, as shown in Figure 1.16. The high electric breakdown of BST ceramics sintered in O_2 is directly attributed to its fine grain size: under the action of a strong electric field, electrostriction would occur with the orientation of polar nano-regions, and the stress caused by the electrostriction is proportional to the size of grains, that is to say, the lager the grain is, the stronger the stress would be, which would cause the dielectric breakdown of the ceramics.[47]

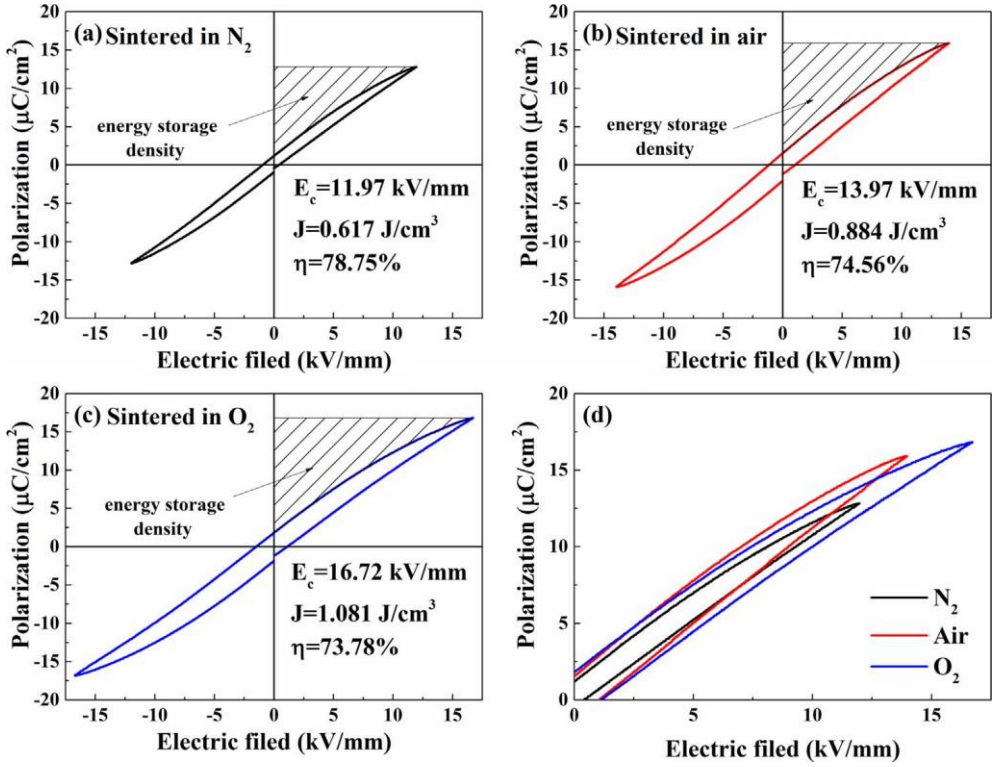

Figure 1.16. *P-E loops at their critical breakdown strength Eb for the $Ba_{0.4}Sr_{0.6}TiO_3$ ceramics sintered in (a) N_2, (b) air and (c) O_2 atmosphere respectively. (d) Unipolar P-E loops of the three samples. The calculated energy storage density J and the energy storage efficiency η are listed in the insets.[47]*

1.8 Lithium sulfur (Li-S) batteries

Recent investigations into the chemistry of Li-S batteries show them as promising systems for the next generation of batteries. With theoretical sulfur capacity that is almost an order of magnitude higher than current lithium-ion battery insertion cathodes and, when combined with a lithium metal anode, Li-S batteries promise energies specific almost five times higher. However, this statement is only valid if sulfur cathodes could be designed in the same way as cathodes for lithium-ion batteries. In this thesis work, recent efforts to design high-capacity sulfur-based thick cathodes are explored. Various papers are compared in terms of capacity, areal mass charge, and conductive additive fraction, which are the critical parameters that dictate a device's potential to achieve a specific target energy superior to current lithium-ion batteries that is greater. at 200 Wh Kg^{-1}. Compared to most cases that project a lower specific energy, currently several promising strategies have been designed to achieve a potential greater than 500 Wh Kg^{-1}. Challenges associated with the limited life cycle of these systems are also discussed due to both the polysulfide shuttle phenomenon and the rapid degradation of the Li metal anode experienced at the current densities required to charge high specific energy batteries in a reasonable period.[48]

1.8.1. Principle of Li-S battery

Research on Li-S batteries dates to the 1960s, when elemental sulfur and metallic lithium were used directly as the cathode and anode, respectively [49,50]. The overall reaction inside a Li–S battery follows the simple combination of Li and S to form Li_2S.

$$16Li+S_8 \leftrightarrow 8Li_2S \quad \text{(1.8)}$$

The complete reaction of Li and S; generates high capacitance of the anode and cathode can be as high as capacity 3860 and 1670 $mAhg^{-1}$ (gravimetrically) or 2200 WhL^{-1}

(volumetrically) at an operating 2.15 V vs. Li/Li^+. Much higher values compared to the theoretical value for commercial LIBs; 387 Wh kg^{-1} or 1015 Wh L^{-1}, based on $LiCoO_2$ cathode and graphite anode materials operated at 3.8 V. [51]

1.8.1.1. Electrochemistry of Li-S battery

Li–S standard batteries are composed of a composite positive electrode (cathode) of elemental sulfur with a conductive additive and a polymer binder, a negative electrode (anode) of lithium metal as well as a porous separator impregnated with liquid organic electrolyte, as show schematic in Figure 1.17.(a). [51] Now we will analyze battery assembled with lithium metal anode and a composite sulfur cathode is already in the "charged" state as soon as it is assembled and packed. In some other cases, where a cathode with Li_2S based composite is used, the battery must be first charged to form lithium and sulfur at the relative electrodes. If a "catholyte" of lithium polysulfide (usually Li_2S_6 or Li_2S_8) is selected, then the battery can be in an intermediate state between charge and discharge. Despite the different initial electrode materials, the difference in the electrochemistry of these systems lies only in the first charge or discharge process, and in later cycles, they all undergo the battery reaction as shown in Equation 1.8. The reactions that occur in Li-S batteries, in the electrochemical process, are really very complex. Because polysulfide has several intermediate steps like soluble and insoluble as shown Figure 1.17.(b). In general, for the analysis of the discharge process of a Li-S battery, it is generated with the reduction of elemental sulfur to lithium sulfide (Li_2S) can be divided into three stages with two different voltage output plateaus in 2.4 V and 2.1 V versus Li/Li^+ in the discharge profile, which agrees with the solubility of the intermediates.

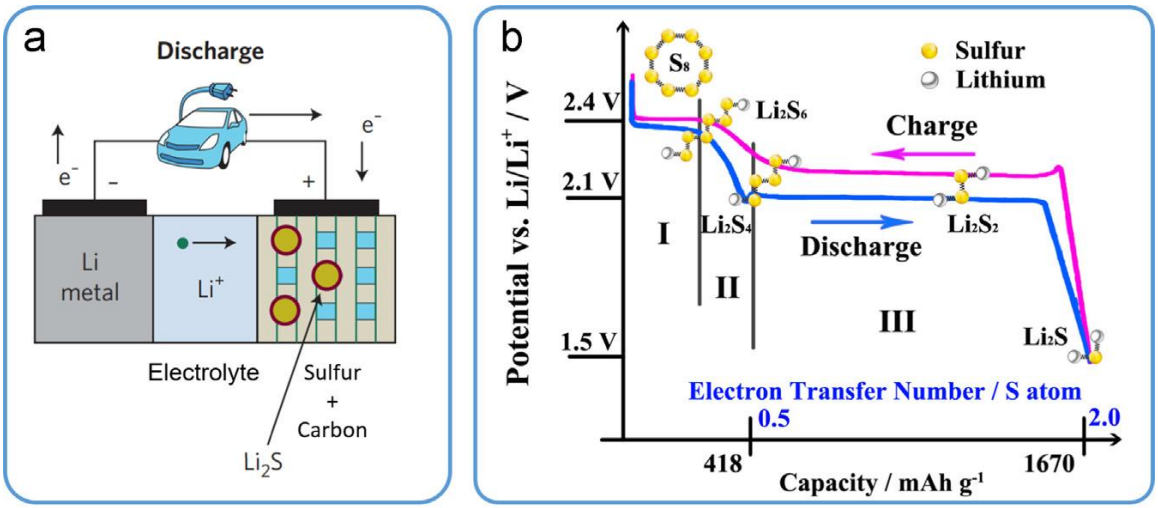

Figure 1.17. *(a)Schematic of Li-S batteries.[51] (b) Charge-Discharge voltage profiles of the cathode.[52]*

In the first stage as show section, I in Figure 1.17. (b) at 2.4 V, elemental sulfur (S_8) is stepwise reduced at 2.4^{-2} by $2e^-$ in each step as shown in Equation (1.9) and (1.10), forming soluble long chain polysulfides.

$$S_8+2e^-\rightarrow S_8^{2-} \quad \text{(1.9)}$$

$$3S_8^{2-}+2e^-\rightarrow 4S_6^{2-} \quad \text{(1.10)}$$

Following that, the sharp drop in voltage from 2.4 V to 2.1 V could be responsible for the formation of S_4^{2-} as illustrated in Equation (1.11), as show in Section II in Figure 1.17.(b).

$$2S_6^{2-}+2e^-\rightarrow 3S_4^{2-} \quad \text{(1.11)}$$

For the next stage at 2.1 V, long chain lithium polysulfides are further reduced into insoluble lithium sulfides by the two $2e^-$ processes shown in Equations (1.12) and (1.13), as show section III in Figure 1.17.(b).

$$S_4^{2-} + 2e^- + 4Li^+ \rightarrow 2Li_2S_2 \quad \text{(1.12)}$$

$$Li_2S_2 + 2e^- + 2Li^+ \rightarrow 2Li_2S \quad \text{(1.13)}$$

It is important to note that the reactions of equations (1.12) and (1.13), the reaction kinetics are very slow due to the slow reaction in solid state that forms Li_2S_2 and Li_2S. Consequently, in most cases a mixture of Li_2S_2 and Li_2S is finally obtained, resulting in a real cathodic capacity lower than its theoretical value of 1670 $mAhg^{-1}$. During the charge process, the reaction sulfide oxidation reaction is reversed in the charge–discharge profile (Figure 1.17(b)) through two voltage plateaus at ca. 2.2 V and 2.5 V vs. Li/Li^+ forming insoluble Li_2S_2 and soluble Li_2S_x ($4<x\leq8$), respectively. Hereinafter, we define that 1 C as 1670 mA g^{-1}_{sulfur}, at which rate elemental sulfur is fully discharged/lithiated into Li_2S at 1 h in a Li–S battery.[52]

Elemental sulfur became reduced to long-chain polysulfide ions (mainly S_7^{-2}, S_6^{-2}, and S_5^{-2}), and S_8^{-2} was formed through the subsequent reaction between the long-chain polysulfide ions and sulfur.[53] During this period, a chemical equilibrium was maintained among S_7^{-2}, S_6^{-2}, and S_5^{-2} until substantial amounts of S_7^{-2} and S_6^{-2} were consumed around 2.3 V, and then the potential started to decrease. Based on the above discussion, shows the mechanism of the three-stage sulfur reduction reaction. Proposed discharge Mechanism of sulfur in a Li-S Battery. [54]

>2.3 V, first plateau, major species are bold.

$$S_8 \underset{\rightarrow}{^{-ne}} (S_8^{2-} + \boldsymbol{S_7^{2-}} + \boldsymbol{S_6^{2-}} + S_5^{2-} + S_4^{2-} + S_3^{2-})$$

$$\boldsymbol{S_7^{2-}} \leftrightarrow \boldsymbol{S_6^{2-}} \leftrightarrow \boldsymbol{S_5^{2-}}$$

Between 2.3 and 2.1 V, major species are bold.

$$S_8^{2-} + S_7^{2-} + S_6^{2-} + \boldsymbol{S_5^{2-}} \underset{\rightarrow}{^{-ne}} \boldsymbol{S_4^{2-}} + S_3^{2-} + Li_2S_2 \downarrow + Li_2S \downarrow$$

<2.1 plateau, major species are bold.

$$\boldsymbol{S_5^{2-}} + \boldsymbol{S_4^{2-}} + S_3^{2-} \xrightarrow{-ne} Li_2S_2 \downarrow + Li_2S \downarrow$$

$$\boldsymbol{S_5^{2-}} \leftrightarrow \boldsymbol{S_4^{2-}} \leftrightarrow \boldsymbol{S_3^{2-}}$$

Therefore, unlike the stepwise reduction process, the oxidation of polysulfide ions was conducted through the electrochemical formation of polysulfide ions $S_n^{2-}(5 \leq x \leq 7)$ and sulfur, while chemical equilibrium among S_5^{2-}, S_6^{2-}, S_7^{2-}, and S_8^{2-} remained throughout the whole oxidation process. The oxidation reaction mechanism proposed charged mechanism on the cathode in Li-S Battery. [54]

Cathode potential < 2.4 V

$$Li_2S_2 \downarrow + Li_2S \downarrow \xrightarrow{-ne} S_8^{2-} + S_7^{2-} + S_6^{2-} + S_5^{2-}$$

$$S_8^{2-} \leftrightarrow S_7^{2-} \leftrightarrow S_6^{2-} \leftrightarrow S_5^{2-}$$

Cathode potential > 2.4 V

$$S_8^{2-} + S_7^{2-} + S_6^{2-} + S_5^{2-} + S_4^{2-} + S_3^{2-} \xrightarrow{-ne} S_8$$

$$S_8^{2-} \leftrightarrow S_7^{2-} \leftrightarrow S_6^{2-} \leftrightarrow S_5^{2-}$$

It was revealed by the real-time quantitative determination of polysulfide species and elemental sulfur by means of high-performance liquid chromatography during the discharge and recharge of a Li-S battery. A three-step reduction mechanism including two chemical equilibrium reactions was proposed for the sulfur cathode discharge, as show Figure 1.18. The typical two-plateau discharge curve for the sulfur cathode can be explained. A two-step oxidation mechanism for Li_2S and Li_2S_2 with a single chemical equilibrium among soluble polysulfide ions was proposed. The chemical equilibrium among S_5^{2-}, S_6^{2-}, $S_7^{2-}$and S_8^{2-} throughout the entire oxidation process resulted for a single flat recharge curve in Li-S batteries, as show Figure 1.18. [54]

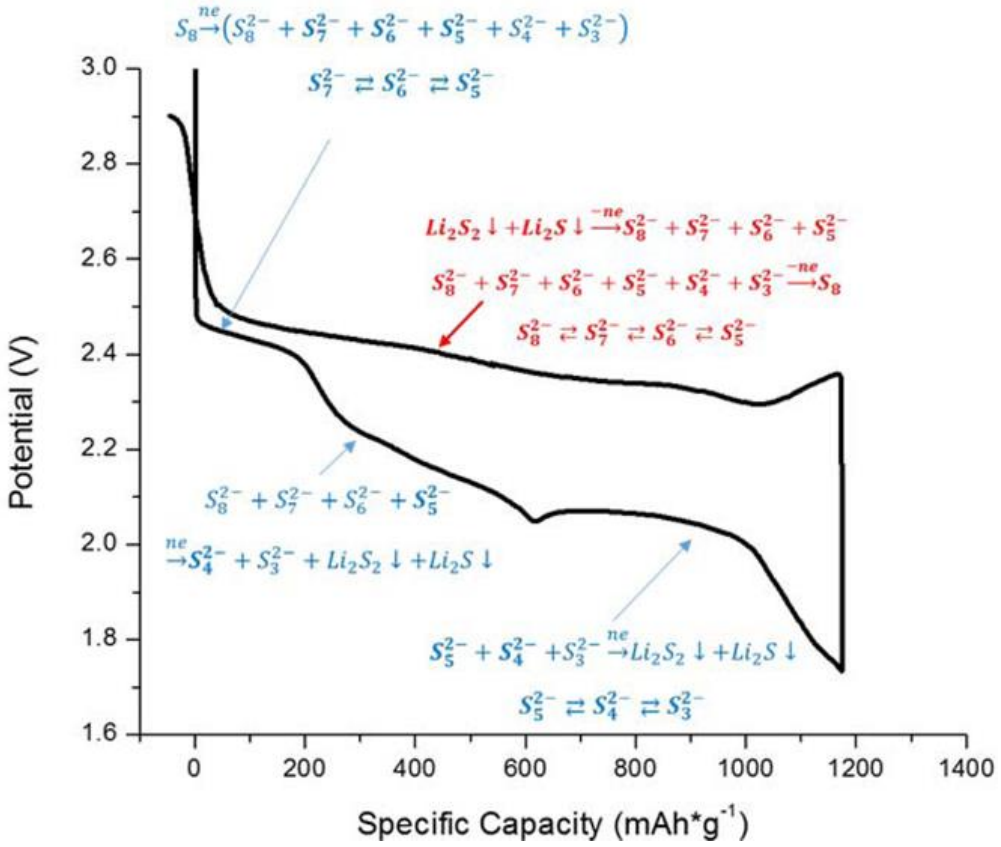

Figure 1.18. *Mechanism of the sulfur cathode in Li-S batteries.[54]*

1.9 Advantages of Li-S batteries

Lithium-sulfur batteries have the great advantage in energy storage devices, due to their high theoretical specific capacity (2500 Wh kg $^{-1}$, 2800 Wh L^{-1}, assuming a complete reaction to Li_2S) has been the motivation of a great number of works.[55] But these batteries have drawbacks that have restricted their applications: high electrical resistance, vanishing capacity, self-discharge, mainly due to the so-called shuttle effect.[56] All reviews of Li-S batteries over the years have repeatedly reported these difficulties with which the electrochemical research community struggles. In addition, the problem of high resistance of the sulfur and the polysulfides has been solved by adding conductive elements, like carbon under different forms in the cathode, at the expense of the amount of

active material available for the electrochemical process.[57] Currently these problems have not been completely solved, but there has been progress in the last few years, giving hope today that these challenges will be met soon. The purpose of this thesis work is to investigate the structural aspects, electrochemical properties, synthesis aspects. To obtain values of specific capacity close to the theoretical.

The electrochemical reaction during discharge occurs in three steps, as shown in the Figure 1.19:

1. Reversible conversion of sulfur through stepwise reduction up to the formation $S^0 \rightarrow S_4^{2-}$. These polysulfides are soluble, so the reaction kinetics is fast.

2. Conversion of S_4^{2-}, polysulfides to solid Li_2S_2. This $S^{0.5-} \rightarrow S^-$ reduction is more difficult, because of the energy needed to nucleate the solid phase.

3. Conversion from solid Li_2S_2 to solid Li_2S. This is the most difficult step because of the sluggish diffusion of lithium in this solid environment. [58,59]

This decomposition in three steps is an approximation. Electrochemical impedance spectroscopy and in situ X-ray diffraction spectra revealed that Li_2S appear immediately at the beginning of the lower plateau. [60] The charge process is such that all the polysulfides transform via charge transfer following the most facile oxidation state S_8^{2-}. Upon cycling, the S_n^{2-} formed on oxidation of Li_2S_2 and Li_2S (or on reduction of S_8) react with them to form S_{n-x}^{2-} polysulfides at the anode side. They diffuse on the cathode side and are re-oxidized into S_n^{2-} species. This parasitic cyclic process decreases the active mass available in the discharge process and is responsible for a significant decrease in coulombic efficiency in the charge process.[61] A model of this internal shuttle effect has reproduced

quantitatively the self-discharge, coulombic efficiency, thermal effects observed experimentally, giving evidence that this internal shuttle effect is responsible for these problems.

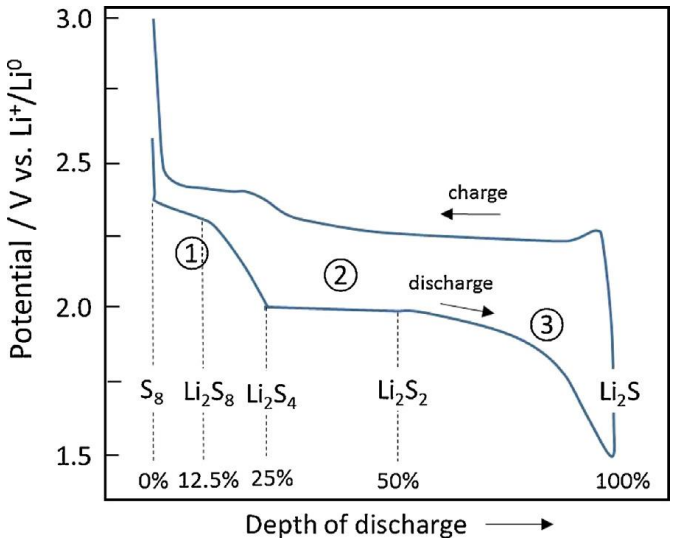

Figure 1.19. *Discharge-Charge profile of Li-S cell, illustrating (I) conversion of solid sulfur to soluble polysulfides; (II) conversion of polysulfide to solid Li_2S_2; (III) conversion of solid Li_2S_2 to solid Li_2S. [59]*

1.9.1 Current challenges of Li-S batteries

Li-S batteries will have a huge impact on applications who would benefit from significant weight reduction, there are several challenges that must be addressed and that impact on the overall cell design, life cycle, safety, and reliability compared to lithium-ion cells. Sulfur and the Li_2S discharge product are electrically insulating.[62] Sulfur is also not a Li ion conductor. For an electrochemical reaction to occur there must be a concurrent transfer of both electrons and ions. Such a situation cannot be achieved at practical rates for thick sulfur films. For this reason, sulfur electrodes are typically mixed with a high surface area conducting material to minimize the effective sulfur thickness between the conductor and the electrolyte to facilitate electronic and ionic transport.[63] Many

strategies have been developed to disperse sulfur in a variety of conducting materials including high surface area carbonaceous materials, polymers, metals, metal oxides, and metal organic frameworks. The proposed strategies are to maximize the amount of sulfur that can be accessed electrochemically at reasonable current densities while minimizing the mass and volume of the conductive phase required (as it adds to the mass of inactive material in the battery) which can constitute a major fraction of the mass and volume of the cathode.

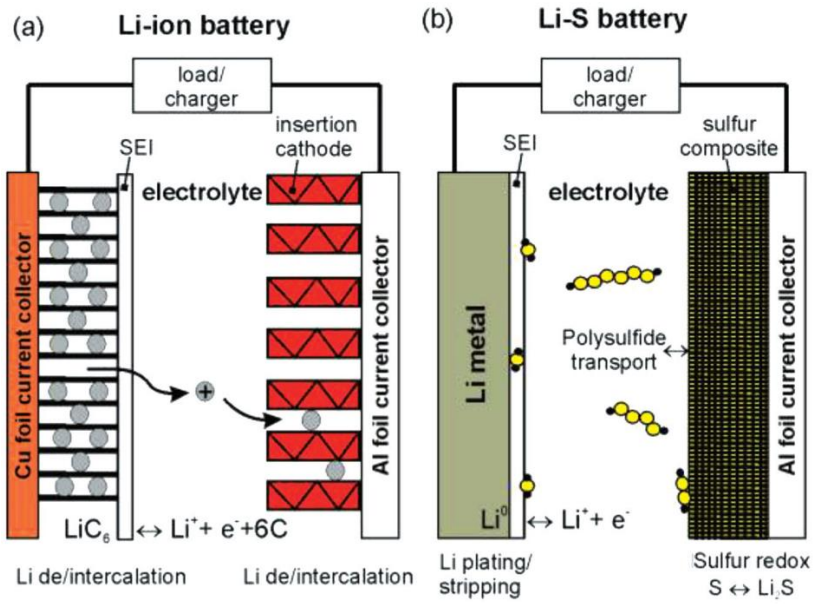

Figure 1.20. *Li-S batteries compared to Li-ion batteries. (a) Typical Li-ion battery comprised of a lithiated graphite (LiC_6) anode and insertion cathode such as $LiCoO_2$ or $LiFePO_4$. On discharge, LiC6 is oxidized, sending an electron through the circuit while Li ions de-intercalate and are inserted into the cathode which is reduced in the process. The reverse occurs when the battery is charged (b) Li-S Battery comprised of a Li metal anode and sulfur composite cathode. [64,65]*

Figure 1.20 shows how lithium-ion batteries work. Reversible intercalation and deintercalation reactions in both the anode and the cathode depend solely on the transport lithium ions between these insertion compounds, typically a graphite anode [64] and a

transition metal oxide cathode. [65] On the other hand, a Li-S battery involves a conversion reaction where various intermediate species referred to as polysulfides are produced. The Li_2Sn ($3 \leq n \leq 6$), generated during the conversion reaction are soluble in most used organic electrolytes.[66] The solubility allows the transport of sulfur species to the Li metal anode where they can react to form the insoluble Li_2S, reducing the Coulombic efficiency and the reversibility of the cell. This solubility provides a mechanism for the redistribution of sulfur in the conductive support material during cyclization, the sulfur was not dispersed homogeneously. [67]

Research also reports that sulfur-based cathodes are not compatible with traditional carbonate-based electrolytes, due to the rapid reaction of the intermediate polysulfides irreversibly with the carbonate solvent, thus exhibiting a high initial capacity that drops to almost zero in the second cycle. [68] This chemical instability has led to the use of alternative, inert, ether-based electrolytes typically composed of a mixture of dioxolane (DOX) and dimethyl ether (DME).[69] Unfortunately, this solvent system poses several challenges associated with its high vapor pressure, such as its pour point. reduced inflammation, which creates safety concerns and practical challenges related to the boiling of solvents during the vacuum process.

The polysulfide problem, the Li metal anode needed to achieve high specific energy is unstable with cycling. Unlike insertion anodes such as graphite which change in volume by ≈20% during cycling, lithium is completely removed from the metal during discharge and replenished upon charge leading to effectively infinite volume change.[70] The reaction products formed between Li metal and the electrolyte form the solid electrolyte interface, a passivation layer which inhibits further reaction between Li metal and the

electrolyte.[70] This also causes the inhomogeneous deposition of Li metal during charge leading to dendritic growth and the development of porous Li metal structures.

1.10 (Ba, Sr) TiO_3 as a cathode additive material

Due to the recent advancement in the production of renewable energy, there is a great demand for advanced energy storage systems. The challenges of lithium-ion rechargeable batteries, to revolutionize the future electrification of transport and the smart grid, is to further increase their energy density. For example, among all rechargeable batteries, lithium–sulfur batteries (Li-S), with an energy density unmatched (2600 Wh kg^{-1}, five times higher than commercially available lithium-ion batteries), as well as low-cost, they show tremendous potential for high-energy storage applications.[71] But in real applications they exhibit rapid capacitance fading, derived mainly from the polysulfide shuttle.[72] The dissolution of heteropolar polysulfides often results in losses active materials on the cathode and cause bad Coulombic efficiency and cyclical stability in Li–S batteries.[73] In current investigations various methods are being explored to address the polysulfide shuttle effect, making progress in recent decades in exciting progress in Li-S batteries has always been accompanied by the emergence of new material concepts to achieve the capture of polysulfides from high efficiency. For example, the confinement form of polysulfides within porous and conductive carbon materials.[74] In this line, different carbon materials, such as graphene,[75] carbon nanotubes,[76] mesoporous carbon,[74] carbon,[77] and their hybrids,[78] have been extensively investigated for polysulfide capture. These investigations have achieved satisfactory results to trap polysulfides. For example: superparamagnetic iron oxide nanoparticles could be used to control the polysulfide shuttle by means of a magnetic field,[79] the concept of

electrocatalysis to the Li-S battery to stabilize the polysulfide transport process through a highly electrocatalytic active graphene/Pt host.[80] These strategies have provided a novel perspective to achieve high-efficiency polysulfide capture and also greatly encouraged us to seek a new direction to conquer the notorious plugging effect of Li-S batteries. It has recently been reported that "spontaneous polarization" ferroelectricity, caused by the asymmetric crystalline structure, offers new opportunities for its photovoltaic and photocatalysis applications,[81] this spontaneous polarization is an aid to build an internal electrical circuit and induces macroscopic charges in the surface of the ferroelectrics. Consequently, many polar molecules from the outside environment will be chemisorbed on the surface to filter out these surface charges.[82] In consideration of the fact that polysulfides are also heteropolar, we speculate that spontaneously polarizing ferroelectric materials can resolve the shuttle effect entirely dependent on a novel ferroelectric enhanced polysulfide capture strategy.

1.10.1 Advance in electrode materials for rechargeable batteries

In research to develop efficient and high-density storage systems, the application of ferroelectric nanomaterials in high-energy storage systems has been directed. Batteries are the most important and most widely used storage system among the different energy storage systems. To improve the performance of rechargeable batteries by studying the main component of batteries, which includes separators, electrolytes, and electrical appliances. The advances and role of ferroelectric electrode materials to improve battery performance and the application of nanomaterials to achieve better capacity and long-life cycle of rechargeable batteries.

For example, BTO is one of the important and widely used ferroelectric materials, [26] in recent investigations it has been introduced into the cathode for the first time as a proof of concept to demonstrate the entrapment of new polysulfide strategies to stabilize the Li-S batteries. After a process of grinding the BTO nanoparticles with the cathode materials, the heteropolar polysulfides manage to anchor in the cathode due to the internal structure of the electric field originated by the spontaneous polarization of the BTO nanoparticles. The hollow carbon nanospheres/S (C/S) cathode with the addition of BTO nanoparticles (C/S+BTO) delivers a discharge capacity of 835 mAh g^{-1} after 100 cycles, two times more than that of its C/S counterpart without BTO (407 mAh g^{-1} after 100 cycles). Meanwhile, with the incremental increase in the current rates of 0.2, 0.5, 1, 2, and 5 C, the discharge capacities of the C/S + BTO cathode were 978, 793, 701, 622, and 438 mAh g^{-1}, respectively, much higher than the C/S composite cathode at the same current densities (726,545, 457, 382, and 286 mAh g^{-1}, at the current densities, respectively), as shown in the Figure 1.21 (c), (d). [83]

Including ferroelectric nanoparticles offers a novel strategy to conquer the polysulfide shuttle to improve Li-S batteries. Furthermore, due to the favorable drivability of this approach, it will also significantly promote the practical use of high-performance Li-S batteries. Using the spontaneously polarized BTO nanoparticles, which function as a functional additive, they were directly mixed with the S-containing C/S composite cathode materials, for different concentrations. The importance of this simple manufacturing method can be perfectly combined with current industrial battery manufacturing processes. Notice that two key issues must be considered to ensure that the BTO nanoparticles can function as stable cathode additives: (1) BTO nanoparticles will not react with Li in the

potential window of 1.5–3.0 V, which is the range of operating voltage of the S cathode, and (2) BTO nanoparticles will keep their ferroelectricity stable during cycling.

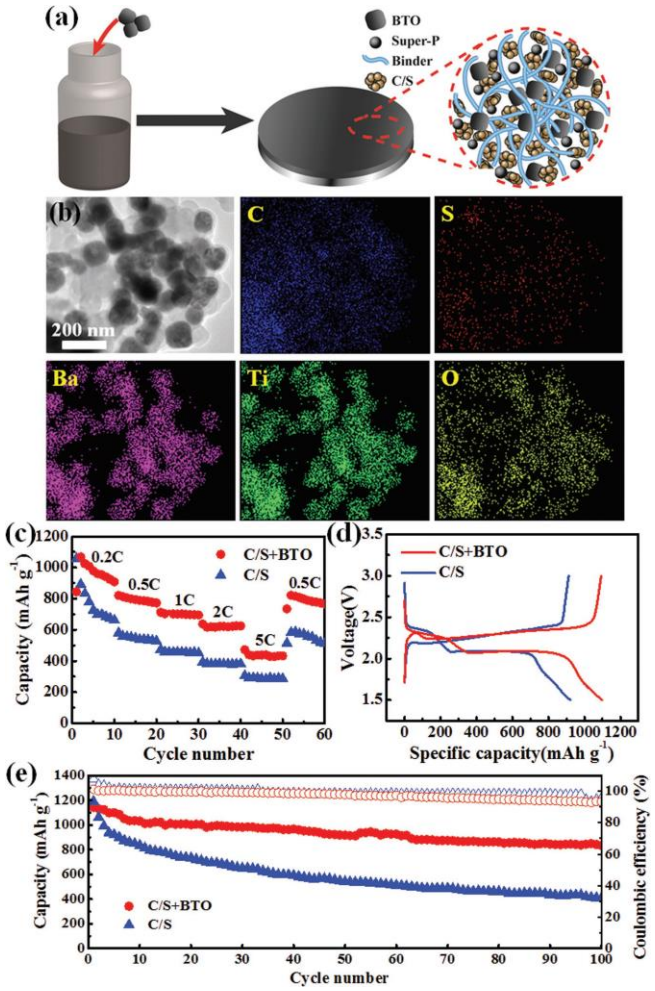

Figure 1.21 *(a)Schematic of the preparation of the BTO-contained C/S cathode. b) TEM image of the prepared cathode and the corresponding elemental mappings. c) Rate performances of the C/S and C/S+BTO composite cathodes at the current density. d) Typical discharge–charge voltage–capacity profiles of the C/S and C/S + BTO composite cathodes. e) Cycling performances of the C/S and C/S+BTO composite cathodes at the current density of 0.2 C. [83]*

All these results showed that the BTO nanoparticles are stable cathode additives while keeping their ferroelectricity. Contrastingly, in the charging process, a long plateau is associated with the conversion of Li_2S into a high-order soluble polysulfide. Moreover, the C/S + BTO composite cathode exhibits a much higher initial discharge capacity of 1143 mAh g^{-1} at 0.2 C. And after 100 cycles, a reversible discharge capacity of 835 mAh g^{-1} can still be retained with a stable CE (Figure 1.21(e)), indicating their long-term cycling stability. As for the C/S composite cathode without BTO nanoparticles, only a reversible discharge capacity of 407 mAh g^{-1} can be obtained after 100 cycles, indicating that the introduction of spontaneous polarized BTO nanoparticles in the cathode can significantly improve the cycle stability of the C/S composite cathode, as expected (Figure 1.21(e)).

In the present research work, it is sought to use BST_x nanoparticles, the simple procedure explained simply by adding the BST_x ferroelectric materials in the cathode C/S, to achieve a better efficiency of the polysulfides can be anchored in the cathode, due to the better stability when including atoms of Sr, enhancing the internal electric field and thus improve the cycle stability as well as the capacity rate of Li-S Batteries efficiently.

1.11 References

[1] J. F. Nye, Physical Properties of Crystals, *Oxford University Press*, Oxford, UK, 1957.

[2] P. S. Halasyamani, K. R. Poeppelmeir, *Chem. Mater.* **10**, 2753 (1998).

[3] Y. M. Chiang, D. P. Birnie, W. D. Kingery, *Physical Ceramics*. John Wiley and Sons, Inc, New York, 1997.

[4] Y. Gim, T. Hudson, Y. Fan, C. Kwon, A. T. Findikoglu, B. J. Gibbons, B. H. Park, Q. X. Jia, *Appl. Phys. Lett*. 77, 1200 (2000).

[5] X. Wei, H. Yan, T. Wang, Q. Hu, G. Viola, S. Grasso, Q. Jiang, L. Jin, Z. Xu, M. Reece, *J. Appl. Phys.* **113**, 024103 (2013).

[6] X. Luo, J. Wang, M. Dooner, *J. Clarke, Appl. Energy* **137**, 511 (2015).

[7] X. Hao, *J. Adv. Dielectr.* **3,** 330001 (2013).

[8] Q. Tan, P. Irwin, Y. Cao, *IEEJ Trans. Fund. Mater.* **126**, 1153 (2006).

[9] J. Laghari, W. Sarjeant, *IEEE Trans. Power Electr.* **7**, 251 (1992).

[10] Q. Li, K. Han, M. R. Gadinski, G. Z. Zhang, Q. Wang, *Adv. Mater.* **26,** 6244 (2014).

[11] Z. Kailun, D. Yu, X. Haojie, Z. Qingfeng, L. Yinmei, H. Haitao, H. Yunbin, *Material Research Bulletin* **113,** 190 (2019).

[12] K. Uchino, *Ferroelectric Devices*, CRC Press, 2nd edn., New York, 2010.

[13] H. Landolt, R. Bornstein, *Ferroelectrics, and related substances: A, Oxides*, Springer-Verlag, New York, 1981.

[14] Y. Gim, T. Hudson, Y. Fan, C. Kwon, A. T. Findikoglu, *Appl. Phys. Lett.* 77**,** 1200 (2000).

[15] J. F. Scott, *Ferroelectric Memories*. Berlin, Springer, New York, 2000.

[16] B. A. Strukov, A. P. Lavanyuk, *Ferroelectric Phenomena in Crystals*. Springer, 1998.

[17] X. Qi, T.L. Michael, H. Xuechen, X. Juan, L. Zhang, H. Hao, H. Liu, *Ceram. Int.* **42**, 9728(2016).

[18] Q. Yun, L. Ying, L. Xiaoyu, H. Haibo, *J. Alloys Comp.* **797**, 348(2019).

[19] Q. Ning, D. Hon, H. Xihong, *J. Mater. Chem. C* **26**, 7993(2019).

[20] X. Jinglong, D. Zhonghua, D. Xiangdong, F. Xing, L. Weiguo, Z. Lin, L. Jinglei, *J. Mater. Sci.* **55**, 13578(2020).

[21] P. Satyanarayan, C. Aditya, V. Rahul, *Mate. Res. Express***1**, 045502(2014).

[22] Y. Zhonghua, S. Zhe, H. Hua, Y. Zhiyong, C. Minghe, Z. Shujun, T. Michael, Lanagan, L. Hanxing, *Adv. Mater.* **29**, 1601727(2017).

[23] O. Yuji, S. Yoshikazu, *JCS Japan* **122**, 728 (2014).

[24] M. Sverre, T. Selbach, M. Tybell, E. Mari-Ann, G. Grande, *Adv. Mater*. **20**, 3692(2008).

[25] V. Giuseppe, N. Huanpo, W. Xiaojong, D. Marco, A. Arturas, *J. Appl. Phys*. **114**, 014107(2013).

[26] N. Funsueb, A. Limpichaipanit, A. Ngamjarurojana, *J. Phys. Conf. Ser.* **1144**, 012133(2018).

[27] M. Zhang, Y. Haibo, Y. Yiwen, L. Ying, *Chem. Eng. J.* 425, 131465(2021).

[28] F. Yuzhu, Z. Zhiyong, R. Liang, D. Xianlin, *J. Eur. Ceram. Soc.* **39**, 4770(2019).

[29] G. Jing, Z. Lei, L. Qing, W. Xuping, Z. Shujun, F. Jing-Feng, *J. Am. Ceram. Soc.*1, 15780(2018).

[30] Z. Liu, T. Lu, R. Withers, Y. Liu, *Adv. Mater. Technol.* **10**, 1002(2018).

[31] J. Abdullah, L. Hanxing, H. Haob, Y. Zhonghua, C. Minghe, S. Arbab, T. Muhammad, *J. Mater. Chem. C* **10,** 1039(2020).

[32] R. Naik, J.J. Nazark, *Phys. Rev. B* **61**, 11367(2000).

[33] C. Q. Sun, (2007), *Solid State Chemistry* **35**, 1(2007).

[34] L. Ming-li, L. Hui, X. Ming-Xia, *Mater. Chem. Phys* **112**, 337(2008).

[35] W. Xiao, X. Gang, R. Zhaohui, W. Yonggang, H. Gaorong, *J. Crystal Growth* **310**, 4132(2008).

[36] K. Thomas, H. Starke, S.V. Gary, *Sensor Actuator B* **88**, 227(2003).

[37] https://aedbaeddebbefddk.blogspot.com/2018/05/capacitor-electric-field.html.

[38] X. Hao, *J. Adv. Dielectr.***3**, (2013)1330001.

[39] P. Hao, K. Ahmed, L. Yuan-Hua, N. Ce-Wen, L. Judith L, M.D. MacManus, *Nanoscale* **12**, 19582(2020).

[40] L. Fredin, Z. Li, M. Ratner, M. T. Lanagan, T. J. Marks, *Adv. Mater.* **24**, 5946 (2012).

[41] S. Chao, F. Dogan, *Mater. Lett.* **65**, 978(2011).

[42] Z. Song, H. Liu, H. Hao, S. Zhang, M. Cao, Z. Yao, Z. Wang, W. Hu, Y. Shi, B. Hu, *IEEE Trans. Ultrason Ferroelectr. Freq. Control* **62,** 609 (2015).

[43] T. Wu, Y. Pu, T. Zong, P. Gao, *J. Alloys Compd.* **584**, 461(2014).

[44] N. Fletcher, A. Hilton, B. Ricketts, *J. Phys. D.: Appl. Phys.* **29**, 253(1996).

[45] Y. Wang, Z. Shen, Y. Li, Z. Wang, W. Luo, Y. Hong, *Ceram. Int. **41**,* 8252(2015).

[46] M. Roy, J. K. Nelson, R. K. Mac Crone, L. S. Schadler, *J. Mater. Sci.* **42***,* 3789(2007).

[47] J. Qian, P. Yong-Ping, W. Chun, G. Zi-Yan, Z. Han-Yu, *Ceramic International* **10,** 1016 (2017).

[48] M.A Pope, I.A. Aksay, Adv. Energy Mater. **5**, 1500124(2015).

[49] M.L.B. Rao, Inventor MALLORY & CO INC PR, assignee, Organic electrolyte cells, United States patent 3413154, 1968.

[50] Dominick A. Nole, S. Vladimir Moss, Inventor Aerojet-General Corporation, assignee, Basttery Rmploying Lithium–Sulphur Electrodes with Non-aqueous Electrolyte, United States patent 3532543, 1970.

[51] P.G. Bruce, S.A. Freunberger, L.J. Hardwick, J.M. Tarascon, Nat. Mater. **11**,19 (2012).

[52] L. Ji, S. Zhen-Hua, L. Feng, C. Hui-Ming, Energy Storage Materials **2**, 76(2015).

[53] D. Zheng, X.R. Zhang, J.K. Wang, D.Y. Qu, D.Y. Qu, J. Power Sources **301,** 312(2016).

[54] D. Zheng, D. Liu, J.B. Harris, T. Ding, J. Si, S. Andrew, D. Qua, X.Q. Yang, D. Qu, ACS Appl. Mater. Interfaces **9**, 4326(2017).

[55] D. Peramunage, S. Licht, Science **261**, 1029(1993).

[56] G. Xu, B. Ding, J. Pan, P. Nie, L. Shen, X. Zhang, J. Mater. Chem. **A 2**, 2662(2014).

[57] R. Van Noorden, Nature **26**, 507 (2014).

[58] H. Yamin, E. Peled, J. Power Sources **9,** 281(1983).

[59] X. Zhang, H. Xie, C.S. Kim, K. Zaghib, A. Mauger, C.M. Julien, Materials and Engineering R **1**, 121(2017).

[60] S. Walus, C. Barchasz, J.F. Colin, J.F. Martin, E. Elkaim, J.C. Lepretre, F. Alloin, Chem. Commun. **49**, 7899 (2013).

[61] B.M.L. Rao, J.A. Shropshire, J. Electrochem. Soc. **128**, 942(1981).

[62] R.C. Weast, M. J. Astle, W. H. Beyer, *CRC Handbook of Chemistry and Physics*, Vol. *69*. CRC Press, Boca Raton, FL **1988**.

[63] X. Ji, K. T. Lee, L. F. Nazar, *Nat. Mater.* **8,** 500(2009).

[64] R. Yazami, P. Touzain, *J. Power Sources* **9**, 365(1983).

[65] A.K. Padhi, K. Nanjundaswamy, J.B.D. Goodenough, *J. Electrochem. Soc.* **144***,* 1188*(***1997)**.

[66] R. Rauh, F. Shuker, J. Marston, S. Brummer, *J. Inorg. Nucl. Chem.* **39**, 1761(1977).

[67] S. S. Zhang, D. T. Tran, *J. Power Sources **211**,*2012(169).

[68] J. Gao, M. A. Lowe, Y. Kiya, H. D. Abruña, *J. Phys. Chem. C* **115**, 25132 (2011).

[69] E. Peled, A. Gorenshtein, M. Segal, Y. Sternberg, *J. Power Sources **26***, 269 (1989).

[70] Z. Li, J. Huang, B. Yann Liaw, V. Metzler, J. Zhang, *J. Power Sources **254***, 168(2014).

[71] S. Rehman, S. Guo, Y. Hou, *Adv. Mater.* **28**, 3167(2006).

[72] X. Liang, C. Hart, Q. Pang, A. Garsuch, T. Weiss, L. F. Nazar, *Nat. Commun.* **6***,* 5682(2015).

[73] H. J. Peng, Q. Zhang, *Angew, Chem., Int. Ed.* **54**, 11018(2015).

[74] X. L. Ji, K. T. Lee, L. F. Nazar, *Nat. Mater.* **8**, 500(2009).

[75] M. P. Yu, J. S. Ma, H. Q. Song, A. J. Wang, F. Y. Tian, Y. S. Wang, H. Qiu, R. M. Wang, *Energy Environ. Sci.* **9**, 1495(2016).

[76] Z. Y. Cao, B. Q. Wei, *Energy Environ. Sci.***6,** 3183(2013).

[77] A. Manthiram, Y. Z. Fu, S. H. Chung, C. X. Zu, Y. S. Su, *Chem. Rev.* **114***,* 11751(2014)

[78] C. Zhang, W. Liv, Y. Tao, Q. H. Yang, *Energy Environ. Sci.* **8,** 1390(2015).

[79] W. Li, Z. Liang, Z. Lu, X. Tao, K. Liu, H. Yao, Y. Cui, *Nano Lett.* **15,** 7394(2015).

[80] H. Al Salem, G. Babu, C. V. Rao, L. M. Arava, *J. Am. Chem. Soc.* **137**, 11542(2015).

[81] M. R. Morris, S. R. Pendlebury, J. Hong, S. Dunn, J. R. Durrant, *Adv. Mater.* **28,** 7123(2018).

[82] Y. Cui, J. Briscoe, S. Dunn, *Chem. Mater.* **25**, 4215(2013).

[83] X. Keyu, Y. You, Y. Kai, L. Wei, Z. Kun, X. Fei, Y. Mao, K. Shanming, S. Chao, Z. Xierong, F. Xiaoli, W. Bingqing, *Adv. Mater.* **29**, 1(2016).

CHAPTER 2

Experimental methods and characterization techniques

2.1 Overview

This chapter briefly describes the synthesis procedure for the preparation of target, ceramic oxides, and different experimental techniques used for the characterization of these materials.

2.2 Sample preparation

The synthesis of materials and the optimization of their physical properties in the form of ceramics, for specific applications of multifunctional devices (energy storage) are the essential part in the field of materials science. Optimum physical and chemical properties of a ceramic are defined requirements of the end use. For example, even greater challenges confront the ceramics involved in, for example, the development of the ceramic battery and capacitor. Here is a combination of a good understanding of solid-state chemical physical. The basic science of a wide range of physics properties of solid, conductivity, dielectric, optical, piezoelectrical and ferroelectric. Understanding must embrace how the science of ceramics can be exploited to optimize properties, not only through the design of materials composition, but also though the tailoring of microstate and texture. Because the objective is an improved component for some functions a capacitor and battery. Today, there are many advanced techniques available for the synthesis of high purity materials. Ferroelectric materials can be easily synthesized in pellet form.[1]

2.2.1. Synthesis of ceramics

The synthesis within mechanical methods, such as solid-state reaction involves different processes, such as: mixtures, calcination, synthesis. This conventional method in which they are mainly used in the synthesis of polycrystalline ceramic from mixture of oxide. [2] These chemicals must meet a certain application-dependent specification about their purity and grain distribution. Using this method, ceramic is produced at a high temperature by mixing its constituent ingredients in a suitable ratio. The completion of the reaction and the uniformity of the product depend on the size of the particles, the homogeneity of the mixture, and the thermal program. During high-energy ball grinding, the powder particles are flattened, cold-welded, fractured, and repeatedly re-welded. Possible mechanisms that may contribute to material transfer during milling of brittle components may include plastic deformation, which is made possible by (a) local temperature rise, (b) micro deformation in defect-free volumes, (c) surface deformation and (d) state of hydrostatic stress in the powder during grinding. In addition to producing the required particle size distribution, ball milling can also produce a highly active powder that is easier to densify in later process steps. However, it is limited in its efficiency and accuracy in producing controlled sizing of particles below nanometric. As the solid part does not participate in the reaction at room temperature, heat is required for the solid precursors to carry out the reaction.

2.2.1.1. Solid state reaction method

Solid-state reactions have a dense packing structure, the reaction process such as mixing and collision, and the probability of a close encounter reaction are limited by transport, as shown schematically in the Figure 2.1.

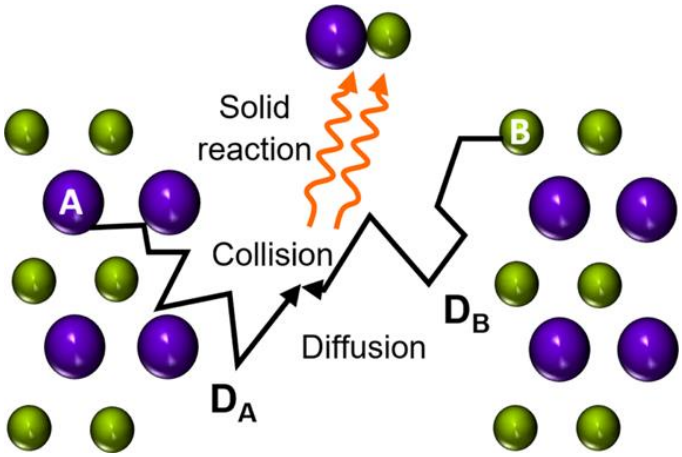

Figure 2.1. *Mixing, collision, and solid-state reaction of solid reactants A and B. [3]*

As discussed, the dominant term of equation 2.1 expresses the correlation between the flux of charged particles, J, and the nonzero ionic diffusion and mass transport. [2,3]

$$J_i^{(2)} \approx -D_i \nabla n_i^{(2)} + \frac{D_i n_i^{(2)}}{KT} q_i E^{(2)} + \frac{D_i n_i^{(0)}}{KT} \langle \left(\frac{n_i^{(1)}}{n_i^{(0)}} \right) q_i E^{(1)} \rangle \ldots\ldots\ldots\ldots\ldots\ldots\ldots\ldots\ldots\ldots\ldots \quad (2.1)$$

Where *J*, *q*, *E*, *k*, *T*, *i*, *n* and *D* the flux of charge particles, the charge of elements, electric filed, Boltzmann's constant, temperature, mobile charge species, concentration, diffusion coefficient, respectively.[3] Period of the oscillation and expanding the *J*, *n*, and *E* to the second order, where the static solutions, the high-frequency fluctuation, and the period-averaged are related to the zero, first, and second order, respectively; for the quasi-stationary flux. As noted, the diffusion of the mobile species can be significantly enhanced by the driving force due to the microwave, i.e., the field induced pondermotive force accelerates diffusion and consequently speeds up the solid-state reaction. It is evident that the pondermotive force can simultaneously densify the granular materials, increase ionic diffusion, and enhance the solid-state reaction rates by enhancing the collision rates. [3,4] Below are the optimized parameters, which are used for the solid-state synthesis obtaining

a very good reaction and densification. Evidence that solid-state reactions can be obtained an optimal classification for applications to energy storage devices.

2.3 Structural and microstructure characterization

Microstructure characterization of advanced ceramics involves qualitative and quantitative analysis of surface topography, porosity, crystal defects, and interfaces. The structure of the surface controls interaction of ceramics with its surroundings, such as adhesion, gas adsorption, and electron exchange, which play an important role in determining overall properties of a material. Pores in ceramic materials originate from incomplete densification during the sintering process. Their presence interferes with functional properties such as mechanical strength, optical transparency, electrical conductivity, and dielectric response. Crystal defects mostly form either because of imperfections during the crystal growth process or because of structural phase transitions. They generally affect most functional properties of materials. So-called extended defects are interfaces that are boundaries between two solids. The most widespread tools for characterization of ceramic microstructures are microscopic techniques involving optical microscopy, different types of electron microscopy, and various scanning-probe methods. This chapter gives a brief introduction of the features of ceramic microstructure and the corresponding techniques for characterizing them.

2.3.1 X-ray diffraction

X-ray diffraction (XRD) is a powerful nondestructive technique for characterizing crystalline materials. To obtain information and analyze on structures, phases, preferred crystal orientations (texture), and other structural parameters, such as average grain size, crystallinity, strain, and crystal defects. Information necessary to optimize and confirm

crystalline structures, necessary to be able to design the devices.[5] XRD topography can easily detect and image the presence of defects within a polycrystalline crystal material, it allows to orient a fraction of the sample with respect to the incident beam, which in turn allows the appearance of diffraction peaks.[5-6] X-ray diffraction is now a common technique for the study of crystal structures and atomic spacing. X-ray diffraction is based on constructive interference of monochromatic X-rays and a crystalline sample. These X-rays are generated by a cathode ray tube, filtered to produce monochromatic radiation, collimated to concentrate, and directed toward the sample (see in Figure 2.2).[7]

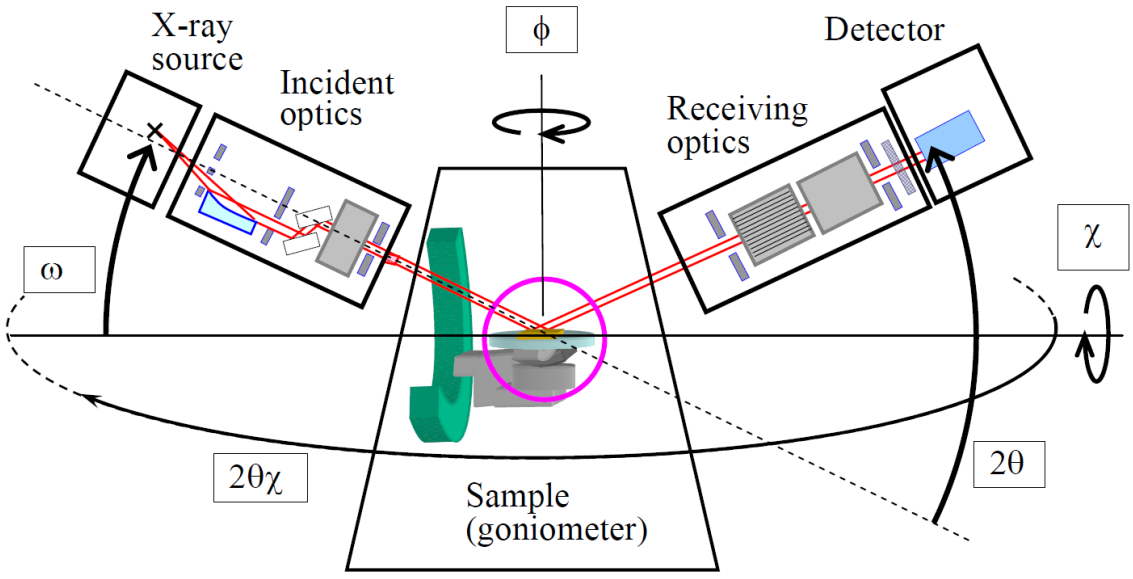

Figure 2.2. *X-ray diffractometer equipped with the 2Θχ axis (SmartLab). Diagram illustration goniometer system.[7]*

In the classic diffraction theory, Bragg diffraction occurs when charged particle or electromagnetic radiation waves with a wavelength comparable to atomic spacing are incident to a crystalline sample. The waves reflected off adjacent scattering centers must have a path difference equal to an integral number of wavelengths. The scattered waves interfere constructively if they remain in phase. Therefore, the path difference between

electron waves reflected from the upper and lower planes in Figure 2.3 is equal to the total length *(AO+BO)*. Assuming the *h k l* planes are spaced a distance d_{hkl} apart and the wave is incident and reflected at angles θ_B, both *AB* and *BC* are equal to $dsin(\theta_B)$, and the total path difference should be equal to $2dsin(\theta_B)$. We can have, *n*, the integer multiple of the smallest G_{hkl} that is allowed, $k=2\pi/\lambda$. [8]

$$2Ksin\theta = G_{hkl} = \frac{2\pi}{d_{hkl}}n \ldots\ldots\ldots\ldots\ldots\ldots\ldots\ldots\ldots\ldots\ldots\ldots \quad (2.2)$$

There can obtain the well-known Bragg's diffraction condition.

$$n\lambda = 2d_{hkl}sin\,(\theta_B) \ldots\ldots\ldots\ldots\ldots\ldots\ldots\ldots\ldots\ldots\ldots\ldots \quad (2.3)$$

n= An integer, the order of reflection,

d_{hkl}=The integer spacing of (*h k l*),

λ =The wavelength of the charged particle or electromagnetic radiation waves,

θ_B=The Bragg angle that is the angle between the incident wave vector and *h k l* lattice planes as shown in Figure 2.3.

h k l=Miller indices

The Bragg angle θ_B is a very important concept in diffraction theory. Wearing to explain electron and X-ray diffraction phenomena. Very strong intensities Bragg peaks are obtained in the diffraction pattern when scattered waves satisfy the Bragg conditions. Angle between incident and reflected waves is $2\theta_B$ as shown Figure 2.3. This equation relates the crystalline structure and the geometric condition for diffraction to occur.[8]

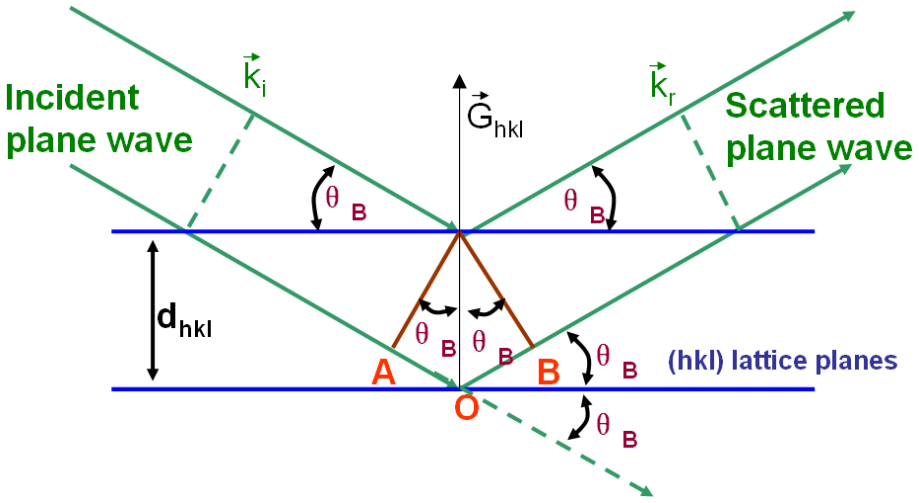

Figure 2.3 *Schematic illustration of Bragg condition and Bragg's law. The path difference between reflected waves to AO+OB.*

To acquire an X-ray diffractogram, the angles 2Θ and Θ are scanned coordinately, simultaneously detecting the intensity of the diffracted beam. Equation (2.2) allows us to calculate d_{hkl} from each angle Θ measured under diffraction conditions. For a crystal structure, there are many sets of planes that satisfy the Bragg condition. In the case of a completely disordered polycrystalline sample, it is possible to observe in the measured 2Θ range the diffractions of all families of atomic planes for which constructive interference conditions are also met. From the analysis of the diffraction pattern of the sample, it is then possible to determine the crystalline structure and the lattice parameters. [5,8]

To generate X-rays in practical diffraction systems, vacuum tubes are used in which a beam of accelerated electrons is incident on an elemental metallic target (Cu in our case). The collision of these electrons with the target causes the expulsion of electrons from one of the internal orbitals of the atom. These empty levels are then occupied by some of the electrons in outermost orbitals, generating in the process photons with energies characteristic of the metal in question. If the empty level belongs to the *K* orbital of the

atom, in the process of occupation we will obtain a photon with characteristic energies of the *K* level, but if it belongs to the *L* orbital then it will be of type *L*, and likewise for the *M* orbital. Within these types there are subtypes. If an electron ejected from the *K* orbital is occupied by an electron from the *L* orbital, we will have a K_α-type X-ray, but if it is occupied by an electron from the *M* orbital, then we have a K_β-type X-ray. If an electron ejected from the *L* orbital is occupied by another from the *M* orbital, we will have an L_α-type X-ray. Now we will have to consider not only which suborbital the electron comes from but also which suborbital it fills, since, except for the *K* orbital, the rest is divided into subshells. So, if an electron ejected from the *K* orbital is occupied by another from the L_3 orbital, a $K_{\alpha 1}$ type X-ray will be obtained, if it is from the L_2 orbital it would be of the $K_{\alpha 2}$ type etc. The equipment used in this work was a Rigaku D/Max Ultima III X-ray diffractometer in Bragg-Brentano (BB), which uses a copper target X-ray tube. The characteristic radiations produced in this tube are mainly $CuK_{\alpha 1}$(λ= 1.5404 Å) and $CK_{\alpha 2}$(λ=1.5418 Å), whose average is called CuK_α (λ=1.5411 Å). A smaller amount of $CuK_{\beta 1}$(λ=1.3921 Å) radiation is also produced. XRD patterns of materials (ceramics and thin films) were collected in the range of 2θ =10˚ to 100˚. [6-8]

Rietveld refinement is conducted by fitting a calculated diffraction pattern to the observed data by adjusting each of the variables that describe the diffraction. Rietveld computations are relatively intensive, and require minimizing the sum of the weighted, squared differences between observed and calculated intensities at every step in a digital powder pattern. The Rietveld method requires knowledge of the approximate crystal structure of all phases present in the specimen. The successive refinement modifies different structural and microstructural parameters of the simulated pattern to fit

experimental diffraction patterns. The calculated intensity $Y_{cal,i}$ at each step in 2Θ is then compared to the observed intensity $Y_{obs,i}$, and the different between the two is minimized by changing certain parameters of the model. This is most done by least-squares refiment in which the quantity minimized is,

$$R_{wp} = \sqrt{\frac{\sum_{i=1}^{N} W_i(Y_{obs,i} - Y_{cal,i})^2}{\sum_{i=1}^{N} W_i Y_{obs,i}}} \quad \text{..... (2.4)}$$

Or a quantity such as goodness of fit (GoF) or χ, which relates R_{wp} to the statistically expected value R_{exp}.

$$GoF = \chi = \frac{R_{wp}}{R_{exp}} = \sqrt{\frac{\sum_{i=1}^{N} W_i(Y_{obs,i} - Y_{cal,i})^2}{N-P}} \quad \text{..... (2.5)}$$

Where N is the number of data point and P the number of parameters. χ should tend to 1a good refiment. Least-squares uses a $1/((Y_{obs,i})^2)$ weighting where $\sigma(Y_{obs,i})$ is the experimental uncertainty in $Y_{obs,i}$. [9,10]

In this thesis work, the Rietveld refinement was performed using the analyses of the XRD patterns were carried out using FullProf suite software 7.70 (Version April 2022).[11] Peaks were refined using a function (Pseudo Void) and linear background was considered. In the refinement process, the zero correction, scale factor, background, unit cell parameters, atomic positions, thermal parameters, and half-width parameters (U, V, and W) were varied. The atoms remained fixed throughout the refining process.

2.3.2 Raman spectroscopy

Raman scattering spectroscopy is important for the study of phase transitions in ferroelectric materials and as a tool to characterize smooth modes and features related to

order-disorder phenomena. The dynamic behavior of phase transitions and their sensitivity to temperature and doping can be easily elucidated by Raman scattering measurements. Perovskite-ABO_3 ferroelectric materials in ceramic, pellet, and powder for energy storage applications (capacitor and batteries). The ferroelectric properties are highly dependent on the preparation of the materials, the chemical composition, and the microstructures (crystal structures, orientation, grain size, domain structure, and surface roughness). Ferroelectric Micro-Raman scattering provides a useful link between the phonon spectrum and the microstructure of materials in the form of ceramic and powder.

Raman effect when the light energy is $E=hv$, is incident on a molecule it is scattered whit the same amount of energy, called Rayleigh scattering, if the energy of the scattering light is lost or gained, generally due to molecular vibrations, is called inelastic scattering Raman scattering. If the scattered light lost energy from that of the incident light, it is Stokes Raman scattering and if it gained energy is called anti-stokes Raman scattering; frequency of inelastically scattered photons shifted either up (anti stokes) or down (stokes) with respect to the incident photons. The elastically scattered photons have similar frequency as of incident photons and the scattering process is called Rayleigh scattering, see in Figure 2.4. Raman scattering, (C) anti-Stokes Raman scattering, (D) Stokes Raman scattering. S_o, ground state, S_1 excited state, E_L energy of incident light, E_s scattered energy, $h\omega_v$ vibrational energy. [12]

The scattering of light is considered as the redirection of light, in the form of an electromagnetic (EM) wave, when interacting with matter, the electronic orbits within the constituent molecules are periodically perturbed with the same frequency (ν_0) as the field. electrical of the incident wave. The oscillation or perturbation of the electron cloud results

in a periodic separation of charge within the molecules, which is called the induced dipole moment. Most of the scattered light is emitted at the same (υ_0) frequency as the incident light, a process called elastic scattering. However, as explained below, the additional light is scattered at different frequencies, a process known as inelastic scattering. Raman scattering is one such example of inelastic scattering.

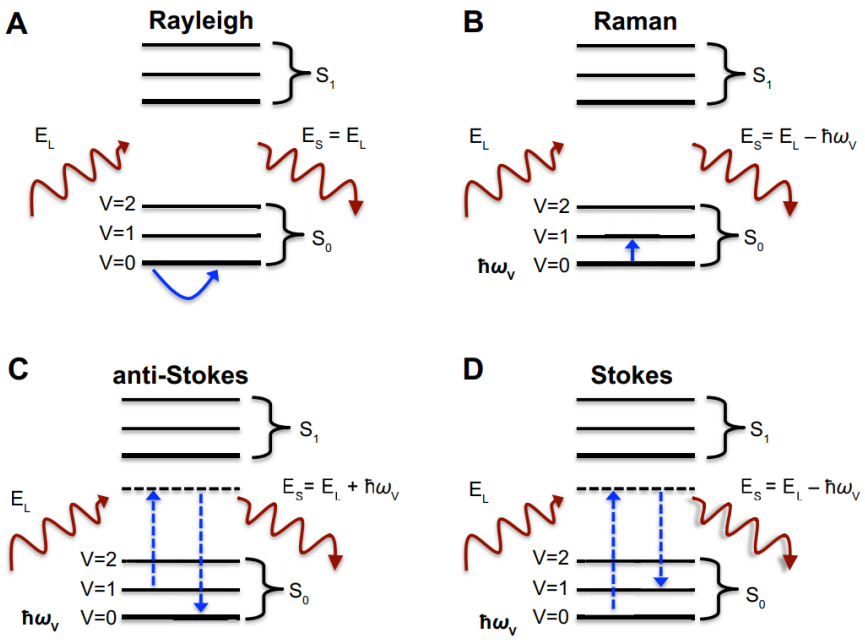

Figure 2.4. *(A) Jablonski energy diagram for Rayleigh scattering, (B) Linear spontaneous [12]*

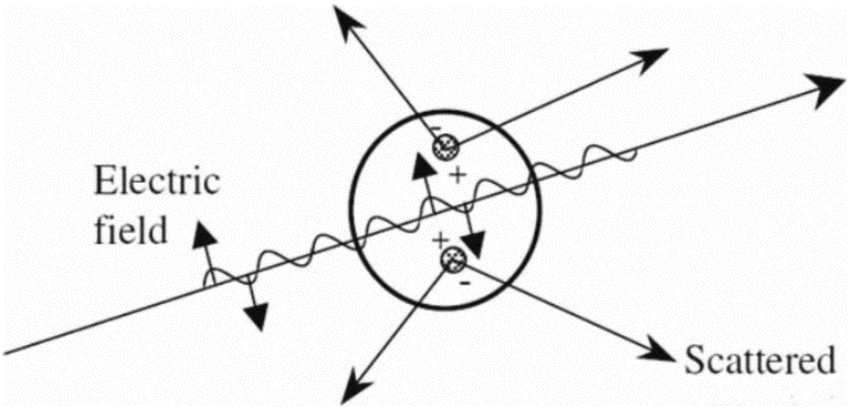

Figure 2.5. *Light scattering by an induced dipole moment.*

As discussed above, an incident electromagnetic wave induces a dipole moment during the light material interaction. The strength of the induced dipole moment, P, is given by.

$$P = \alpha\bar{E} \quad \text{(2.6)}$$

where polarizability and E is the strength of electric field of the incident EM wave, the polarizability is a material property that depends on the molecular structure and nature of the bonds; for the incident EM wave, the electric field may be expressed as

$$\bar{E} = E_0\cos(2\pi\gamma_0 t) \quad \text{(2.7)}$$

$\upsilon_{0,}$ is frequency (Hz) the incident EM ($\upsilon_{0,} = c/\lambda$)

Reem place (2.6) into (2.7) yields the time dependent induced dipole moment,

$$P = \alpha_0 E_0\cos(2\pi\upsilon_0 t) \quad \text{(2.8)}$$

The power to perturb the local electron cloud of a molecular structure is related to the relative location of the atoms in their individual positions. Understanding polarizability as a function of the instantaneous position of the atoms. In molecular bonds, individual atoms are confined to specific modes of vibration, in which the vibrational energy levels are quantized, obtaining the vibrational energy given by the equation.

$$E_{vib} = \left(j + \frac{1}{2}\right) h\upsilon_{vib} \quad \text{(2.9)}$$

j =is the vibrational quantum number (j=0,1,2…)

υ_{vib}= frequency of vibrational model

h= Plank constant.

The physical displacement *dQ* of the atoms with respect to their equilibrium position due to the mode of vibration is shown in the equation.

$$dQ = Q_0 \cos(2\pi \upsilon_{vib} t) \ldots\ldots\ldots\ldots\ldots\ldots\ldots\ldots\ldots\ldots\ldots\ldots \quad (2.10)$$

Q_0: maximum displacement about the equilibrium position.

To account for such small displacements, the polarizability is approximated using the Taylor series.

$$\alpha = \alpha_0 + \frac{\partial \alpha}{\partial Q} dQ \ldots\ldots\ldots\ldots\ldots\ldots\ldots\ldots\ldots\ldots\ldots\ldots\ldots\ldots\ldots\ldots \quad (2.11)$$

$\alpha_0 =$ polarization of the molecular mode at equilibrium poison

The vibrational displacement of equation (9), can represent the polarization as

$$\alpha = \alpha_0 + \frac{\partial \alpha}{\partial Q} Q_0 \cos(2\pi \nu_{vib} t) \ldots\ldots\ldots\ldots\ldots\ldots\ldots\ldots\ldots\ldots\ldots \quad (2.12)$$

Substituting equation (2.12) into equation (2.8), we get

$$P = \alpha_0 E_0 cos(2\pi \upsilon_0 t) + \frac{\partial \alpha}{\partial Q} Q_0 E_0 \cos(2\pi \upsilon_0 t) \cos(2\pi \nu_{vib} t) \ldots\ldots\ldots\ldots\ldots \quad (2.13)$$

Applying trigonometric identity, we formulate the equation.

$$P = \alpha_0 E_0 \cos(2\pi \upsilon_0 t) + \left(\frac{\partial \alpha}{\partial Q} \frac{Q_0 E_0}{2}\right) \{\cos[2\pi(\nu_0 - \upsilon_{vib})t] + \cos[2\pi(\nu_0 + \upsilon_{vib})t\} \ldots \quad (2.14)$$

Analysis of the above equation shows the induced dipole moments created at three different frequencies, namely υ_0, $(\nu_0 - \nu_{vib})$ and $(\nu_0 + \nu_{vib})$, obtaining the scattered radiation at these three frequencies. The first scattered frequency corresponds to the incident frequency, hence, is elastic scattering (Mie or Rayleigh), while the latter two frequencies are shifted to lower or higher frequencies and are therefore inelastic processes.

The scattered light in these latter two cases is referred to as Raman scattering, with the down-shifted frequency (longer wavelength) referred to as Stokes scattering, and the up-shifted frequency (shorter wavelength) referred to as anti-Stokes scattering. Raman was the first to describe this type of inelastic scattering, for which he was awarded the Noble prize in physics in 1930. Necessary condition for Raman scattering is that the term $\frac{\partial \alpha}{\partial Q}$ must be non-zero. The constraint can be interpreted physically as that the vibrational displacement of the atoms corresponding to a particular vibrational mode result in a change in polarizability. [13,14]

2.3.2.1 Raman process

In Raman spectroscopy experiments, a laser source is used to generate a monochromatic photon flux in the sample, and the scattered photons are scattered and recorded, resulting in distinct peaks corresponding to lost (Stokes) or gained (anti) photons. -Stokes), the energy generated from the vibrational states ($\hbar\omega_v$) is shown in the Figure 2.4 . The Stokes peak corresponds to a process in which the system is initially in its ground state, while the anti-Stokes peak already requires a system with excited states. This is the reason why the anti-Stokes peak has, in general, a lower intensity. Therefore, in standard Raman spectroscopy only the Stokes peaks are recorded. Then we can introduce the most used equation in spectroscopy, where the spectral position of the Raman peaks is recorded in cm^{-1}. However, the spectral position of the Raman peaks with respect to the incident photon is independent of the latter. Therefore, it is more convenient to represent the Raman spectra not in terms of energy (frequency or wavelength), but in terms of the so-called Raman shift, as shown in equation 2.14. where λ_i is the wavelength of the incident photon and λ_s the wavelength of the scattered photon, corresponding to the Raman peak. [13,14]

$$\text{Raman shift}(\text{cm}^{-1}) = \left(\frac{1}{\lambda_i(\text{nm})} - \frac{1}{\lambda_s(\text{nm})}\right) \times 10^7 \quad \text{..... (2.15)}$$

2.3.3 Scanning electron microscopy

The combination of scanning electron microscopy (SEM) and energy dispersive X-ray spectroscopy (EDX) yields elementals maps, which can be processed by means of digital image analysis to separate the brick structure into single grain images. The single grain geometries obtained, the chemical composition can be evaluated through the EDX elemental mappings, which can then be compared with the preliminary determined by PXRD mineral phases, allowing complete identification and quantification of all material phases.[15]

The scanning electron microscope (SEM) has earned a reputation as the most widely used high-performance imaging technology available for using a focused beam of high-energy electrons to generate a variety of signals at the surface of solid specimens. The signals that derive from electron-sample interactions reveal information about the sample including external morphology (texture), chemical composition, and crystalline structure and orientation of materials making up the sample. The Figure 2.6 shows all the interactions that occur when the electron beam hits the sample.

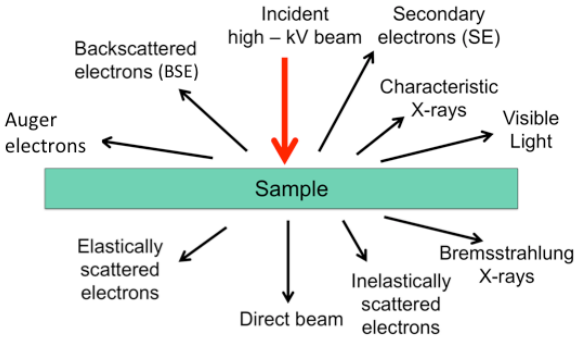

Figure 2.6. *The signals generated when electron beam strikes the sample.*

Accelerated electrons in an SEM carry significant amounts of kinetic energy, and this energy is dissipated as a variety of signals produced by electron-sample interactions when the incident electrons are decelerated in the solid sample. Two main signals that are commonly collected are the secondary electrons and back-scattered electrons. These signals include secondary electrons produce SEM images, backscattered electrons (BSE), diffracted backscattered electrons used to determine crystal structures, photons characteristic X-rays that are used for elemental analysis and continuum X-rays, visible light cathodoluminescence, and heat. Also, secondary electrons and backscattered electrons are commonly used for imaging samples: secondary electrons are most valuable for showing morphology and topography on samples and backscattered electrons are most valuable for illustrating contrasts in composition in multiphase samples. SEM analysis is non-destructive; that is, x-rays generated by electron interactions do not lead to volume loss of the sample, so it is possible to analyze the same materials repeatedly. [15,16]

The surface morphology of the sintered pellets was observed using scanning electron microscopy (SEM) (model: JEOL/MP) equipped with a backscattered electron detector, operated at an accelerating voltage of 20 kV and magnifications (high and low). SEM-based energy dispersive X-ray spectra (EDS) (model: JSM-IT500HR-JEOL) were measured from the surface of the sintered pellets and electrode to infer their chemical compositions.

2.4 Optical studies by ultraviolet-visible spectroscopy

The analysis of spectroscopy through the measurement and interpretation of spectra that arise from the interaction of electromagnetic radiation with matter. Methods differ with respect to the species to be analyzed (eg, molecular or atomic spectroscopy), the type of

radiation-matter interaction to be monitored (eg, absorption, emission, or diffraction), and the region of the electromagnetic spectrum used in the analysis. Spectroscopic methods are very informative and are widely used for both quantitative and qualitative analyses. Spectroscopic methods are based on the absorption or emission of radiation in the ultraviolet (UV), visible (Vis) and infrared (IR) frequency ranges. Optical spectroscopy is useful for understanding the different processes when light interacts with photovoltaic materials. The photon absorption process can take place through fundamental absorption between the valence and conduction bands, or through impurity states. For fundamental absorption, it can be direct or indirect. These processes can be investigated using optical absorption spectroscopy. Ultraviolet and visible spectroscopy (UV-Vis) is called absorption or reflectance spectroscopy in the ultraviolet-visible spectral region and is a useful characterization technique for studying the absorption, transmission, and reflectivity of materials. This tool is generally used to study the optical properties of materials in the wavelength range from 190 to about 2500 nm. [17,18]

The Bouguer-Lambert-Ber law the mathematical-physical basic of light-absorption measurements on gases and solutions in the UV-Vis and IR-region:

$$\lg\left(\frac{I_0}{I}\right) = \lg\left(\frac{100}{T(\%)}\right) \cong A_{\overline{\upsilon}} = \varepsilon_{\nu}.c.d \quad \text{……...……. (2.16)}$$

Were,

$A_{\overline{\nu}} = \lg\left(\frac{I_0}{I}\right)_{\overline{\nu}}$ is the absorbance.

$T_{\overline{\nu}} = \frac{I}{I_0} * 100$ in % is the transmittance.

$\varepsilon_{\overline{\upsilon}}$ is the molar decadic excitation coefficient.

I_0 is the intensity of the monochromatic light entering the sample and I is the intensity of this light emerging from the sample, c is the concentration of the light- absorption substance and d is the path length of sample in cm. [17]

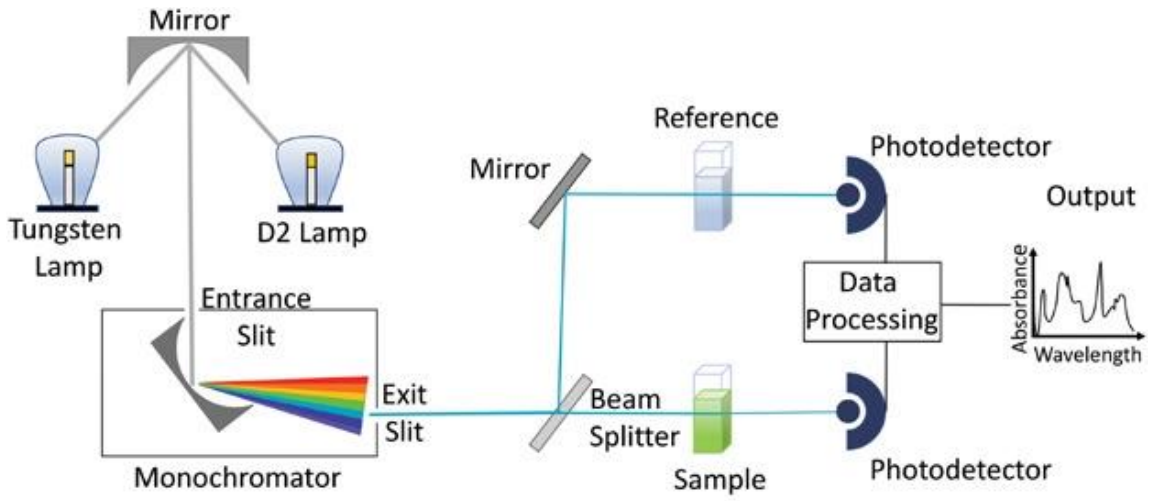

Figure 2.7. *Schematic Diagram of Double Beam UV-Vis Spectrometer.*

La espectroscopia óptica en el rango de luz UV-Vis se aplica ampliamente en casi todos los segmentos de investigación. The main parts of a UV-Vis spectrometer are a light source, a sample holder, a diffraction grating on a monochromatic, or a prism to separate the different wavelengths of light and a detector as shown in Figure 2.7. Single Photodiode and Photomultiplier Detectors Tubes are used with scanning monochromators, to filter light from a single wavelength arriving at the detector at the same time. The scanning monochromator proceeds the diffraction grating to "pass through" each wavelength so that its intensity can be measured as a function of wavelength. A spectrometer can be a single beam or double beam. Samples for the UV/Vis spectrometer are usually liquids, although the absorbance of gases and even solids can also be measured. [17,18]

The band gaps of the samples were estimated from UV-Vis absorbance spectra that were measured from the polished surface of the pellets in the energy range from 0.3 to 1.9 eV

employing a Fourier transform UV-Vis-infrared spectrometer (Agilent Technologies, Cary 100-bio).

2.5 Electrical characterization

2.5.1 Ferroelectric properties

The ferroelectric hysteresis loops (P-E loops) of the studied materials were measured using a ferroelectric tester (Radiant Technologies, Inc.). For the ferroelectric measurement in pellet, initially very small area electrodes were fabricated using silver paint. The set-up consists of a ferroelectric tester, an optical microscope, a probe station, and control PC. The P-E loops were measured in a wide range of voltage (100-4000 V) and frequency (50Hz). The ferroelectric hysteresis loops were measured at 50 Hz using an automatic P-E hysteresis loop tracer system (RT6000 HVS Radiant Technologies Inc.) that utilizes a modified Sawyer Tower test circuit to reduce noise by using virtual ground.

2.5.2 Leakage characteristics

Measurement of the current-voltage (I-V) curves were carried out at room temperature using a Keithley electrometer (model #2401) with the top silver-painted electrode DC biased and the bottom silver painted electrode grounded. The leakage current is an important characteristic of pellet ferroelectric capacitors. The leakage current measurements were performed as a function of applied dc voltage and time held under a have field. Current measurements versus applied voltage typically involved increasing the voltage to ±200 V with a ±1.0 V step and a 60 sec hold at each voltage. For the current density measurements with respect to time, a selected bias voltage was held for a period ranging from 1000 to 10,000 seconds.

Dielectric materials applied to capacitors are not ideal insulators. A small DC current can flow, or "leak" through the dielectric material for various reasons specific to each dielectric. As a result, when a capacitor is charged to a certain voltage, it will slowly lose its charge. As it loses its charge, the voltage between the capacitor's electrodes will drop. The leakage current and the insulation resistance in relation in lay de Ohm:

$$R = \frac{V}{I} \quad \text{(2.17)}$$

$$I = \frac{V}{R} \quad \text{(2.18)}$$

The values of resistance (R), Voltage (V) and Current (I) are related, for the use of the terms leakage current and insulation resistance will vary according to the type of dielectric. A relatively large leakage is called leakage current. It is improved by using ceramic capacitors which have a very small leakage current. So, the effect is quantized as an insulation resistance.[19]

2.6 Electrochemical characterization

2.6.1 Positive electrode and cell assembly

Electrode prepared with a composite ($S_{40}BST1_{40}CB_{10}$+$PVDF_{10}$), coating a mixture of 40 wt.% sulfur, 40 wt.% $Ba_{0.9}Sr_{0.1}TiO_3$, Carbon black 10 wt.% and 10 wt.% polyvinyl fluoride (PVDF) binder in a 30-micrometer gauge - Hick to aluminum foil. Electrochemical performance data of the electrode were obtained in type CR2032 coin cells (1.6 cm^2 electrode area) with a lithium metal counter electrode, a Celgard®2500 separator and liquid electrolyte containing 1M LiTFSI+2 wt.% $LiNO_3$ in DOL+DME. The coin cells were assembled in a glove box under an Ar-atmosphere, applying 25µL of electrolyte. The coin cells were manufacture as indicated in al Figure 2.8, applying a pressure of 8.5 Psi.

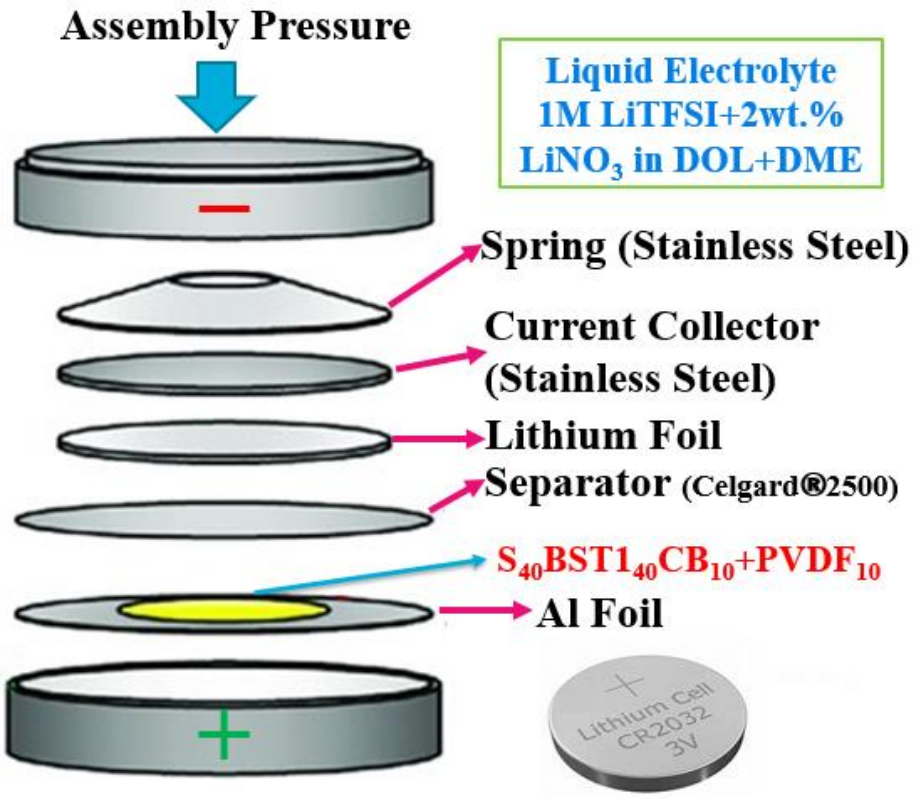

Figure 2.8 *Schematic of Assembly Battery Coin Cell.*

2.6.2 Charge-discharge

The discharging and charging behaviors of the Li/S cells were examined with a battery cycler at room temperature, using battery analyzer model BST8-WA (1 mA). Discharge-charge profiles, specific capacity, and coulombic efficiency in function cycle number spectra of battery $S_{40}BST_{40}CB_{10}$+$PVDF_{10}$ cathode at current densities 50-300 mA/g. The amount of the charge and discharge are very easy to keep track of it the current both ways are keeping constant in such a case total charge accumulated or spent is proportional to time spent charging or recharging for the discharge half of the cycle, this means using a variable load resistance which must be periodically adjusted in step with diminishing cell voltage.

The maximum specific capacity of the intercalation electrodes (C_{max}, in units of mAh/g) is determined by the number of electrons injected or removed during the cycle and the molecular weight of the insertion material according to Equation 2.19:

$$C_{max} = \frac{nF}{3.6 \times MW} \quad \text{(2.19)}$$

Here n is the number of electrons inserted per formula unit of reactant, F is the Faraday constant, MW is the molecular weight of the reactant, and 3.6 is the conversion factor between coulombs and milliamp-hours (mAh), the preferred unit for capacity. At the bench scale, the capacity will be reported with respect to the weight of the active material, which is useful to determine how much material is being utilized. However, at the cell and pack level, the practical energy density will be much lower, owing to the weight of inactive materials. [20]

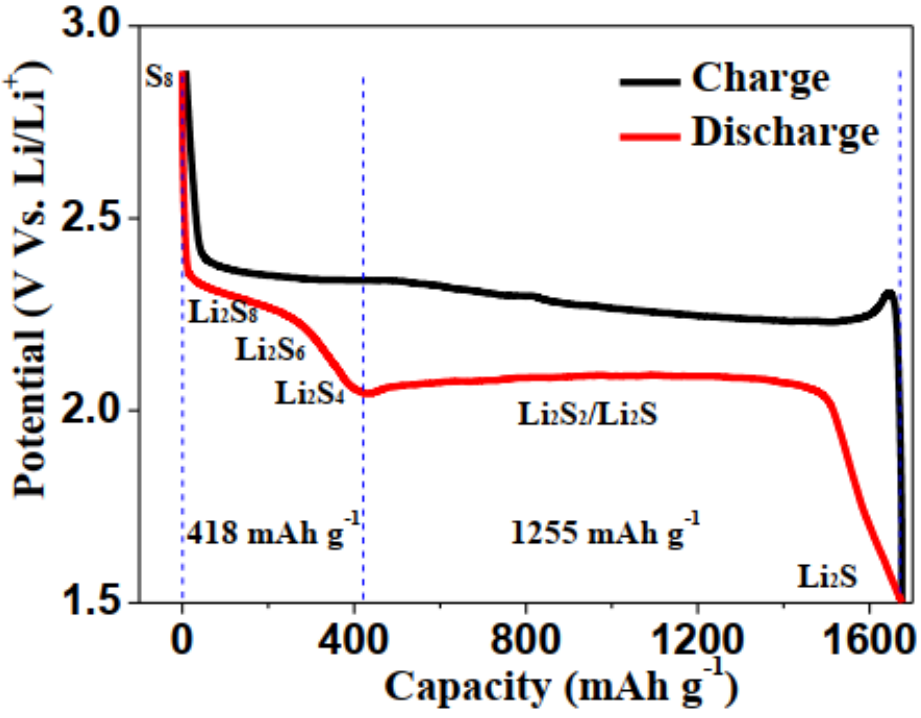

Figure 2.9. *The typical charge-discharge curve of lithium-sulfur batteries.*

As Figure 2.9 shown, at the early discharge process, S_8 obtains the Li-ions and electrons to form a series of long-chain lithium polysulfide species ($S_8 \rightarrow Li_2S_8 \rightarrow Li_2S_6/Li_2S_4$). Since this process is a multiple reaction which just obtains 4 electrons for per S_8, the corresponding voltage plateau is sloping and just contributes 25% of the theoretical capacity of sulfur (418 mAh g^{-1}). At subsequent discharge process, Li_2S_4 is further lithiated and forms short-chain sulfide species ($Li_2S_4 \rightarrow Li_2S_2/Li_2S$). Because this process is individual reaction which gets 12 electrons for per S_8, the corresponding voltage plateau is flat and contributes to 75% of the theoretical capacity of sulfur (1255 mAh g^{-1}). [21]

2.6.3 Cyclic voltammetry (CV)

The analysis of the discharge/charge curves, CV shows a typical behavior of Li-S batteries, measurement was performed at as scan rate of 0.05 mVs^{-1}. The first reduction peak at 2.4~2.2 V involves the reduction of solid S_8 to soluble Li_2Sn ($3 \leq n \leq 8$), and the second reduction peak at 2.1~1.9 V is related to the reduction of Li_2Sn to Li_2S_2/Li_2S. where the two-step reduction process is reflected in the discharge curve of two plateaus, as shown in the Figure 2.10. [22,23] During anodic scanning, the peaks may overlap at 2.2~2.6V, corresponding to the oxidation of lithium sulfide to LiPs/sulfur. In most cases, the redox reactions undergo a process like that described above, leading to similar descriptions of the CV curves. For L-S batteries with Li_2S as the starting material, it is generally charged to 3.5 V firstly, when the original Li_2S electrode must get over a large over-potential barrier to get oxidized to short chain polysulfide, reflecting a broad oxidation peak at 3.0-3.2 V. [23] The short-chain polysulfide is then further oxidized to long-chain polysulfide, corresponding to a long charge process. The following electrochemical redox processes are

the same as that with S_8 cathode, which can be seen from both the CV curves and voltage profiles in Figure 2.10.

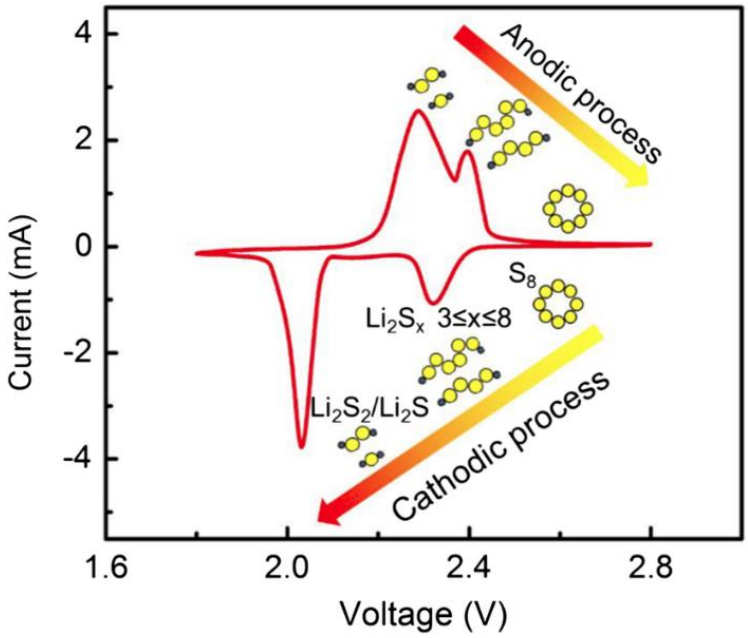

Figure 2.10. *CV curves typical Li-S Batteries at a scanning rate of 0.1 mVS^{-1}. [23]*

2.6.4 Electrochemical impedance spectroscopy

There are many advantages to using electrochemical impedance spectroscopy (EIS) to understand the power delivery capacity in Lithium-Sulfur battery System. EIS performance using an electrochemical workstation Potentiostat/Galvanostat/ZRA (model-26081). For the EIS test, the alternative current amplitude was ±0.05 mV, and the applied range was 0.01 to 10 MHz. To obtain more detailed evolution of impedance spectra during the discharge/charge process, the test interval for each potential was 0.01 V.

The EIS technique analyzes measurements of resistance (R), capacitance (C), and inductance (L) by monitoring the response of the electrochemical cell when an AC voltage is applied. When a DC voltage is applied, the relation among R, V and I satisfy Ohm's law, as shown in Figure 2.11(a). Similarly, when an AC voltage is applied to an electrochemical

cell, the impedance Z(ω) (ω= 2πf is the angular frequency of the applied AC voltage) can be expressed as V(ω) / I(ω), which is the equation for Ohm's law in an AC circuit. Therefore, the impedance is defined as the resistance that interrupts the current flow when an AC voltage is applied to the circuit.[24] These interruptions are represented by various circuit elements, such as resistors, inductors, and conductors, which constitute the overall impedance in a circuit. In an actual system, the electrochemical cell contains various circuit elements with diverse combinations. Thus, it is more accurate to use the concept of impedance than a circuit model consisting solely of a resistor to represent an electrochemical system. Additionally, when V is applied with the angular frequency ω, V and I have a phase difference of Ø. Therefore, the above V and I values in the AC circuit can be expressed by the equation shown in Figure 2.11(b). In these equations, V_m and I_m represent the maximum values of V and I, respectively. [24,25]

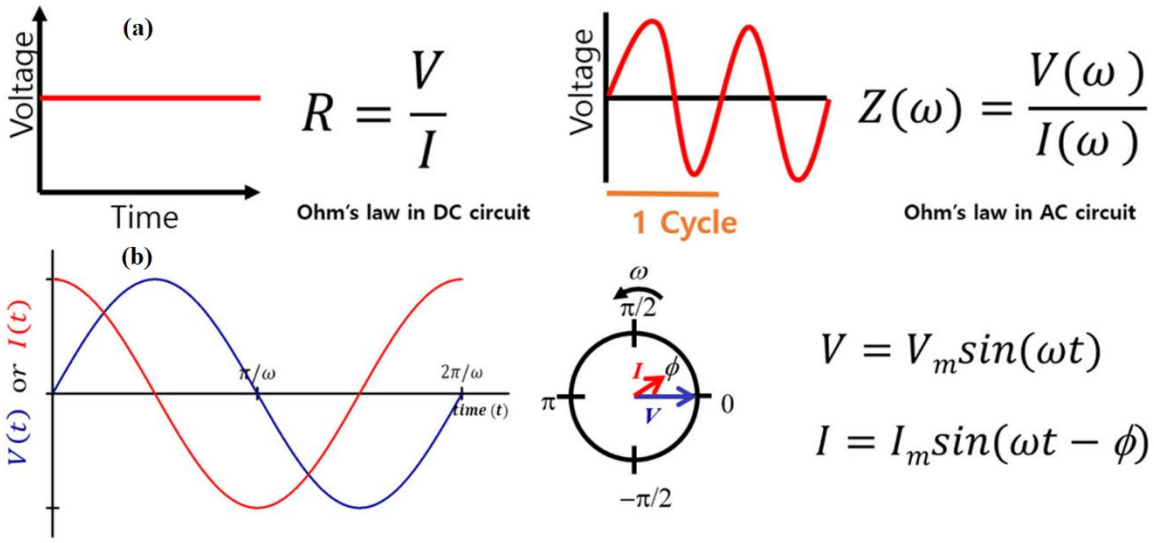

Figure 2.11 *(a) Schematic diagram and equation showing Ohm's law. (b) Relationship between the voltage and current when applying an AC voltage with the angular frequency ω. [25]*

2.7 References

[1] A. J. Moulson and J. M. Herbert, Electro ceramics: Materials, Properties and Application, John Wiley, and Sons Inc., (2003).

[2] R.N.P. Choudhary and S. K. Patri, Dielectric Materials: Introduction, Research and Applications, Nova Publishers, (2009).

[3] A. Malhotra, M. Hosseini, S.H. Zaferani, M. Hall, D. Vashaee, *ACS Appl. Mater. Interfaces* **12**,45(50941).

[4] A. Kumar, S. Dutta, S. Kim, T. Kwon, S.S. Patil, N.K.S. Jeevanandham, I.S. Lee, Chem. Rev. **15**, 122(12748).

[5] Robert E. Dinnebier and Simon J. L. Billinge, Powder Difracction: Theory and Practice, The Royal Society of Chemistry, Cambridge CB4 0WF, UK(2008).

[6] A.A. Bunaciu, E.G. Udristioiu, H.Y. Aboul-Enein, Critical Reviews in Analytical Chemical **45**, 298(2015).

[7] I. Katsuhiko, K. Shintaro, U. Kenichi, O. Akira, R.L. Sanapa, E. Tamio, Advance in Materials Physics and Chemistry **3**, 72(2013).

[8] Vitalij K. Pecharsky and Peter Y. Zavalij, Fundamentals of Powder Diffraction and Structural Characterization of Materials, Springer (2009).

[9] R. A. Young, The Rietveld Method, Oxford University Press (1991).

[10] J. Rodriguez-Carvajal, Physical B **192**, 55 (1993).

[11] Crystallographic tools for Rietveld, profile matching & integrated intensity refinements of X-ray and/or neutron data (2022), FullProf suite software **7.70** (https://www.ill.eu/sites/fullprof/).

[12] J. Johnston, E.N. Taylor, R.J. Gilbert, T.J. Webster, International Journal of Nanomedicine **11**, 45(2016).

[13] John R. Ferraro, Kazuo Nakamoto, and Chris W. Brown, "Introductory Raman Spectroscopy," Second edition, Elsevier (2003).

[14] Ewen Smith, Geoffrey Dent, "Modern Raman Spectroscopy - A Practical Approach," Wiley & Sons (2005).

[15] T. Buchner, T. Kiefer, W. Gaggl, L. Zelaya-Lainez, J. Fussl, Construction and Building Materials **288,** 122909(2021).

[16] A.V. Crewe; M. Isaacson, D. Johnson, Rev Sci Instrum **40**, 241(1969).

[17] H.H. Perkampus, "UV-VIS Spectroscopy and Its Applications," 1st edition, Springer-Verlag (1992).

[18] B.M. Weckhuysen, P. Van Der Voort, G. Cortana, "Spectroscopy of Transition Metal Ions on Surface",1st edition, Leuven University Press (2000).

[19] E. Rosenbaum, L.F. Register, Transactions on Electron Devices **44**, 317(1997).

[20] Available at: http://thisweekinbatteries.blogspot.com/2010/06/in-batteries-221-actually-more-like-12.html. (Accessed: 1st January 2016).

[21] J. Wang, J. Yang, C. Wan, K. Du, J. Xie and N. Xu, Adv. Funct. Mater.**13**, 487(2003).

[22] L. Kong, H.J. Peng, J.Q. Huang, W. Zhu, G. Zhang, Z.W. Zhang, P.Y. Zhai, P. Sun, J. Xie, Q. Zhang, Energy Storage Materials **8**, 153(2017).

[23] X. Huang, Z. Wang, R. Knibbe, B. Luo, S. Abdul Ahad, D. Sun, L. Wang, ACS Energy Technology **10**, 1002(2019).

[24] X. Qiu, Q. Hua, L. Zheng, Z. Dai, RSC Adv. **10,** 5283(2020).

[25] C. Woosung, S. Heon-Cheol, K. Ji Man, C. Jae-Young, Y. Won-Sub, J. Electrochem. Sci. Technol **1**, 11(2020).

CHAPTER 3

Phase transition and energy storage density in lead-free ferroelectric $Ba_{1-x}Sr_xTiO_3$ (x = 0.1, 0.3, and 0.7) capacitors

3.1 Abstract

Structure, phonon, and energy storage density in Sr^{2+}-substituted lead-free ferroelectric $Ba_{1-x}Sr_xTiO_3$ (BST_x) for compositions x = 0.1, 0.3, and 0.7 were investigated using X-ray diffraction, Raman, and ferroelectric polarization measurements as a function of temperature. The samples were tetragonal for x = 0.1 with a large c/a ratio. The tetragonal anisotropy was decreased upon increasing x and transforming to cubic for x = 0.7. The changes in structural and ferroelectric properties were found to be related to the c/a ratios. The temperature-dependent phonon spectroscopy results indicated a decrease in tetragonal-cubic phase transition temperature, Tc, upon increasing x due to a reduction in the lattice anisotropy. The intensity of ~303 cm^{-1} E(TO2) mode decreased gradually with temperature and that finally disappeared around the tetragonal ferroelectric to cubic paraelectric phase at about 100 ℃ and 70 ℃ for x = 0.1 and 0.3, respectively. A gradual reduction in the band gap E_g of BST_x with x was evident from the analysis of UV-Visible absorption spectra. The energy storage density (U_{dis}) of the ferroelectric capacitors for x = 0.7 was ~0.20 J/cm^3 with an energy storage efficiency of ~88% at an applied electric field of 104.6 kV/cm. Nearly room temperature transition temperatures T_C and reasonably fair energy storage density of the BST_x capacitors were found.

3.2 Introduction

Recent research on sustainable energy requires the design and development of new energy storage materials for their applications in energy storage devices such as batteries, supercapacitors, and electrostatic capacitors. Electrostatic capacitors are promising in specific power operating voltage, fast charge-discharge capacity, and resistance, and are of great interest due to their potential applications in pulse power electronics [1,2], weapons [3], and electric vehicles [4,5]. The dielectric capacitors have also aroused great interest due to their fast charge and discharge energy density [6,7]. The dielectric capacitors have ultra-low charge and discharge time with ultra-high energy storage density [8,9]. As a result, in recent years, eco-friendly lead-free dielectric energy storage materials are the subject of research as an alternative to lead-based toxic materials [7]. However, it is difficult to realize a high recoverable energy density of $W_{re} > 2\ J/cm^3$ and energy storage efficiency of $\eta > 80\%$ simultaneously under a relatively low electric field in several lead-free dielectric ceramics [10]. The ferroelectric capacitor stores electrostatic energy and exhibits an electric displacement polarization loop. The polarization loop of the ferroelectric capacitor is established due to the separation and alignment of electric charges by an induced electric field. In general, the energy storage density of a ferroelectric capacitor is calculated from the numerical integration of the close area of the ferroelectric electric polarization (P-E) loop measured at different electric fields [7,9,11]. It is established that the antiferroelectric (AFE) materials are promising as they possess high polarization maximum P_{max}, low remanent polarization P_r, unique polarization versus electric field loop, and a high recoverable polarization that is involved during charging and discharging processes [12,13]. For instance, $(Na_{0.5}Bi_{0.5})TiO_3$-based AFE ceramic

capacitors can store large energy density [14,16]. However, the main drawback with AFE materials lies in their high dissipation energy (which implies a low storage energy efficiency), due to the large hysteresis involved in the polarization versus the electric field loop [17]. Lead-free relaxors, manifested by a slim P-E hysteresis loop (with maximum P_{max} and small P_r), are explored as promising energy storage materials to fabricate electrostatic capacitors with high energy density and high energy storage efficiency. The order-disorder cation in relaxor ferroelectric establishes local and heterogeneous polar states in the nanoscale range known as the polar nanoregions (PNRs). The nucleation and growth of these PNRs are widely considered the reason behind the slim P-E loop.

Raman spectroscopy is a light-scattering local probe sensitive to crystal structure, ferroelectric phase transition, and short-range polar ordering, and is often complemented by the diffraction technique [18]. Raman spectroscopic studies on crystal identify structural phase transition, chemical inhomogeneity, lattice stress, and grain size effects in materials [18,21]. The anomaly in Raman spectra measured as a function of composition and temperature identify ferroelectric phase transition. A ferroelectric phase has a unique set of Raman active phonons governed by spectral selection rules. Hence, when it undergoes a ferroelectric phase transition, other species of phonons associated with the transformed phase become Raman activated [22].

$BaTiO_3$ (BTO) is a well-studied ferroelectric compound stabilized in a tetragonal phase at room temperature [23,24]. However, a large leakage current is realized in BTO due to poor densification of the compound. Improvement in the ferroelectric behavior of BTO has been observed by cationic substitution of different dopants such as Na, Sr, Ca, and N in the parent compound [15,25]. Moreover, the study of energy storage capacitive

behavior of the *A*-site Sr-substituted BTO compound is limited. $Ba_{1-x}Sr_xTiO_3$ (BST_x) is known as a promising ferroelectric material stabilized in the ABO_3-type perovskite phase [19]. The *A*-site of the perovskite occupies by either Ba and Sr cations, as well as the *B*-site by T_i cation, and the compound stabilizes in a distorted tetragonal ferroelectric phase. BST_x with Sr content x higher (lower) than 0.4 are in cubic (tetragonal) phase at room temperature [19]. Eventually, tetragonal ferroelectric BST_x transforms to a paraelectric cubic phase at high temperatures [19]. It exhibited good dielectric behavior with low tangential loss in the high frequency range. The ferroelectric studies of these high-performing materials are paramount from the point of view of energy storage device applications. In recent years, advances in dielectric capacitor technology have attracted significant research interest in developing lead-free eco-friendly nano-electronic materials for energy storage applications. The ferroelectric behaviors in perovskite ferroelectrics are governed by their tetragonal lattice anisotropy (c/a ratio) [26]. Furthermore, nanocrystalline ferroelectrics often show different behavior from bulk. Therefore, the lead-free BSTx ferroelectric materials with different concentrations of barium and strontium composition with a significant variation in their c/a ratios are of great interest to study. As a result, the ferroelectric ordering can be changed; consequently, one can tailor the energy storage capacitive behaviors in BST_x. In this work, we have synthesized $Ba_{1-x}Sr_xTiO_3$ (BST_x) submicron-size ceramics for x = 0.1, 0.3, and 0.7, coined as BST1, BST3, and BST7, respectively, by high-energy ball milling, and the solid-state reaction method and investigated their crystal structure, phonon vibration, ferroelectric polarization, capacitive storage energy density, and leakage current behavior using X-ray diffraction (XRD), Raman spectroscopy, ferroelectric polarization, and I-V curve measurements. The bandgap

energy of these samples has also been examined for their possible photovoltaic applications. The present study is expected to provide better insight into the design and tuning of the physical properties of lead-free BST_x submicron-size ferroelectric with x.

3.3 Experimental and methods

BST_x (x = 0.1, 0.3, and 0.7) samples were prepared by high-energy ball milling and solid-state reaction method. The stoichiometric ratio of starting raw materials $BaCO_3$ (99.997%), $SrCO_3$ (99.998%), and TiO_2 (99.988%) were mixed along with isopropanol using Planetary ball-milling (Pulverisette Fritsch Planetary Mill). The powder of the metal oxides was mixed with a tungsten carbide media at a ball-powder weight ratio of 3:1 at a speed of 600 rpm for ten hours operated in a bi-directional mode with a rotational frequency of 45 Hz. The ball milling was suspended for 20 min after every 1 h of milling to cool down the milling system. The mixed slurries were dried on a hot plate at 100 °C overnight and pulverized thoroughly using a motor and pestle. The powder was screened using a mesh of 150 μm size to obtain a fine powder of almost uniform particle size. The powder was pre-calcined at 850 °C/4 h, followed by thorough pulverization and calcined at 1150 °C/2 h at a ramp rate of 5 °C/min. The calcined powder was mixed with 5 wt. % polyvinyl alcohol (PVA) solution and pressed into pellets with a diameter of 10 mm and thickness of 1.5 mm by applying a uniaxial hydraulic press of 8 Ton for 5 min. These pellets were sintered at a high temperature of 1250 °C for 2 h at a slow ramp rate of 2 °C/min following a similar report [27]. The geometrical bulk density of the sintered pellets was estimated using the weight and dimension of the BST1, BST3, and BST7 samples, which are 5.382 gm/cm^3, 5.241 gm/cm^3 and 5.071 gm/cm^3, respectively. The relative density of these ceramics showed ~91% (BST1), ~92% (BST3), and ~93% (BST7). At other higher

sintering temperatures, the densities of the samples may improve. The surface morphology of the crack-sintered pellets was studied using scanning electron microscopy (SEM) (model: JEOL/MP) equipped with a backscattered electron detector operating at an accelerating voltage of 20 kV and 3300× magnifications. SEM-based energy dispersive X-ray spectra (EDS) (model: JSM-IT500HR-JEOL) were measured from the crack surface of the sintered pellets to infer their chemical compositions. The X-ray diffraction (XRD) measurements were carried out using a Rigaku SmartLab X-ray diffractometer equipped with CuK_{α} radiation (λ = 1.5418 Å) operated in a Bragg-Brentano (θ–2θ) geometry at 40 kV and 44 mA. The crystal structure and phase purity of the compounds were checked in a slow scan mode using a 2θ step size of 0.05°. The analyses of the XRD patterns were carried out using FullProf suite software 7.70 (Version April 2022). Raman spectroscopy studies were carried out employing a HORIBA Jobin Yvon *micro*-Raman spectrometer (model: T64000) equipped with a 50× long working distance objective lens in a back-scattering geometry (2θ = 180°) using a 514.5 nm line of an Ar^{+} ion laser (Coherent, Innova 70-C). Raman spectra with improved signal-to-noise ratio were measured by optimizing the Laser power and acquisition time. The scattering light from the sample was dispersed by a triple monochromator and detected by a liquid N_2-cooled charge-coupled device detector. The spectral resolution was about 1 cm^{-1} for 1800 lines/mm grating. Raman spectra as a function of temperature were measured from −40 °C to 150 °C in a close temperature interval of 10–20 °C using a Linkam heating/cooling stage with temperature stability of ±1 K. The ferroelectric hysteresis loops were measured on the thin pellet of thickness 0.3 mm at an applied frequency of 50 Hz using an automatic P-E hysteresis loop tracer system (RT6000 HVS Radiant Technologies Inc., San Diego, CA, USA) that utilizes

a modified Sawyer Tower test circuit to reduce noise by using a virtual ground. The current-voltage (I-V curves) curves were measured at room temperature using a Keithley electrometer (model #2401) with the top silver-painted electrode DC biased and the bottom silver-painted electrode grounded. UV-Visible absorbance spectra were measured from the polished surface of the pellets in the energy range from 0.3 to 1.9 eV employing a Fourier transform UV-Visible-infrared spectrometer (Agilent Technologies, Cary 100-bio, Santa Clara, CA, USA). The band gaps of the compounds were obtained from the analysis of UV-Visible absorbance spectra.

3.4 Results and discussion

The phase purity and structural parameters of BST_x (x = 0.1, 0.3, and 0.7) ceramics were obtained from Rietveld analysis of the high-resolution powder XRD patterns measured in the 2θ range from 10 to 100° at room temperature (Figure 3.1 a). To carry out the Rietveld analysis, the starting structural parameters were considered from JCPDF No # 34-0411 (tetragonal structure, space group P4mm, and the number of formula units per unit cell Z = 1). Linear interpolation of manually selected background points was considered to have a smooth background profile modeled by using the Chebyshev polynomial with six coefficients. The X-ray reflection peaks were modeled using pseudo-Voigt function. Subsequently, the scale factor, half-width parameters of peak profile, unit cell parameters, atomic position coordinates, and isotropic thermal parameters of Ba, Sr, Ti, and O atoms were successfully refined. The Rietveld refinement plot of BST_x is shown in Figure 3.1 a. The refined unit cell parameters of $Ba_{0.9}Sr_{0.1}TiO_3$ are a = 3.9871(1) Å, c = 4.0166(1) Å , and V = 63.851(1) $Å^3$, which are in close agreement with an earlier report [28]. The residuals of refinement are Rp = 2.57%, R_{wp} = 3.99% and χ^2 = 1.55. Similarly,

the analyses were carried out for XRD patterns of x = 0.3 and 0.7; and the obtained refined unit cell parameters and the residual of their refinements are listed in table 3.1.

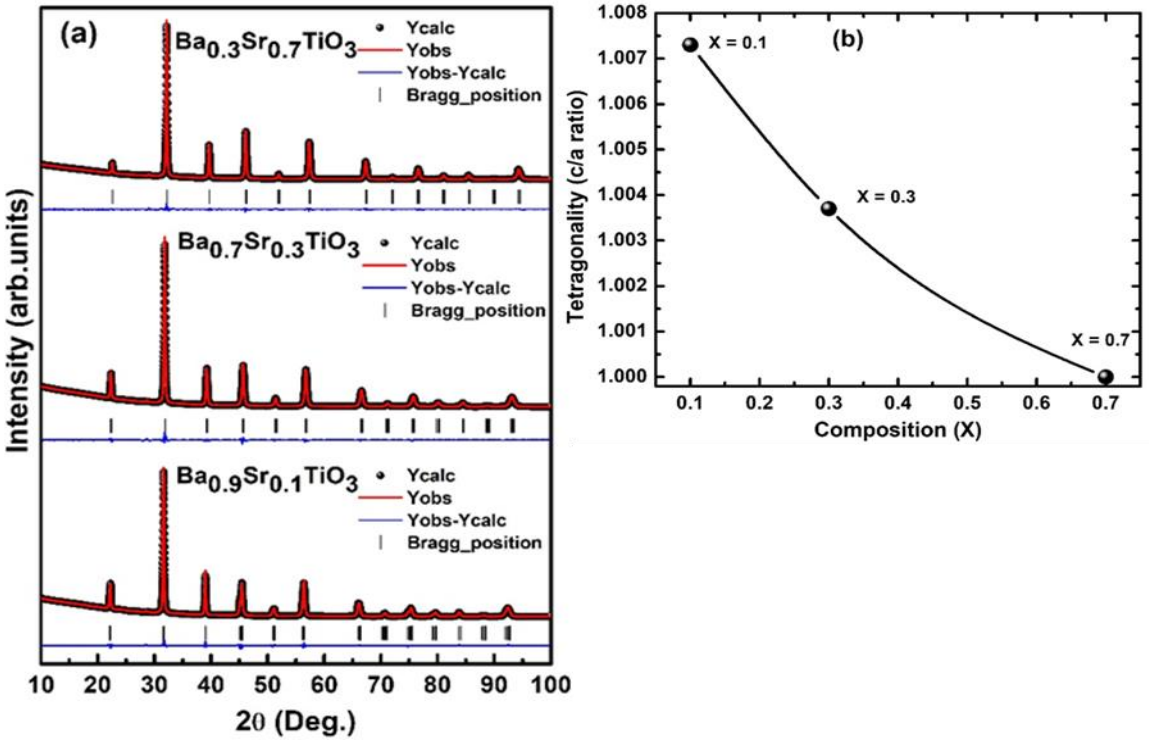

Figure 3.1 *(a) Rietveld refinement of XRD patterns of BST_x for x = 0.1, 0.3, and 0.7. Lower vertical lines (black color) show the Bragg's positions of tetragonal phase for x = 0.1 and 0.3, and cubic phase for x = 0.7 and (b) Variation of tetragonality (c/a ratio) with Sr-content x.*

The calculated tick patterns are shown at the bottom of figure 3.1. correspond to the tetragonal phase of BST1 and BST3 and cubic phase for BST7. As there are no unindexed lines in the XRD patterns, the single-phase formation of these compounds is evident. All the X-ray diffraction peaks were shifted to higher 2θ angles with increasing Sr contents, suggesting a gradual decrease in the lattice parameters. The doublets at 2θ ~45, 67, and 75 degrees for x = 0.1 and 0.3 turned out to be single reflection peaks for x = 0.7, which is consistent with an earlier report. [29] The intensity of several diffraction peaks for x = 0.7 at 2θ ~45, 67, 71, 83, and 92 degrees was found to decrease compared to the other two

lower Sr content compounds. The unit cell volume reduces from 63.851 $Å^3$ for x = 0.1 to 60.963 $Å^3$ for x = 0.7. The change in the volume of the crystal unit cell indicates a change in the density of the synthesized structures; consequently, that affects the changes in the ferroelectric properties as revealed later in the ferroelectric studies. The lattice anisotropy of the crystal was calculated from the ratio of c- and a- lattice parameters of the tetragonal phase. The anisotropic c/a ratios were 1.0073, and 1.0037 for x = 0.1, and 0.3respectively. The lattice anisotropy became smaller with increasing Sr-content. For x = 0.7, the c/a ratio became unity (Figure 3.1b). A large tetragonality (c/a = 1.007) was observed for x = 0.1, which decreases to 1.004 for x = 0.3. For x = 0.7, the XRD pattern fits cubic structure with space group Pm3m. The tetragonal distortion (c/a ratio) disappeared for x = 0.7 and a cubic phase with lattice parameter a = 3.9357(1) Å emerged. Therefore, the structural change from tetragonal to cubic phase occurred due to the homovalent substitution of Bi^{2+} (ionic radius 1.61 Å) by Sr^{2+} (ionic radius 1.44 Å) cation [30].

Table 3.1 *Structural parameters of BST_x (x = 0.1, 0.3 and 0.7) obtained from Rietveld analysis of XRD patterns.*

x	a (Å)	c (Å)	V ($Å^3$)	c/a	R_p	R_{wp}	χ^2
0.1	3.9871(1)	4.0166(1)	63.851(1)	1.0073	2.57	3.99	1.55
0.3	3.9673(1)	3.9822(1)	62.677(1)	1.0037	2.37	3.6	1.51
0.7	3.9357(1)		60.963(2)	-	1.9	2.80	1.44

SEM micrographs measured from the fractured surface of the sintered BST_x pellets are shown in Figure 3.2, indicating a nearly uniform distribution of grains throughout the surface. A noticeable difference in grain sizes with Sr content was observed. The average grain sizes of these compounds were 80–300 nm for BST1, 100–300 nm for BST3 and 50–100 nm for BST7. It is worth noting that in our experiment, the long-time high-energy ball-

milling, high rpm speed, and the slow heating rate of the sintering (2°C/min) was favorable for the growth of submicron-size grains, resulting in a reasonably densified pellet. The SEM micrographs showed the morphology of the submicron-size grains in ferroelectric BST_x. It revealed that the pellets were crack free with little porosity. The porosity decreased with increasing x, which was consistent with the observed geometrical bulk densities of the samples. Interestingly, upon increasing Sr contents, the grain size of BST_x decreased due to the smaller radius of Sr^{2+} ions; consequently, that modified the sample surface due to the insertion of Sr^{2+} ions into the $BaTiO_3$ structure.

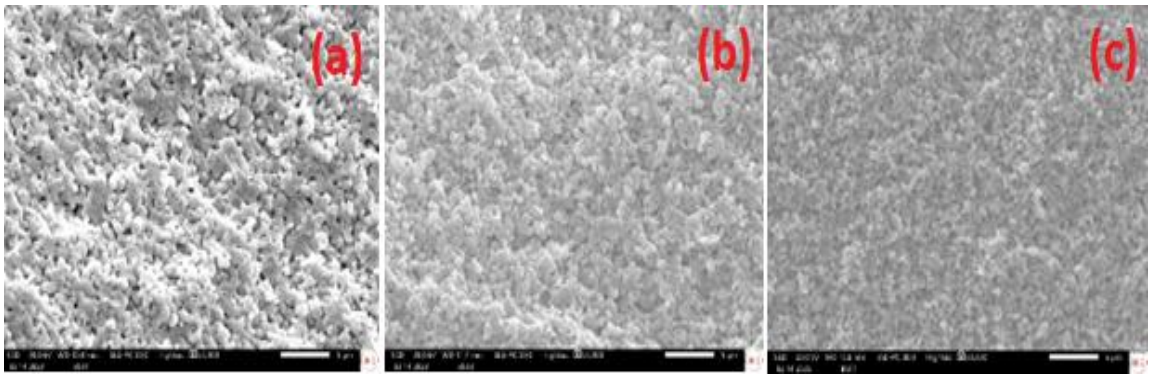

Figure 3.2. *Scanning electron micrographs from a fracture surface of BST_x samples (a) $Ba_{0.9}Sr_{0.1}TiO_3$ (b) $Ba_{0.7}Sr_{0.3}TiO_3$ and (**c**) $Ba_{0.3}Sr_{0.7}TiO_3$.*

The EDS spectra were measured from the fracture surface of the sintered pellets to study the chemical compositions (Figure 3.3). It suggested the presence of Ba, Sr, Ti, and O constituent chemical elements. The estimated compositions [29] (final stoichiometry) were found to agree with those of the theoretically expected compositions (starting compositions). The experimental compositions of the sintered pellets BST1, BST3, and BST7 are $Ba_{0.86}Sr_{0.11}Ti_{1.02}O_{3.21}$, $Ba_{0.68}Sr_{0.34}Ti_{1.10}O_{2.55}$, and $Ba_{0.23}Sr_{0.78}Ti_{0.84}O_{3.3}$, respectively.

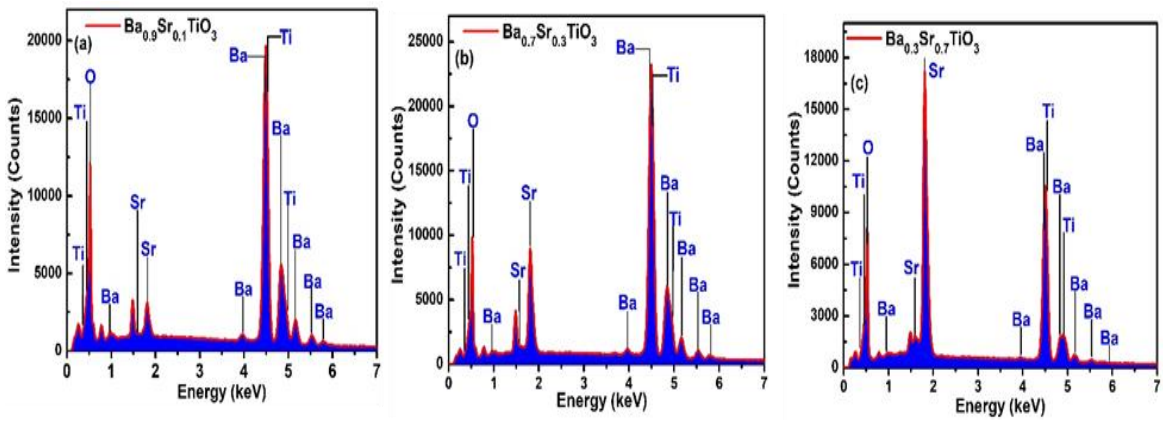

Figure 3.3 *EDS spectra from a fracture surface of BST_x samples (a) $Ba_{0.9}Sr_{0.1}TiO_3$ (b) $Ba_{0.7}Sr_{0.3}TiO_3$ and (c) $Ba_{0.3}Sr_{0.7}TiO_3$.*

Raman spectra of BST_x samples were measured at room temperature in the frequency range of 30-1000 cm^{-1} (Figure 3.4). The mode frequencies of Raman bands observed for x = 0.1 were located around 170 cm^{-1} A1(TO1), 251 cm^{-1} A1(TO2), 303 cm^{-1} E(TO2), 514 cm^{-1} A1(TO3) and 720 cm^{-1} A1(LO3) in agreement with those found in earlier reports [18–22]. Raman active A1 and E phonons are expected in the tetragonal phase of BST_x. These modes were split into longitudinal (LO) and transversal (TO) modes due to the effect of long-range electrostatic force associated with lattice ionicity [19]. For x = 0.3, the Raman bands were broadened and reduced their intensities. The Raman bands at around 303 cm^{-1} and 720 cm^{-1} are specified for the tetragonal phase [18,31], confirming the tetragonal phase of BST1 and BST3. The theoretically expected optical phonons in the Pm3m cubic phase are F1u and F2u, where the F1u mode is only infrared active, and the F2u mode is silent [32]. Thus, no Raman active modes are expected for x = 0.7. Only broad Raman bands centered around 233, 368, and 620 cm^{-1} were observed for this compound (Figure 3.4). These bands in the cubic phase are expected due to a substitutional disorder at cation sites and essentially have a significant contribution from the phonon density of states [32]. The

303 cm^{-1} E(TO2) band is well-known as the structurally sensitive band to the tetragonal-cubic phase transition [17]. The intensity of this Raman band was examined, and found that the intensity decreased with x. For x = 0.7, the E(TO2) band intensity decreased rapidly, and was not discernable as the tetragonal distortion (c/a-1) approached zero and confirmed the cubic phase of the compound. The observation of broad Raman peaks in the cubic phase suggests the relaxor ferroelectric behavior of the perovskite compound [32].

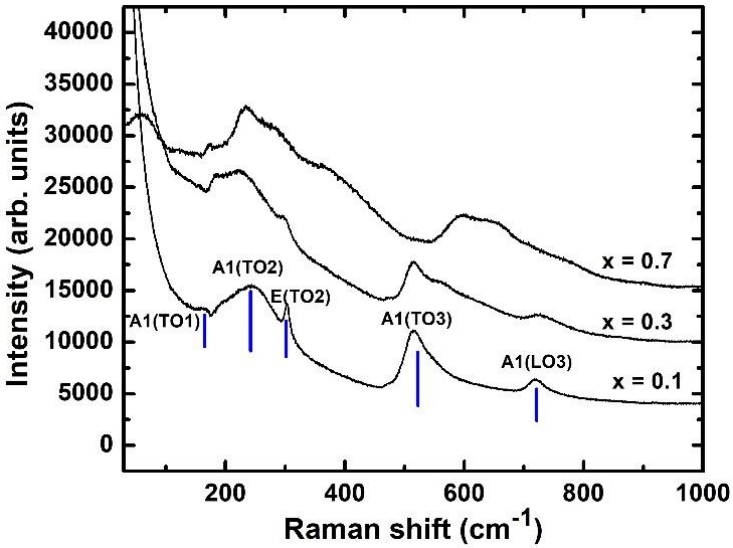

Figure 3.4 *Room temperature Raman spectra of BST_x for different Sr-contents. The phonon modes are labeled with vertical lines.*

Raman spectra were measured at several temperatures in the heating cycle to identify the phase transition of BST_x (x = 0.1 and 0.3) (Figure 3.5). Upon increasing temperature, the phonon frequency and linewidth broaden due to anharmonicity involved in the interatomic potential field of the crystal lattice [33]. For x = 0.1, at the high temperature of 150 °C, only two broad Raman peaks centered around 247 and 552 cm^{-1} were observed. For x = 0.3, these two Raman bands were noticed at high temperature of 100 °C. The spectral intensity decreased, and band linewidths broadened at elevated temperatures due to a decrease in phonon lifetime resulting from multiple phonons scattering processes [33].

The Raman intensity of the structural sensitive 303 cm^{-1} E(TO2) Raman band decreased gradually with increasing temperatures and disappeared at around 100 °C and 40 °C for x = 0.1 and 0.3, respectively. In addition, the 720 cm^{-1} A1(LO3) Raman band intensity of the tetragonal phase decreased and could not be followed up beyond 100 °C and 40 °C for x = 0.1 and 0.3, respectively. This suggested that the tetragonal to cubic phase transition occurred at 100 °C and 40 °C for BST1 and BST3, respectively, in agreement with an earlier report [18].

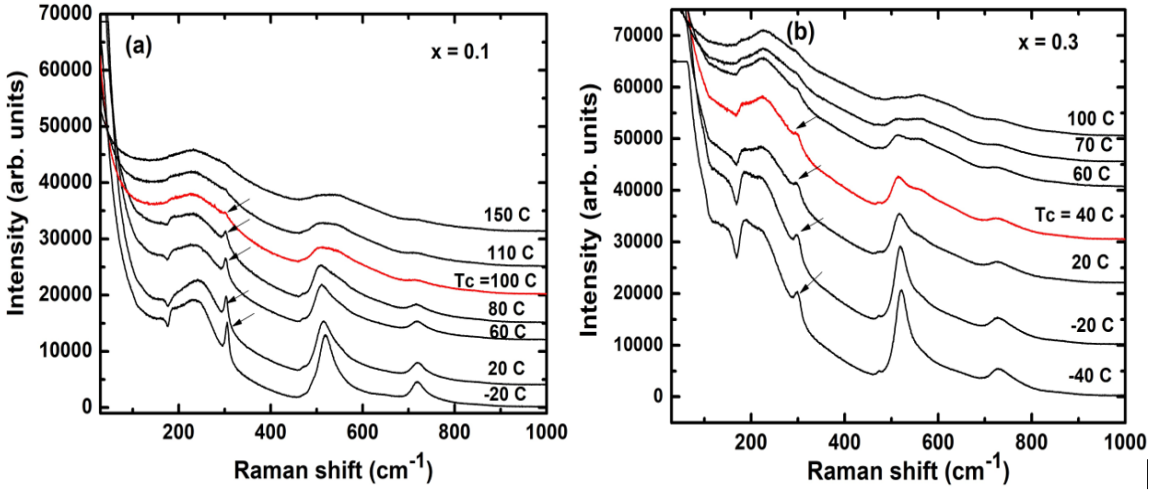

Figure 3.5 *Temperature dependent Raman spectra of BST_x for (a) x = 0.1 and (b) x = 0.3. The evolution of E(TO2) band intensity with temperature is shown by arrow marks. For x =0.1 and 0.3, the tetragonal to cubic phase transition temperature Tc is observed at about 100 °C and 40 °C, respectively.*

The transition temperature was found to decrease with increasing Sr-content x. This was expected due to the reduction in the tetragonal lattice distortion of BST_x with increasing Sr- substitution x. Temperature-dependent Raman spectroscopic study for x = 0.7 was not carried out as the compound was in the cubic phase at room temperature (as discussed earlier).

BST_x has a direct band gap involving an electronic transition between the top of the valence band and the bottom of the conduction band [34]. The optical band gap (E_g) for BST_x was estimated from the analysis of UV-Visible absorbance spectra recorded from the sintered pellets in the wavelength range of 300 to 800 nm. The famous Tauc equation $(\alpha h\nu)^n = A(h\nu - E_g)$, where A is the proportionality constant, n = 2 for the direct band gap material, and n = 1/2 for indirect band gap material, is useful to estimate the bandgap of the compound using the reflectance data [34]. It can be mentioned that the Kubelka and Munk (K-M) function is defined by $F(R) = (1-R)^2/R$, where R is the reflectance obtained from the polished surface of the samples. This function F(R) is a mathematical function of reflectance R and is directly proportional to the optical absorption coefficient α of the materials [34,35]. Therefore, F(R) can be substituted in place of α in the Tauc equation to estimate the band gap E_g of the materials. Upon substitution, the modified Tauc equation turns out to be $[F(R)\ h\nu]^2 = A(h\nu - E_g)$ for direct band gap material. From the analysis of $[F(R)h\nu]^2$ versus hν-plotted curves, the direct band gaps in BSTx were estimated, where h is the Planck's constant and ν is the incident photon frequency (Figure 3.6 a–c). The tangent of the linear part of the curve touching the horizontal axis originating from the center provides the band gap E_g of the compound. The Eg values obtained from the analysis are 1.73 eV for BST1, 1.70 eV for BST3, and 1.63 eV for BST7, similar to those band gaps reported earlier [36]. Therefore, a gradual reduction in the band gap E_g of BST_x with Sr-substitution x is evident. The reduction in band gap E_g of BST_x compared to pristine BTO (3.10 eV) [37] was found to be around ~1.67 eV (Figure 3.6 d). The compounds have a narrow band gap in the visible light region and can have photovoltaic applications [38].

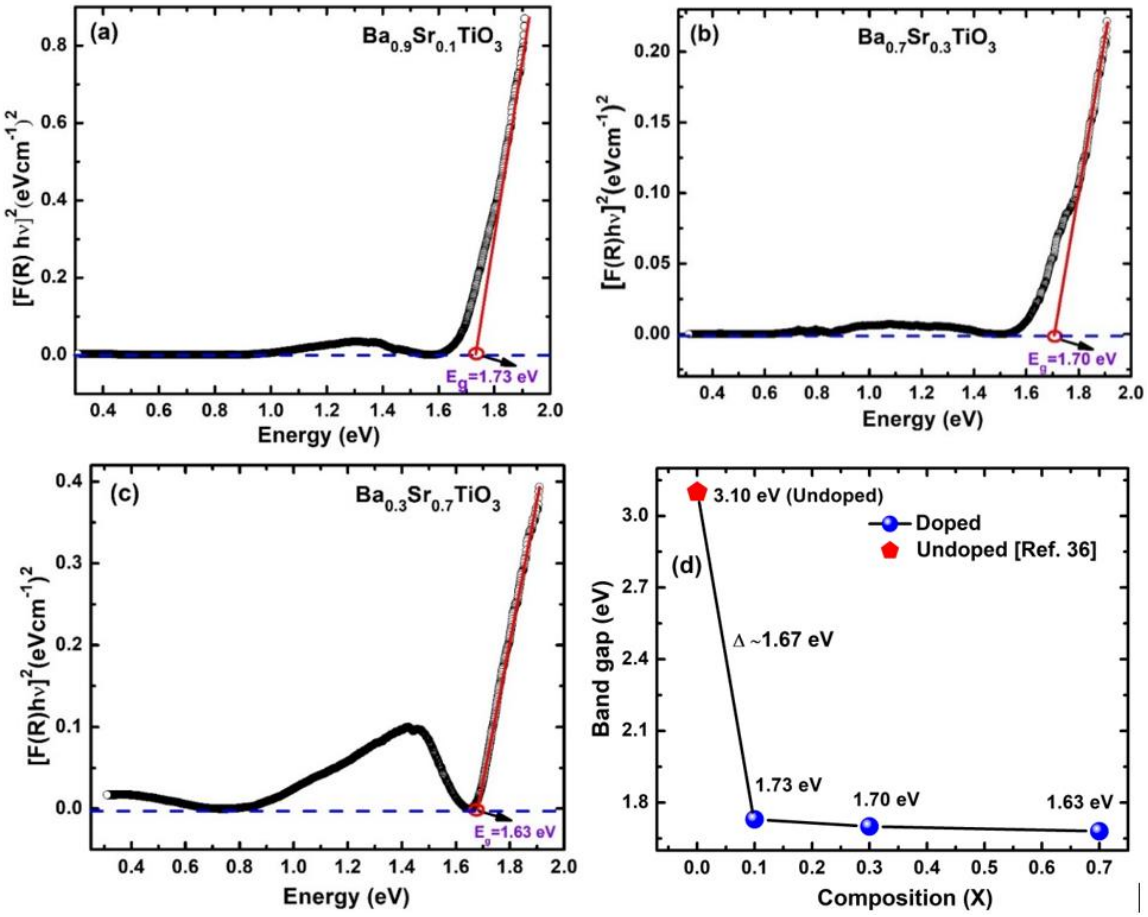

Figure 3.6. *Optical band gap E_g of BST_x using UV-Visible absorbance spectra using modified Tauc plot: $[F(R)hv]^2$ versus hv (a) x = 0.1, (b) x = 0.3 (c) x = 0.7 and (d) BST_x band gap reduces by about ~1.67 eV as compared to the pristine BTO is also shown.*

3.4.1 Current-voltage (I-V) behaviors

The leakage current conduction behavior of the BST_x capacitor was measured with a voltage step of 0.1 V (Figure 3.7 a–c). Below 30 V, the electric current increased linearly, with applied voltages indicating an Ohmic conduction behavior in BST_x. On the other hand, above 30 V, an exponential increment of current with voltage was observed, attributed to the Schottky or Poole-Frankel emission type conduction processes due to oxygen vacancies-related conductivity [39]. The leakage currents in these sintered ceramic

capacitors were of the order of 10^{-10} to 10^{-11} A, indicating that these compounds were well compacted and densified.

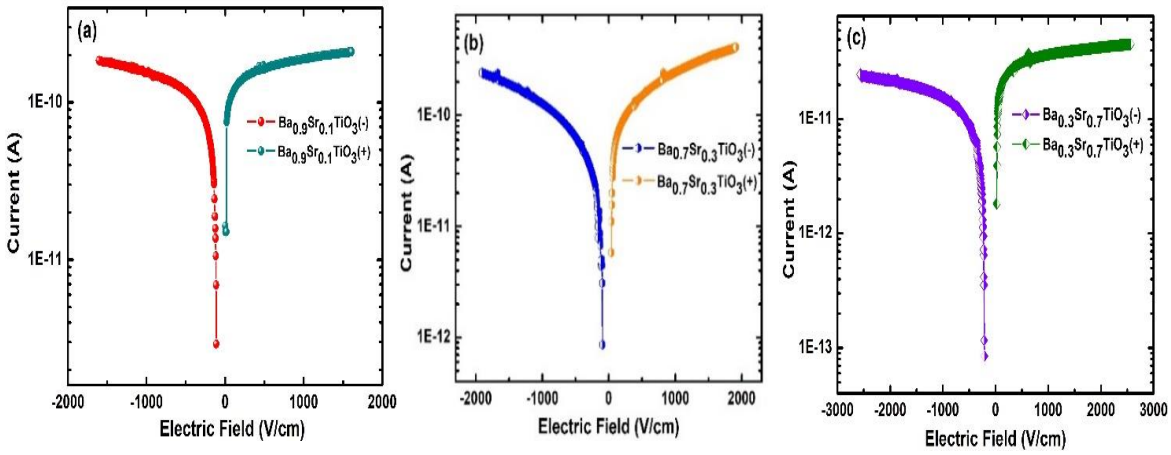

Figure 3.7. *Leakage current behavior with the applied electric field for the BST_x capacitors (a) x=0.1, (b) x=0.3, (c) x=0.7.*

3.4.2 Ferroelectricity, and energy storage density calculations

The P-E hysteresis loops of BST_x capacitors measured at various applied electric fields at room temperature are depicted in Figure 3.8. Upon increasing the applied electric field, the polarization maximum P_{max} and remanent polarization P_r increased, and all the samples exhibited well-defined ferroelectric hysteresis loops (Figure 3.8). The maximum remanent polarization P_r and coercive field E_c of the ferroelectric loops of these compounds is listed in Table 2. The P_r values were large [40] and comparable with those reported in BST_x [41,42]. The high value of P_r of 5.96 μC/cm^2 in the BST1 system was manifested due to long-range cooperative ferroelectric phenomena, indicating the ferroelectric nature of the compound. However, the P_r and Ec values decreased upon increasing strontium content in BST_x. This is because the ferroelectric ordering is progressively disturbed due to an increase in the degree of substitutional disorder (broken translational symmetry) with increasing x. In the BST7 system, the ferroelectric loop appeared as a slim loop (Figure 3.8

c) with a small P_r value of 0.125 μC/cm^2 and a low E_c value of 2.76 kV/cm, characteristic of a relaxor ferroelectric system. Hence, the BST1 and BST3 exhibited normal ferroelectric behavior, and the BST7 sample exhibited a cubic relaxor ferroelectric behavior. One can see that the slope of the major axis of the hysteresis loops of the BST_x (Figure 3.8), which is proportional to the dielectric constant, is quite large, suggesting that the dielectric response of the samples is good.

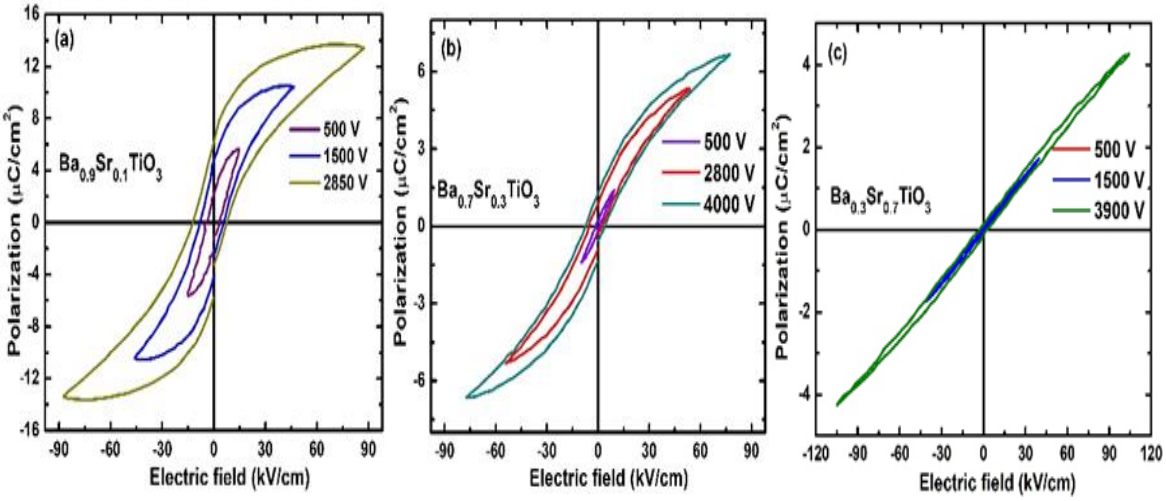

Figure 3.8 *The P-E hysteresis loops of BST_x capacitors measured at room temperature (a) x = 0.1 (b) x = 0.3, and (**c**) x = 0.7.*

Table 3.2 *The remanent polarization P_r and coercive field E_c of BST_x (x = 0.1, 0.3 and 0.7) ferroelectric capacitors.*

BST_x Sample	P_r (μC/cm^2)	E_c (kV/cm)	Ferroelectricity
BST1	5.964	7.63	ferroelectric
BST3	1.279	4.0	ferroelectric
BST7	0.125	2.76	relaxor-ferroelectric

The dielectric breakdown strength of BST1, BST3, and BST7 capacitors was found to be 86.80 kV/cm, 76.66 kV/cm, and 104.65 kV/cm, respectively. A reasonably large breakdown voltage achieved in these capacitors could be attributed to the low porosity density, microcracks-free, phase purity, and submicron grain size of the samples [40,43–

45] corroborated by the high relative densities and low leakage current of these compounds. A reasonably large breakdown electric field of a ferroelectric capacitor is a crucial factor in achieving high-energy storage density.

A high-energy storage density and a high-energy storage efficiency (η) of the ferroelectric capacitors are crucial for device application. During the electric field action period, the electric field varies from zero to maximum E_{max}, resulting in an increment of the ferroelectric polarization from zero to the polarization maximum P_{max}. In this process, the electric energy stored in the ferroelectric capacitor in the forward cycle of the electric field is known as the charge energy storage density U_{st}. Upon decrease in the electric field from maximum E_{max} to zero, the recoverable energy storage density releases from the capacitor known as the discharge energy density U_{dis}. However, the energy density stored between the charge and discharge process is unrecovered due to the hysteresis loss, called loss energy density U_{loss}.

The energy storage behavior of ferroelectric capacitors is studied from the electric field dependence of energy-storage density estimated from P-E hysteresis loops using the formula [7,9].

$$\text{energy storage density } (U_{st}) = \int_0^{P_{max}} EdP \quad (1)$$

$$\text{recoverable energy storage density } (U_{dis}) = \int_{P_r}^{P_{max}} EdP \quad (2)$$

$$\text{energy storage efficiency } (\eta) = \frac{U_{dis}}{Ust} \times 100\% \quad (3)$$

where P_{max}, P_r and E denote the maximum field-induced polarization, remnant polarization, and applied electric field, respectively. Therefore, the energy storage density in the

capacitor is $U_{st} = U_{dis} + U_{loss}$, which can be calculated for the applied electric field from 0 to E_{max}. For clarity, a schematic illustration of the charging, discharging, and loss energy storage density of a ferroelectric capacitor at a maximum electric field of E_{max} is shown in Figure 3.9.

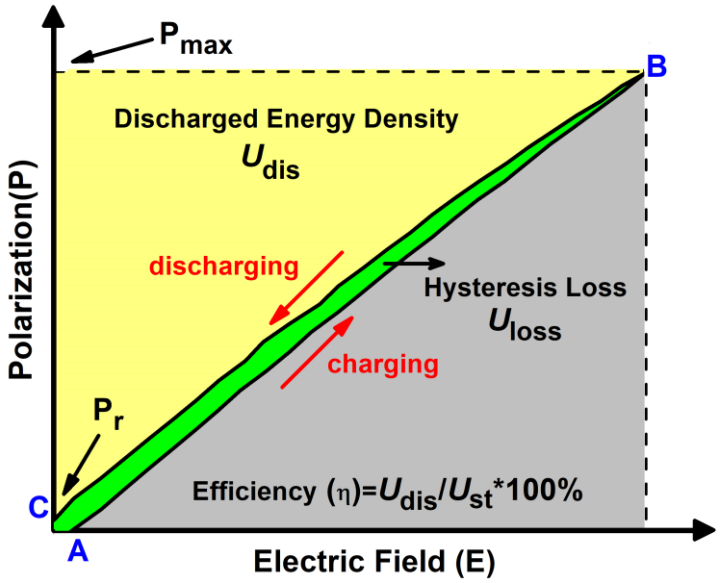

Figure 3.9 *The Schematic sketch illustrates the charging, discharging and hysteresis loss of energy storage density at an electric field of* E_{max}.

The unipolar P-E loops of the BST_x capacitors were measured at various applied electric field at room temperature (Figure 3.10). These loops were analyzed to estimate the U_{dis} and η. A comparison of the reported energy storage density and efficiency for BST_x-based capacitors and our estimated values are listed in Table 3.3. The U_{dis} and η were found to be less in BST1. Interestingly, these values were progressively increasing with increasing Sr substitution. In these submicron-size ceramics, an increase in the insulating behavior of nanograin boundaries with Sr content is expected due to an increase in the grain boundary density due to a reduction in the grain sizes with x. It can be considered as a possible reason for the improved energy storage density with Sr content. In BST7 relaxor

ferroelectric, at applied field of 104 kV/cm and frequency 50 Hz, a high U_{dis} of 0.20 J/cm^3 and large η of ~88% was obtained. In microwaved sintered $(Ba_{0.4}Sr_{0.6})TiO_3$ ceramics, prepared by the co-precipitation method, the U_{dis} was reported to be between 0.77 to 1.15 J/cm^3 with energy efficiencies from 60% to 82% [46]. Jin et al. obtained an energy storage density of 1.081 J/cm^3 with an energy efficiency of about 74% in $Ba_{0.4}Sr_{0.6}TiO_3$ sintered in an O_2 environment [47]. Hwang et al. reported an improved energy storage density of 1.5 J/cm^3 at an applied field of 300 kV/cm in $Ba_{0.6}Sr_{0.4}TiO_3$-MgO ceramics [48]. Wang et al. synthesized $Ba_{0.4}Sr_{0.6}TiO_3$ nanoceramics of about 200 nm grain sizes using the chemical solution precipitation method and reported the energy storage density of 0.33 J/cm^3[49]. Theoretical simulation on $Ba_{0.5}Sr_{0.5}TiO_3$ ceramic predicted the energy density of around 4 J/cm^3 at an applied field of 600 kV/cm [50]. In nanocrystalline $Ba_{0.4}Sr_{0.6}TiO_3$ ceramics of grain size about 0.5 μm, the energy storage density of 1.28 J/cm^3 was observed [51]. A BST-based relaxor ferroelectric of $Ba_{0.65}Sr_{0.35}TiO_3$-$Bi(Mg_{2/3}Nb_{1/3})O_3$ reported an energy storage density of 3.34 J/cm^3 and an energy storage efficiency of 86% [52].

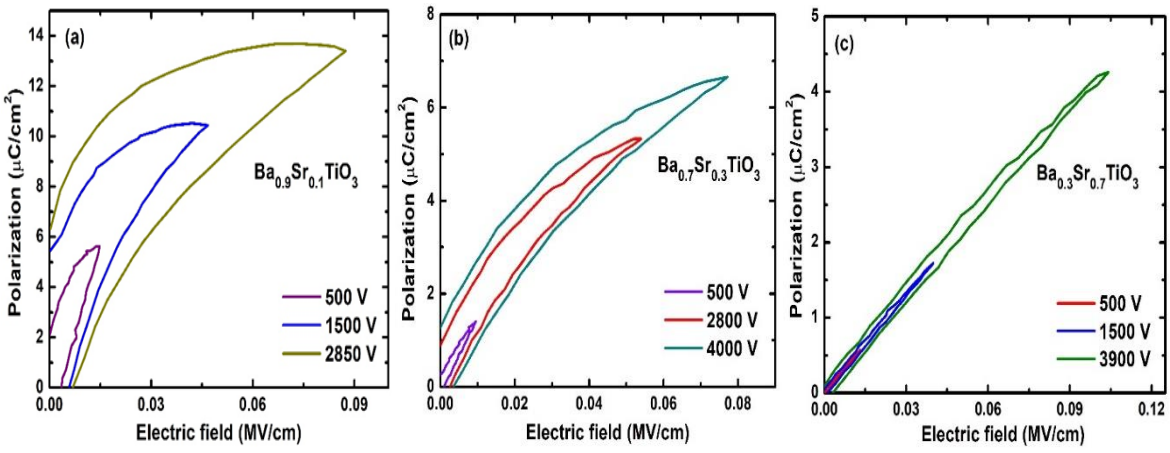

Figure 3.10 *Unipolar Polarization-Electric field loops of BST_x capacitors (a) x = 0.1, (b) x = 0.3, and (**c**) x = 0.7, measured at various applied fields.*

Table 3.3 High energy storage density and energy storage efficiency of BST_x-based capacitors.

Material Composition	U_{dis} (J/cm^3)	η (%)	Electric Field	Worked by
$Ba_{0.4}Sr_{0.6}TiO_3$	1.15	82	180 kV/cm	Son et al. [46]
$Ba_{0.4}Sr_{0.6}TiO_3$-MgO	1.5	-	300 kV/cm	Huang et al. [48]
$Ba_{0.4}Sr_{0.6}TiO_3$	0.33	-	514.2 kV/cm	Wang et al. [49]
$Ba_{0.3}Sr_{0.8}TiO_3$	8	-	600 kV/cm	Fletcher et al. [50]
$Ba_{0.4}Sr_{0.6}TiO_3$	1.28	-	243 kV/cm	Song et al. [51]
$0.9Ba_{0.65}Sr_{0.35}TiO_3$-$0.1Bi(Mg_{2/3}Nb_{1/3})O_3$	3.34	85.7	400 kV/cm	Dai et al. [52]
$Ba_{0.9}Sr_{0.1}TiO_3$	0.11	20	86.79 kV/cm	Present work
$Ba_{0.7}Sr_{0.3}TiO_3$	0.14	62	76.66 kV/cm	Present work
$Ba_{0.3}Sr_{0.7}TiO_3$	0.20	88	104.65 kV/cm	Present work

3.5 Conclusions

Polycrystalline BST_x (x = 0.1, 0.3, and 0.7) samples were prepared using a high-energy ball milling and the solid-state reaction method. Rietveld analysis of XRD data suggests the single-phase formation of the compounds. BST1 and BST3 have a tetragonal phase, and BST7 has a cubic phase. The tetragonal anisotropy (c/a ratio) reduces with increasing Sr-substitution and approaches unity for x = 0.7. The SEM results of BST_x suggest that the nanograin size and porosity decrease with increasing Sr-content x. These compounds have a narrowband gap in the visible light region. Upon increasing Sr-content x, a gradual reduction in the band gap of BST_x was observed. Ferroelectric polarization studies suggested a normal ferroelectric behavior for BST1 and BST3, while relaxor ferroelectric behavior for x = 0.7 capacitors. A recoverable energy storage density U_{dis} of ~0.2 J/cm^3 and an energy storage efficiency η of ~88% were obtained for BST7 capacitors. The present results on ferroelectric BST_x capacitors may be useful in several energy storage applications. BST_x thin films were grown in our lab recently from the target of these materials in RF sputtering technique. We are studying the structural, ferroelectric ordering and energy storage density of the BST_x thin films.

3.6 References

[1] B. Chu, X. Zhou, K. Ren, B. Neese, M. Lin, Q. Wang, F. Bauer, Q.M.A Zhang, *Science* **313**, 334(2006).

[2] M. Zhou, R. Liang, Z. Zhou, X. Dong, *J. Mater. Chem.* C **6**, 8528(2018).

[3] Z. Yao, Z. Song, H. Hao, Z. Yu, M. Cao, S. Zhang, M.T. Lanagan, H. Liu, Adv. Mater. **29**, 1601727(2017).

[4] X. Hao, J. Adv. Dielectr. **3**, 1330001(2013).

[5] Y. Fan, Z. Zhou, Y. Chen, W. Huang, X.A. Dong, J. Mater. Chem. C **50**, 50(2022).

[6] F. Han, G. Meng, F. Zhou, L. Song, X. Li, X. Hu, X. Zhu, B. Wu, B. Wei, Sci. Adv. **1**, 3(2015).

[7] N. Liu, R. Liang, Z. Zhou, X. Dong, J. Mater. Chem. C **6**, 10211(2018).

[8] Y. Wu, Y. Fan, N. Liu, P. Peng, M. Zhou, S. Yan, F. Cao, X. Dong, G. Wang, J. Mater. Chem. C 7, 6222(2019).

[9] J. Wei, T. Yang, H. Wang, J. Eur. Ceram. Soc. **39**, 624(2019).

[10] T. Shao, H. Du, H. Ma, S. Qu, J. Wang, J. Wang, X. Wei, Z. Xu, J. Mater. Chem. A **5**, 554(2017).

[11] H. Yang, F. Yan, Y. Lin, T. Wang, F. Wang, W. Yilin, L. Guo, W. Tai, H. Wei, J. Eur. Ceram. Soc. **37**, 3303(2017).

[12] J. Li, F. Li, Z. Xu, Adv. Mater.**30**, 1802155(2018).

[13] B. Ma, Z. Hu, R.E. Koritala, T.H. Lee, S.E. Dorris, J. Mater. Sci.: Mater. Electron. **15**, 3025(2015).

[14] T. Ozaki, S. Kitagawa, S. Nishihara, Y. Hosokoshi, M. Suzuki, Y. Noguchi, M. Miyayama, S. Mori, *Ferroelectrics* **385**,155(2009).

[15] L. Zhang, X. Hao, *J. Alloys Compd.* **586**, 674(2014).

[16] A. Mishra, B. Majumdar, R. Ranjan, J. Eur. Ceram. Soc. **37**, 2384(2017).

[17] A. Chauhan, S. Patel, R. Vaish, C.R. Bowen, Materials **8**, 8009(2015).

[18] P.S. Dobal, A. Dixit, R.S. Katiyar, D. Garcia, R. Guo, A.S. Bhalla, *J. Raman Spectrosc.* **32**, 147(2001).

[19] R. Naik, J.J. Nazarko, *Phys. Rev. B* **61**, 11367(2000).

[20] S. Kamba, P. Samoukhina, F. Kadlec, J. Pokorny, J. Petzelt, I.M. Reaney, P.L. Wise, *J. Eur. Ceram. Soc.* **23**, 2639(2003).

[21] Y. J. Jiang, L.Z. Zeng, R.P. Wang, Y. Zhu, Y.L. Liu, J. Raman Spectrosc. **27**, 31(1996).

[22] A. K. Sood, N. Chandrabhas, S. Muthu DV, A. Jayaraman, Phys. Rev. B **51**, 8892(1995).

[23] J.A. Sanjurjo, R.S. Katiyar, S.P.S. Porto, Phys. Rev. B **22**, 2396(1980).

[24] O.A. Maslova, F.V. Shirokov, Y.I. Yuzyuk, M.E. Marssi, M. Jain, N. Ortega, R.S. Katiyar, Phys. Solid State **56**, 310(2014).

[25] Y. Yuan, C.J. Zhao, X.H. Zhou, B. Tang, S.R. Zhang, *J. Electroceram.* **25**, 212(2010).

[26] K.K. Mishra, A.T. Satya, A. Bharathi, V. Sivasubramanian, K. Murthy VR, A.K. Arora, J Appl. Phys. **110**, 123529(2011).

[27] C. Berbecaru, H.V. Alexandru, C. Porosnicu, A. Velea, A. Ioachim, L. Nedelcu, M. Toacsan, *Thin Solid Films* **516**, 8210(2008).

[28] S.W. Kim, H.I. Choi, M.H. Lee, J.S. Park, D.J. Kim, D. Do, M.H. Kim, T.K. Song, W.J. Kim, Ceram. Int. **39**, S487(2013).

[29] B. Wodecka-Dus, A. Lisinska-Czekaj, T. Orkisz, M. Adamzcyk, K. Osinska, L. Kozielski, D. Czekaj, Mater. Sci. Poland **25,** 791(2007).

[30] R.D. Shannon, Acta Cryst. **A32**, 751(1976).

[31] V.S. Puli, P. Li, S. Adireddy, D.B. Chrisey, J. Adv. Dielectr. **5**, 1550027(2015).

[32] K.K. Mishra, V. Sivasubramanian, R.M. Sarguna, T.R. Ravindran, A.K. Arora, *J. Solid State Chem.* **184**, 2381(2011).

[33] K.K. Mishra, S.N. Achary, S. Chandra, T.R. Ravindran, A.K. Sinha, M.N. Singh, A.K. Tyagi, *Inorg. Chem.* **55**, 8994(2016).

[34] S. Jr. Landi, I.R. Segundo, E. Freitas, M. Vasilevskiy, J. Carneiro, C.J. Tavares, *Solid State Commun.* **341**, 114573(2022).

[35] R. Lopez, R. Gomez, *J. Sol-Gel Sci. Technol.* **61**, 1(2012).

[36] A. Boubaia, A. Assali, S. Berrah, H. Bennacer, I. Zerifi, A. Boukortt, *Mater. Sci. Semicon. Proc.* **130**, 105837(2021).

[37] D. Zheng, H. Deng, Y. Pan, Y. Guo, F. Zhao, P. Yang, J. Chu, *Ceram. Int.* **46**, 26823(2020).

[38] I.R. Putra, H. Syafutra, H. Alatas, *Procedia Environ. Sci.* **33**, 607(2016).

[39] V.S. Puli, D.K. Pradhan, S. Adireddy, R. Martínez, P. Silwal, J.F. Scott, C.V. Ramana, D.B. Chrisey, R.S. Katiyar, *J. Phys. D Appl. Phys.* **48**, 355502(2015).

[40] S. Yun, X. Wang, D. Xu, *Mater. Res. Bull.* **43**, 1989(2008).

[41] C. Fu, C. Yang, H. Chen, Y. Wang, L. Hu, *Mater Sci Eng. B.* **119**, 185(2005).

[42] M. Sindhu, N. Ahlawat, S. Sanghi, R. Kumari, A. Agarwal, *J. Alloys Compd.* **575**, 109(2013).

[43] X.Q. Liu, T.T. Chen, Y.J. Wu, X.M. Chen, *J. Am. Ceram. Soc.* **96**, 1021(2013).

[44] X. Xu, G.E. Hilmas, *J. Am. Ceram. Soc.* **89**, 2496(2006).

[45] F.M. Pontes, E.R. Leite, E. Longo, J.A. Varela, E.B. Araujo, J.A. Eiras, *Appl. Phys. Lett.* **76**, 2433(200).

[46] Z. Song, S. Zhang, H. Liu, H. Hao, M. Cao, Q. Li, Q. Wang, Z. Yao, Z. Wang, *J. Am. Ceram. Soc.* **98**, 3212(2015).

[47] Q. Jin, Y.P. Pu, C. Wang, Z.Y. Gao, H.Y. Zheng, *Ceram. Int.* **10**, 1016(2017).

[48] Y.H. Huang, Y.J. Wu, W.J. Qiu, J. Li, X.M. Chen, *J. Eur. Ceram. Soc.* **35**, 1469(2015).

[49] J. Wang, L. Tang, B. Shen, J. Zhai, *Ceram. Int.* **40**, 2261(2014).

[50] N.H. Fletcher, A.D. Hilton, B.W. Ricketts, *J. Phys. D: Appl. Phys.* **29**, 253(1996).

[51] Z. Song, H. Liu, S. Zhang, Z. Wang, Y. Shi, H. Hao, M. Cao, Z. Yao, Z. Yu, *J. Eur. Ceram. Soc.* **34**, 1209(2014).

[52] Z. Dai, J. Xie, W. Liu, X. Wang, L. Zhang, Z. Zhou, J. Li, X. Ren, *ACS Appl. Mater. Interfaces* **12**, 30289(2020).

CHAPTER 4

Control of polysulfide shuttle: An approach via ferroelectric ($Ba_{0.9}Sr_{0.1}TiO_3$) nanoparticles doped sulfur cathode for high-capacity Li-S batteries.

4.1 Abstract

In this chapter we are reporting electrochemical performance of $Ba_{0.9}$ $Sr_{0.1}TiO_3$ (BS1T) having polarization of 14.58 μC/cm^2 doped sulfur/carbon-black/polyvinylidene fluoride (S/BS1T/CB/PVDF) composite cathodes. The performance of fabricated cathodes in terms of structural, electronic, morphological, and electrochemical response have been tested at various concentrations of $BS1T_x$ doping. Considering that polar substances have good affinity towards polysulfide and can provide a more stable reacting environment in the cathodic site, trapping polysulfide intermediates via induced permanent dielectric polarizability. It is expected that spontaneous polarization induced by asymmetric crystal structure of ferroelectrics provide internal electric fields and increase chemisorption with heteropolar reactions. X-ray diffraction spectra confirms tetragonal symmetry (c/a=1.0073), Raman spectroscopic study confirms Raman modes (A1(TO1), A1(TO2), A1(TO3) and A1(LO3)) of the tetragonal orientation for BS1T modified composites. All the compositional cations are observed from SEM images confirm homogeneous distribution of BS1T in the sulfur cathode system having grain sizes (1-1.5 μm) which is based on microscopic analysis. BS1T coupled C-S composite cathodes improve the electrochemical performance in comparison with the cathodes composed of C-S. The high capacity for S/$BS1T_x$/CB/PVDF composites of the order of 820 mAh/g @ 100 mA/g have been achieved for the $S_{50}BS1T_{30}CB_{10}PVDF_{10}$ composite cathode and very stable response

till 100^{th} cycles attributes polysulfide migration is effectively reducing due to ferroelectric particles doping in the composite cathode. Two plateaus were observed in between 2.3V-2.0V and 2.0V-1.5V in the charge/discharge characteristics and high cyclic stability substantiate the superior performance of the designed ferroelectric nanoparticles doped S/CB composite cathode materials due to the efficient reduction in the polysulfide shuttle effect in these composite cathodes.

4.2 Introduction

Lithium–sulfur (Li–S) batteries are promising candidates for next generation energy storage systems owing to their high energy density and low cost [1]. Typically, Li-S batteries consist of elemental sulfur (S_8) cathodes and Li anodes. Based on multi electron conversion mechanism between S_8 and Li metals, Li-S batteries deliver high theoretical specific capacities of 1675 mAh/g and specific energy of 2600 Wh/kg, which is almost four times that of Li-ion batteries [2-3]. However, the practical application of Li/S batteries is greatly hampered by some persistent problems including (i) sulfur and discharge products (Li_2S_2 and/or Li_2S) has a low electrical conductivity, affecting the reaction rate of the battery; (ii) the Li_2S and other insoluble compounds are generated and cover the active compounds during cycling, which inhibits access of lithium ions and degrades the conductive network, and (iii) the high-order soluble polysulfides can penetrate through the separator to the lithium negative electrode, where they are reduced to insoluble Li_2S or Li_2S_2, and the following polysulfides react with these fully reduced sulfides to form lower-order polysulfides, which become concentrated at the anode side and diffuse back to the positive electrode and are then re-oxidized into high-order polysulfides [4-6].Such shuttle between the anode and cathode induces deposition of solid Li_2S_2 and Li_2S on the anode

and loss of the active material, which leads to low Columbic efficiency, low utilization of the sulfur cathode, and severe degradation of cycle life. To overcome these problems, many efforts have been explored to enhance the electrical conductivity of the cathode and suppress the loss of soluble polysulfide intermediates during cycling. The use of conductive nanocarbon (e.g., mesoporous carbon [7-10], carbon nanotubes (CNTs) [11-14], graphene [15-17], CNT/graphene hybrids [18], carbon hollow spheres [19], etc.) and polyaniline as well as polyacrylonitrile [20-21] etc. gives rise to advanced composite cathode with excellent conductivity, robust electron/ion pathway, as well as superior reversible charge discharge capacity and cycling performance. To retard the shuttle of polysulfides is still a key issue to obtain Li-S cells with superior Li storage performance. One of the most promising strategies is to build the functional porous and conductive host to immobilize sulfur and anchor LiPSs [22]. Wei et. reported that ferroelectric barium titanate ($BaTiO_3$) could effectively anchor polysulfides by the built in electric field arising from spontaneous polarization. By applying $BaTiO_3$ as a cathode additive, the electrochemical performances of assembled cells remarkably improved and shows the role of polarized materials in lithium sulfur battery [23]. More recently from our group Katiyar et. al reported the role of spontaneously polarized bismuth ferrite ($BiFeO_3$) doped S/SWCNT composite cathode as well as $BiFeO_3$ coated separator to suppress polysulfide shuttle in Li-S batteries [24]. $BaSrTiO_3$ has attracted considerable research interest due to its strong dielectric and ferroelectric polarization under electric field. The strontium (Sr) concentration into $BaTiO_3$ offers high dielectric constant and low leakage current [25]. Additionally, in nano ranges, the ferroelectric structure has demonstrated completely different features from bulk

structure. The dependence of ferroelectric characteristics on grain size is due to its electrical properties [26].

4.3 Experimental

4.3.1 Materials & method

Sulfur (S, purity 99.5%), Carbon black (99.00%), N-Methyl 1-2-pyrrolidone (NMP 98%) were purchased from Sigma Aldrich and used without further purification. $Ba_{0.9}Sr_{0.1}TiO_3$ (BS1T) where in $BS1T_x$ (x = 0.2, 0.3,) samples were prepared by high-energy ball milling and solid-state reaction method. The stoichiometric ratio of starting raw materials $BaCO_3$ (99.997%), $SrCO_3$ (99.998%), and TiO_2 (99.988%) were mixed along with isopropanol using planetary ball milling (Pulverisette Fritsch Planetary Mill). The powder was screened using a mesh of 150 µm size to obtain a fine powder of almost uniform particle size. The powder was pre-calcined at 850 ◦C/4 h, followed by thorough pulverization and calcined at 1150 ◦C/2 h at a ramp rate of 5 ◦C/min. The ball milling was suspended for 20 min after every 1 h of milling to cool down the milling system. The aluminum (Al) foil (25µm thickness and purity 99.45%), Lithium foil, (0.75×19mm, 99.9%) and polypropylene separator (Celgard2400:25 µm), B is(trifluoromethylsulfonyl)imide lithium salt (LiTFSI; 98+%), lithium nitrate ($LiNO_3$; anhydrous, 99.999%), 1,2-dimethoxyethane (DME; 99+%), 1,3-dioxolane (DOL; 99.5%) were purchased from Alfa Aesar and used without further purification for the preparation of 1M LiTFSI as the electrolyte. The sulfur (S), BS1T, carbon black (CB), and PVDF were mixed. The slurry of S/BS1T/CB/PVDF composite was prepared in NMP via ball milling and coated on aluminum foil of thickness (25µm) via doctor blade. After drying in vacuum oven (40 ^{0}C) till 15 hrs. electrodes were cut into disc of 13 mm for cathode. The

polypropylene (PP) separator (Celgard 2400) was used. The coin cells (CR2032) were assembled in an Ar-filled glove box (MBraun, USA) with H_2O, and O_2 <0.1ppm.

4.4 Characterization

The X-ray diffraction (XRD) measurements were carried out using a Rigaku Smart Lab X-ray diffractometer equipped with CuKα radiation (λ = 1.5418 Å) operated in a Bragg-Brentano (θ–2θ) geometry at 40 kV and 44 mA. The crystal structure and phase purity of the compounds were checked in a slow scan mode using a 2θ step size of 0.05^0. The analyses of the XRD patterns were carried out using FullProf suite software 7.70 (Version April 2022). Raman spectroscopy studies were carried out employing a HORIBA Jobin Yvon micro-Raman spectrometer (model: T64000) equipped with a 50× long working distance objective lens in a back-scattering geometry ($2\theta = 180^0$) using a 514.5 nm line of an Ar+ ion laser (Coherent, Innova 70-C). Raman spectra with improved signal-to-noise ratio were measured by optimizing the laser power and acquisition time.

The surface morphology of the samples was studied using scanning electron microscopy (SEM) (model: JEOL/MP) equipped with a backscattered electron detector operating at an accelerating voltage of 20 kV and 3300× magnifications. SEM-based energy dispersive X-ray spectra (EDS) (model: JSM-IT500HR-JEOL) were measured from the crack surface of the sintered pellets to infer their chemical compositions. Galvanostatic charge-discharge curves were measured using MTI battery tester at different current densities within the voltage range 1.5-3.2 V (Vs Li^+/Li). The cyclic voltammetry @ 0.1mV/s was used for the testing of cycling performance and stability of the cathode material. Electrochemical impedance spectroscopy (EIS) was performed on symmetric cells of $S_{60}BS1T_{20}CB_{10}PVDF_{10}$ & $S_{50}BS1T_{30}CB_{10}$ $PVDF_{10}$ using an Arbin-32MTS Pro

battery tester at open circuit potential (OCP) with a signal amplitude of 10 mV, in a frequency range from 1 MHz to 50 Hz.

4.5 Results & discussion

4.5.1 X-ray diffraction

Figure 4.1 represents X-ray diffraction spectra of pristine carbon black, $Ba_{0.9}Sr_{0.1}TiO_3$ (x=0.1), Carbon black, Sulfur, $S_{50}BS1T_{30}C_{10}PVDF_{10,}$ & $S_{60}BS1T_{20}C_{10}PVDF_{10}$ composites obtained from Rietveld analysis of the high-resolution powder XRD patterns measured in the angle (2-theta) range from 10^0 to 100^0 at room temperature. The $S_{60}BS1T_{20}CB_{10}PVDF_{10}$ & $S_{50}BS1T_{30}CB_{10}PVDF_{10}$ composite cathode material shows all the sulfur diffraction peaks, together with an extra peak at 25.60, showing the carbon (002) diffraction peak together with BS1T diffraction peaks, consistent with ICDD # 861518. However, variation in the intensity of peaks indicates the lack of long-range order due to sulfur confinement into carbon and $BS1T_x$. The size of sulfur particles is ~20–25 nm, and that of carbon is 30–40 nm, as estimated from the Scherrer formula [27-28]

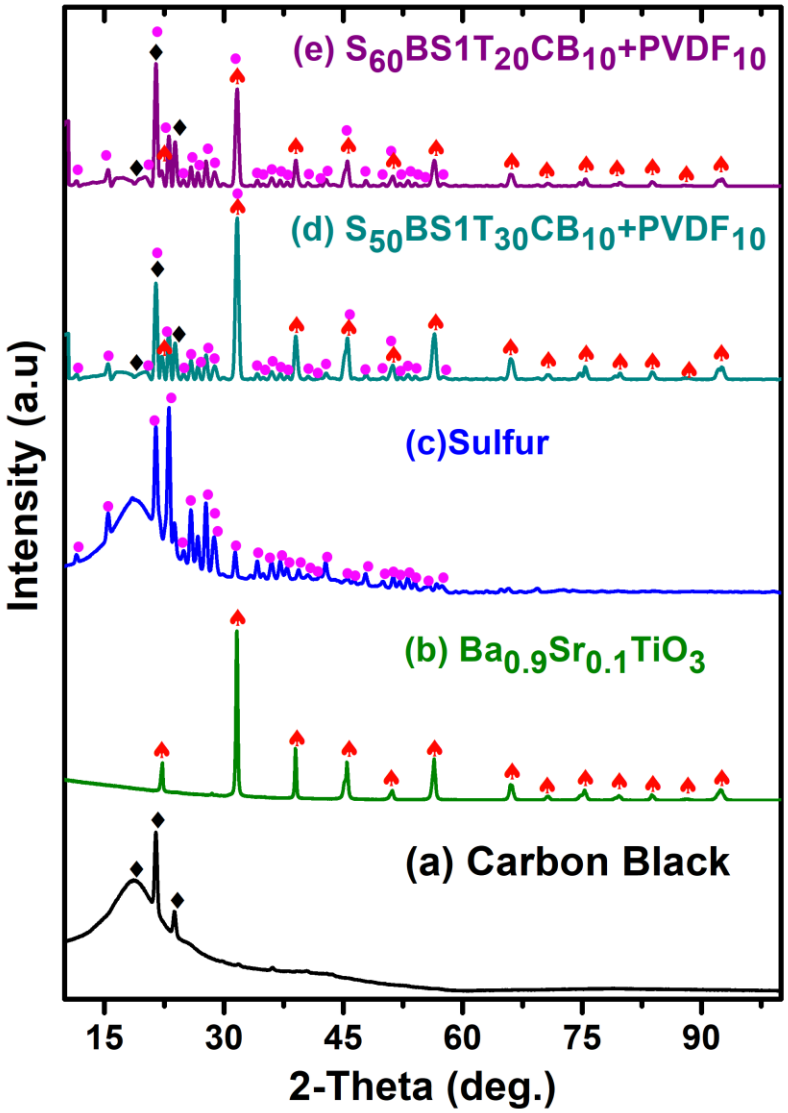

Figure 4.1 *X-ray diffraction spectra for (a) Carbon black (b) BS1T (c) Sulfur (d) $S_{50}BS1T_{30}C_{10}PVDF_{10}$ (e) $S_{60}BS1T_{20}C_{10}PVDF_{10}$.*

4.5.2 Raman spectra

Figure 4.2 (a, b, c, d, e, f) show Raman spectra of pristine $Ba_{0.9}Sr_{0.1}TiO_3$, Carbon black, sulfur, $S_{60}BS1T_{20}C_{10}PVDF_{10}$, $S_{50}BS1T_{30}CB_{10}PVDF_{10}$ composites & polarization loop (p-E) of $Ba_{0.9}Sr_{0.1}TiO_3$ respectively. Raman spectra for pristine and composites are

summarized in Figure 4.2 (a, b, c, d, e). Raman spectroscopic study confirms Raman modes ($A_1(TO_1)$, $A_1(TO_2)$, $A_1(TO_3)$ and $A_1(LO_3)$) of the tetragonal orientation for BS1T modified composites. The low wavenumber peaks noticed in Figure 4.2 (c) at 26, 44, 49, and 84, correspond to A1(LO) phonon modes, whereas vibrational peaks noticed at 153, 217, and 471 cm^{-1} correspond to E(TO) modes for the BS1T system. The observation of modes these substantiates the phase purity of BS1T nanoparticle's tetragonal structure [29]. The characteristic carbon peaks are identified at 1350 and 1580 $\mathbf{cm^{-1}}$, which correspond to D and G characteristic bands [30]. These characteristic carbon vibration modes are observed in all S/BS1T_x/CB/PVDF composite samples. Figure 4.2 (b, e), suggesting the efficient integration of carbon into the S/BS1T_x/CB/PVDF composite matrix. Further, the rhombic sulfur characteristics are observed in all S/BS1T_x/CB/PVDF composite cathode materials, implying the efficient impregnation of sulfur with carbon in these composite cathode samples.

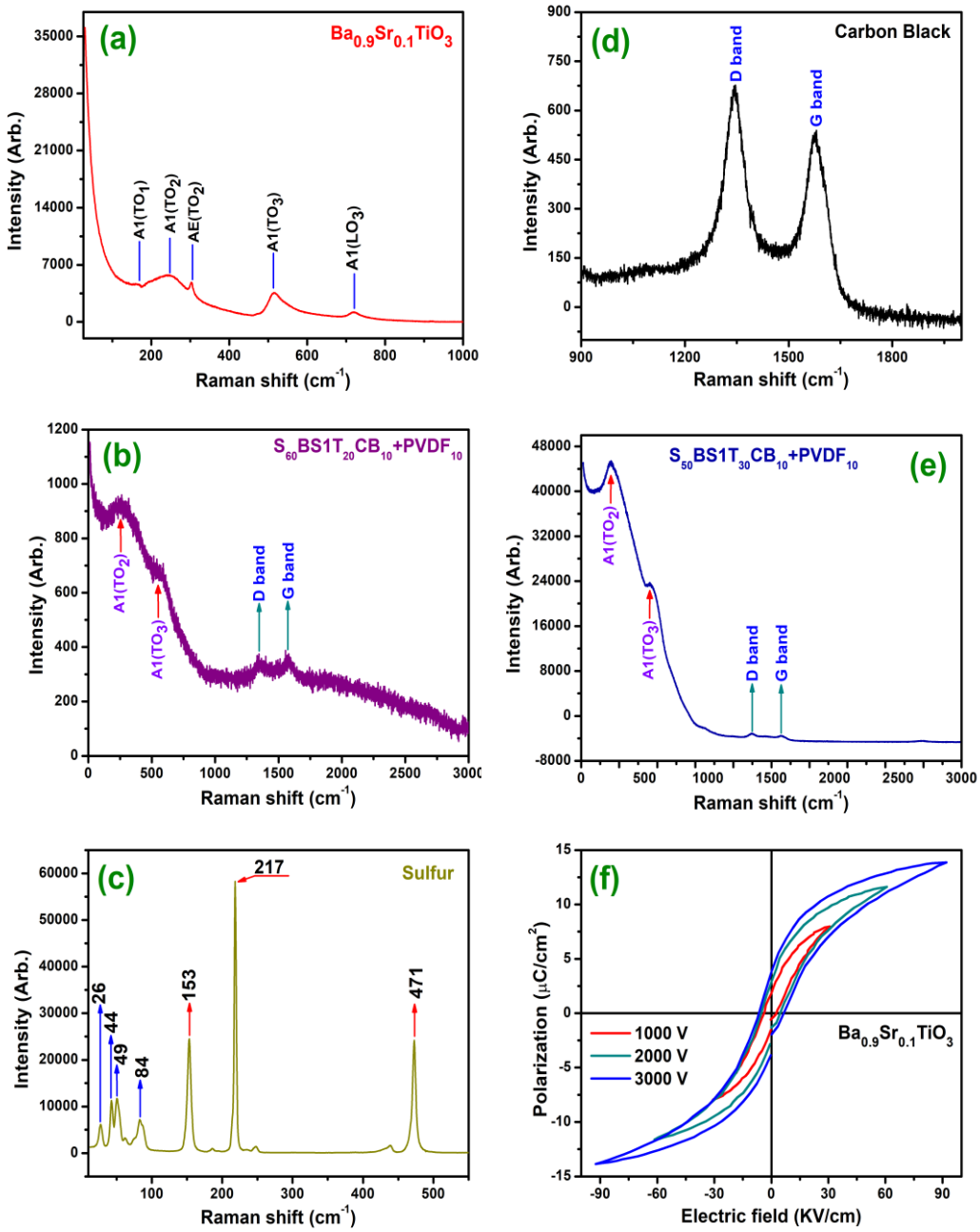

Figure 4.2 *Raman spectra of (a) $Ba_{0.9}Sr_{0.1}TiO_3$, (b) $S_{60}BS1T_{20}CB_{10}PVDF_{10}$ composite (c) Sulfur (d) Carbon black, (e) $S_{50}BS1T_{30}C_{10}PVDF_{10}$ & (f) Polarization loop(p-E) of $Ba_{0.9}Sr_{0.1}TiO_3$.*

As shown in Figure 4.2(f) the BS1T ferroelectric particles contributing to the polarization which induces modifications in S/CB/PVDF composite cathode. Generally,

polar substances have an affinity toward polysulfides and can provide a more stable reacting environment at the cathode site [31-32]. It is well known that ferroelectric materials induce permanent dielectric polarizability [33] via which suppression of polysulfide intermediates is expected. This force is determined to alter the path of dissolved charged polysulfide ions, thus enhancing electrochemical performance by promoting the suppression of these polysulfide ions.

4.5.3 Surface morphology

Figure 4.3 (a,b) shows SEM images of $S_{60}BS1T_{20}C_{10}PVDF_{10}$, $S_{50}BS1T_{30}CB_{10}PVDF_{10,}$ and Figure 4.3 (c,d) shows EDAX spectra of $S_{60}BS1T_{20}C_{10}PVDF_{10}$ & $S_{50}BST_{30}C_{10}PVDF_{10}$ composites**.** The material surrounding the sulfur matrix is acting as a protective layer, showing the morphology of $S_{60}BS1T_{20}CB_{10}PVDF_{10}$, & $S_{50}BS1T_{30}CB_{10}PVDF_{10}$ composite materials in Figure 4.3 (a, b) respectively. The surface area and structural features provide defect sites at which lithium ions may be adsorbed to the surface of loosely bound carbons layers [34]. BS1T, CB, and sulfur showing the close contact between BS1T, CB, and sulfur, may be an excellent electron pathway for insulating sulfur and adsorption sites for soluble polysulfides.

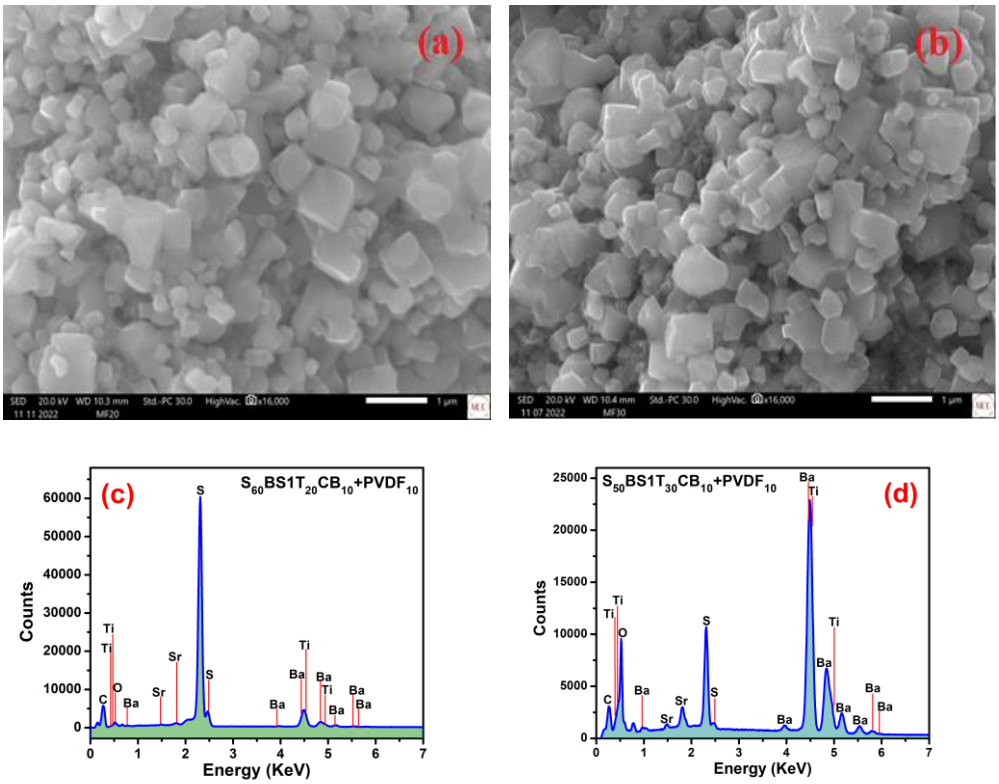

Figure 4.3 *SEM images of (a)$S_{60}BS1T_{20}CB_{10}PVDF_{10}$ (b) $S_{50}BS1T_{30}CB_{10}PVDF_{10}$ EDAX spectra of (c) $S_{60}BST_{20}CB_{10}PVDF_{10}$ (d) $S_{50}BST_{30}CB_{10}PVDF_{10}$ composites.*

4.6 Electrochemical performance

4.6.1 Charge-discharge

Figure 4.4(a, b, c, d) showing charge-discharge profiles for $S_{60}BS1T_{20}CB_{10}PVDF_{10}$, and $S_{50}BS1T_{30}CB_{10}PVDF_{10}$ @100mA/g & 200mA/g respectively up to 100 cycles. As shown in Figure 4.4 (a, b) it has been observed that the maximum capacity for $S_{60}BS1T_{20}CB_{10}PVDF_{10}$ composite cathode @ 100 mA/10 @1st cycle is 750 mAh/g which reduces to 348 mAh/g after 100th cycle with capacity retention of 46.4%, However the observed specific capacity of the same composite cathode of $S_{60}BS1T_{20}CB_{10}PVDF_{10}$ @ 200 mA/g in 1st cycle is 300 mAh/g which reduces to 246 mAh/g after 100th cycle.

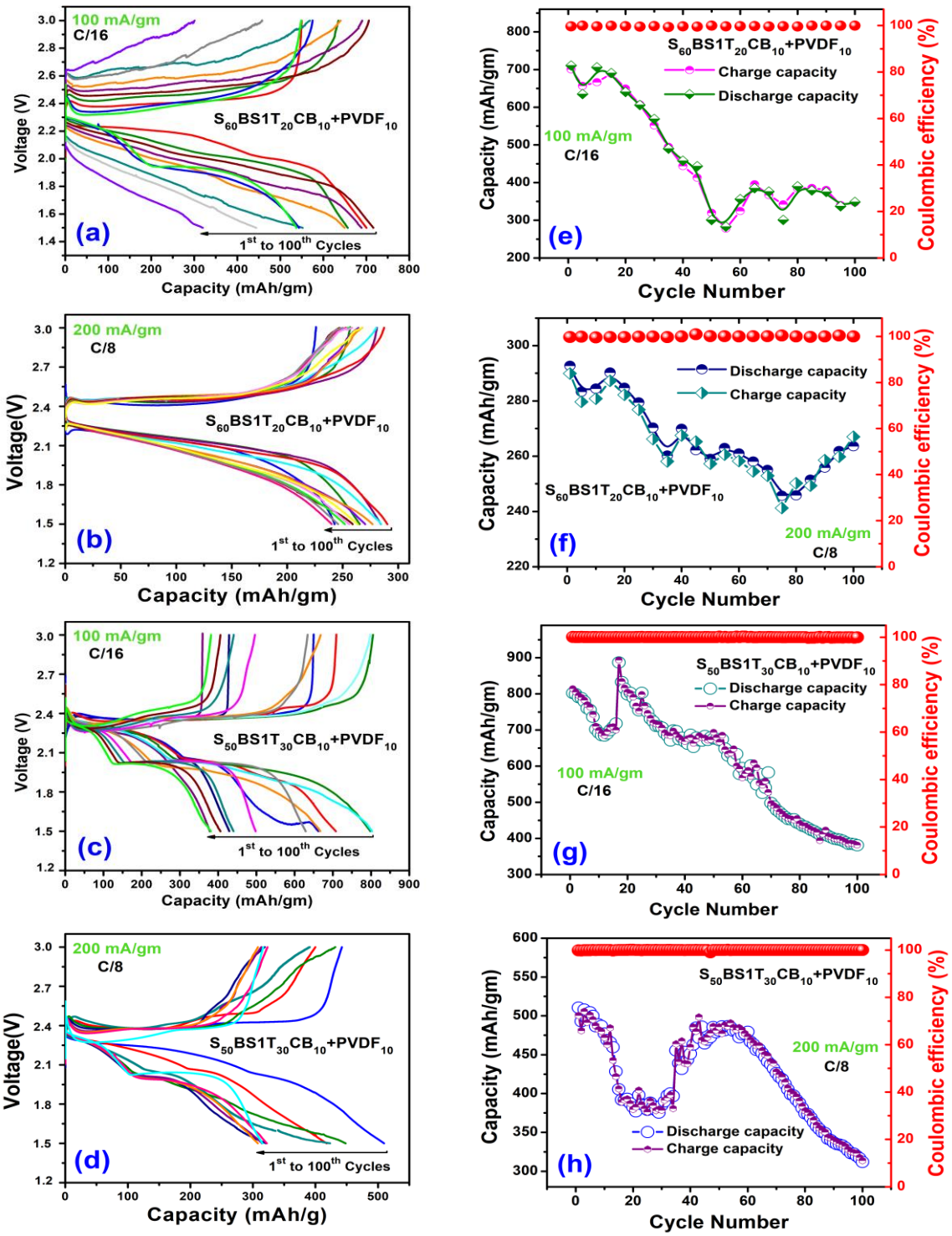

Figure 4.4 *Capacity vs voltage performance of $S_{60}BS1T_{20}CB_{10}PVDF_{10}$ (a)100mA/g & (b) 200mA/g,$S_{50}BS1T_{30}CB_{10}PVDF_{10}$(c)100 mA/g&(d)200 mA/g, Cycling performance of $S_{60}BS1T_{20}CB_{10}PVDF_{10}$ (e)100 mA/g & (f) 200 mA/g, $S_{50}BS1T_{30}CB_{10}PVDF_{10}$ (g) 100 mA/g & (h) 200 mA/g.*

The specific capacity for $S_{50}BS1T_{30}CB_{10}PVDF_{10}$ @100mA/g in 1st cycle is 820 mAh/g which reduces to 400 mAh/g after 100th cycle with capacity retention of 48.7%, However the observed specific capacity of $S_{50}BS1T_{30}CB_{10}PVDF_{10}$ composite cathode @ 200 mA/g in 1st cycle is 540 mAh/g which reduces to 322 mAh/g after 100th cycle with capacity retention 59.6%. The improvement in capacity retention for $S_{50}BS1T_{30}CB_{10}PVDF_{10}$ composite cathode due to higher concentration of BS1T reaches up to 59.6% showing that spontaneous ferroelectric polarization of BS1T nanoparticles facilitates the migratory of Li-ions and eliminate the concentration gradient of Li-ions near electrode surface to control the polysulfide formation [35]. It has been found that coupling of BS1T nanoparticles anchoring the polysulfides in the cathode. When spontaneous polarized BS1T particles are added into the cathode, the dissoluble heteropolar polysulfides are most likely absorbed around the nanoparticles due to the induced internal electric field, attributes the control of reactions from S_8 to Li_2S_2 or Li_2S_4, also the strong polarization of the ferroelectric nanoparticles influences distribution of Li-ions, yielding diffusion pathways in the electrolyte/active material, which accelerates the transfer speed of Li-ions, might eliminating the concentration gradient of Li-ions near to the deposition surface. Thus, the internal electric field of the ferroelectric BS1T particles, played an important role to inhibit LiPSs shuttling leading to an improvement of the cycle stability of Li-S batteries. The observed capacity retention (CR%) has been found to be improved for S/BS1T/CB/PVDF composite cathodes @ 100 mA/g.

4.6.2 Cyclic voltammetry & EIS performance

Figure 4.5 (a, b), shows cyclic voltammetry (CV) curves for S/BS1T/CB/PVDF composite cathodes @0.1mV/s. Generally, in Li-S batteries cathode materials during the

cycling show two reduction peaks, in which higher one corresponds to the transformation of elemental sulfur (S_8) into long chain polysulfides (Li_2S_n, n>4) and the lower one belongs to the conversion of long-chain polysulfides into short chain polysulfides ((Li_2S_n, n<_4) as well as the product of lithium sulfide (Li_2S) [36]. It has been observed that the composite cathode of $S_{60}BS1T_{20}CB_{10}PVDF_{10}$ shows oxidation peaks at 2.70 V & 2.5 V, however reduction peak is at 2.0 V during cycling.

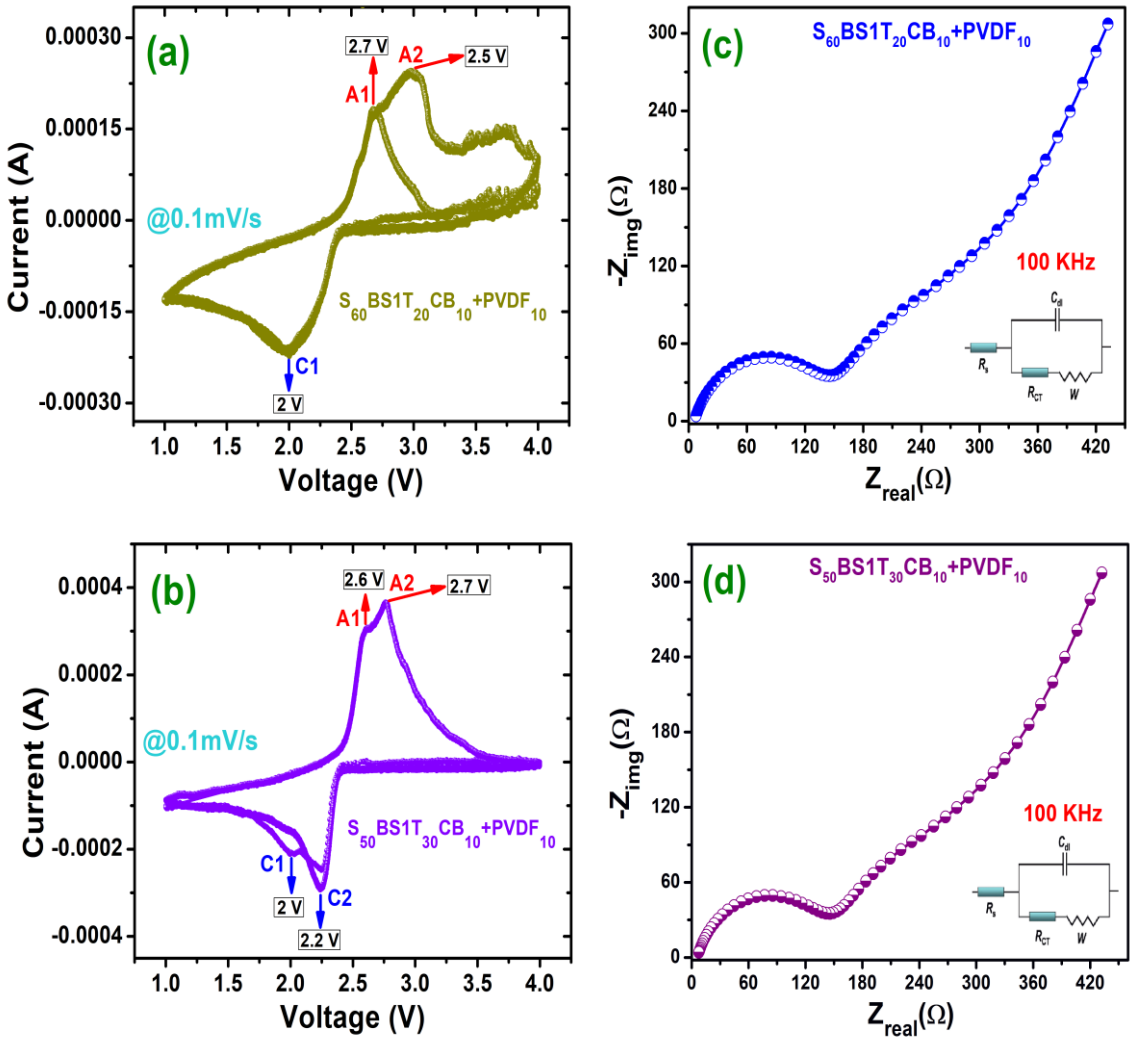

Figure 4.5 (a, c) *Cyclic voltammogram & EIS spectra of $S_{60}BS1T_{20}CB_{10}PVDF_{10}$ (b, d) Cyclic voltammogram & EIS spectra of $S_{50}BS1T_{30}CB_{10}PVDF_{10}$ composite electrodes.*

As shown in Figure 4.5(b) the oxidation peaks for $S_{50}BS1T_{30}CB_{10}PVDF_{10}$ composite are at 2.6 V & 2.7 V and reduction peaks are at 2.0 V & 2.2V suggests an enhanced kinetics of the reduction reaction with the BS1T doped cathode as expected due to the alteration in the kinetics might be due to ferroelectric nanoparticles coupling & reversible transformation of Li_2S to short/long chain LiPSs and finally to S_8 [32]. Figure 4.5(c, d) showing the EIS spectra of $S_{60}BS1T_{20}CB_{10}PVDF_{10}$ & $S_{50}BS1T_{30}CB_{10}PVDF_{10}$ composite cathodes. In the case of symmetric cells with the positive and blocking electrodes, We have confirmed that the active material, sulfur, does not contribute to the resistance of the positive electrode, however due to inclusion of BS1T up to 20 & 30 wt.% and applying RC(R)W circuit model for interfacial parameters , The observed values for $S_{60}BS1T_{20}CB_{10}PVDF_{10}$ are Rs (1.142 Ω) C=1.333 µF R_{ct} (289.5.Ω) and W(0.003719) similarly the observed values for $S_{50}BS1T_{30}CB_{10}PVDF_{10}$ are as Rs (2.688) C= 9.1 µF R_{ct} (145 Ω) and W(0.02312) showing the improved diffusion pathways for Lithium ions [37].

4.7 Conclusions

In summary, polycrystalline $BS1T_x$ (x = 0.2 & 0.3) ferroelectric particles doped in S/CB composite cathodes were prepared using a high energy ball milling and the solid-state reaction method. Rietveld analysis of XRD data suggests the single-phase formation of the compounds. BS1T has a tetragonal phase. Ferroelectric polarization studies suggested the highest polarization of is ~14.58 µC/cm^2 for BS1T. The surface morphology as observed from SEM images, showing interconnected network of composites. The Li-S batteries fabricated based on optimized hybrid cathodes like $S_{50}BS1T_{30}CB_{10}PVDF_{10}$ & $S_{60}BS1T_{20}CB_{10}PVDF_{10}$ composites tested @100 mA/g & 200 mA/g with polypropylene (PP) separator showing specific capacities ~ 820mAh/g & ~540 mAh/g respectively, with

improved capacity retention up to 60%. The improvement in capacity retention is attributed to the suppression of polysulfides via effective spontaneous polarization provided by the ferroelectric nanoparticles. It is suggested that the role of ferroelectric nanoparticles embedded in the cathode controls the polysulfides formation as an adsorption center due to BS1T doped cathode in such batteries. It is suggested that BS1T particles mixed in cathode render dipoles permanently polarized due to which polysulfides exposure to the electrolyte will be minimal. This strategy via inducing ferroelectric polarization within the cathode provides an opportunity and promising solution to control polysulfides formation and achieve improved capacity retention in the high energy Li-S batteries.

4.8 References

[1] Y. Li, S. Gui, Matter, **4(4)**1142-1188 (2021)

[2] L. Hou, X. Zhang, B. Li., Q. Zhang, Materials Today, **45**, 62-76 (2021).

[3] Y. Yang, G.Y. Zheng, Y. Cui, Chem. Soc. Rev. **42**, 3018-3032 (2013).

[4] A. Manthiram, Y.Z. Fu, Y.S. Su, Acc. Chem. Res. **46**, 1125-1134 (2013).

[5] X.L. Ji, L.F. Nazar, J. Mater. Chem. **20**, 9821-9826 (2010).

[6] X.L. Ji, K.T. Lee, L.F. Nazar, Nat. Mater. **8**, 500-506 (2009).

[7] S. Xin, Y.X. Yin, L.J. Wan, Y.G. Guo, Part. Part. Syst. Char. **30**, 321-325 (2013).

[8] D. Li, F. Han, S. Wang, F. Cheng, Q. Sun, W.C. Li, ACS Appl. Mater. Interfaces **5**, 2208-2213(2013).

[9] F.G. Sun, J.T. Wang, H.C. Chen, W.C. Li, W.M. Qiao, D.H. Long, L.C. Ling, ACS Appl. Mater. Interfaces **5**, 5630-5638 (2013).

[10] G.M. Zhou, D.W. Wang, F. Li, P.X. Hou, L.C. Yin, C. Liu, G.Q. Lu, I.R. Gentle,

[11] H.M. Cheng, Energy Environ. Sci. **5**, 8901-8906 (2012).

[12] S. Dorfler, M. Hagen, H. Althues, J. Tubke, S. Kaskel, M.J. Hoffmann, Chem. Commun. **48**, 4097-4099 (2012).

[13] X.F. Liu, Q. Zhang, J.Q. Huang, S.M. Zhang, H.J. Peng, F. Wei, J. Energy Chem. **22,** 341-346(2013).

[14] M. Hagen, S. Dorfler, H. Althues, J. Tubke, M.J. Hoffmann, S. Kaskel, K. Pinkwart, J. Power Sources **213**, 239-248 (2012).

[15] G.Y. Zheng, Q.F. Zhang, J.J. Cha, Y. Yang, W.Y. Li, Z.W. Seh, Y. Cui, Nano Lett. **13**, 1265-1270 (2013).

[16] J.Q. Huang, X.F. Liu, Q. Zhang, C.M. Chen, M.Q. Zhao, S.M. Zhang, W.C. Zhu, W.Z. Qian, F. Wei, Nano Energy **2**,314-321 (2013).

[17] H. Wang, Y. Yang, Y. Liang, J.T. Robinson, Y. Li, A. Jackson, Y. Cui, H. Dai, Nano Lett. **11**, 2644-2647 (2011).

[18] L.W. Ji, M.M. Rao, H.M. Zheng, L. Zhang, Y.C. Li, W.H. Duan, J.H. Guo, E.J. Cairns, Y.G. Zhang, J. Am. Chem. Soc. **133**, 18522-18525 (2011).

[19] M.Q. Zhao, X.F. Liu, Q. Zhang, G.L. Tian, J.Q. Huang, W.C. Zhu, F. Wei, ACS Nano **12**, 10759-10769(2012).

[20] Y. Li, B. Xing, J. Ma, S. Peng, Y. Li, K. Zhou, Q. Long, G. Xu, S. Yang, Journal of Materials Research and Technology, **20**, 3714-3722 (2022).

[21] Y. H. Peng, B. Li, J. Xie, L. Kong, M. Zhao, Adv Energy Mater, **9 (1)**, 1802768-1802776 (2019).

[22] H. Wang, Y. Yang, Y. Liang, J.T. Robinson, Y. Li, A. Jackson, Y. Cui and H. Dai, Nano Lett.**11**, 2644-2647(2011).

[23] K. Xie., Y. You, K. Yuan, W. Lu, K. Zhang, F. Xu, M. Ye, S. Ke, C. Shen and X. Zeng, Adv. Mater., **29**, 1604724(2017).

[24] R.K. Katiyar, C.Z. Zuluaga Gomez, S. Katiyar, B. Tripathi, G. Morell, B.R. Weiner, Ram S Katiyar, APL Materials, **11**, 051115 (2023).

[25] K.A. Razak, A. Asadov**,** J. Yoo, E. Haemmerle, W. Gao, J. Allys. Compd., **449**, 19-23 (2008).

[26] V.R. Mudinepalli, L. Feng, W. Lin, B.S. Murty, J. Adv. Ceram., **4**, 46-53 (2015).

[27] S. Zheng, P. Han, Z. Han, H. Zhang, Z. Tang, J. Yang, Sci. Rep., **4,** 4842-4846(2014).

[28] B. Zhang, Energy Environ. Sci., **3,** 1531-1537 (2010).

[29] M.K. Singh, H.M. Jang, S. Ryu, M.H. Jo, Appl. Phys. Lett., **88**, 42907–42915(2006).

[30] L. Xue, W. Chen, Y. Hu, J. Xiong, Nano energy, **79**, 105481 (2021).

[31] T. Yim, S.H. Han, N.H. Park, M.S. Park, J.H. Lee, J. Shin, J.W. Choi, Y. Jung, Y.N. Jo, J.-S. Yu, K.J. Kim, Adv. Funct. Mater.**, 26 (43)** 7817–7823(2016).

[32] K. Xie, Y. You, K. Yuan, W. Lu, K. Zhang, F. Xu, M. Ye, S. Ke, C. Shen, Adv. Mater., **29** (6) 1604-1661 (2017).

[33] G.H. Haertling, J. Am. Ceram. Soc., **82 (4)** 797–818 (1999).

[34] J. Sun, S. Xiao, S. Jiang, G. Li, Y. Huang, J. Geng, Chem. Mater., **27**, 4594–4599(2015).

[35] Y. Wang, Z. Wan, F. Zheng and Li Lu, Advance. Science, **9**, 2105849(2022).

[36] Y Tian, G. Li, Y. Zhang, D. Luo, X. Wang, Y. Zhao, H. Liu, P. Ji, X. du, and J. Li, Ad. Mater. **13**, 1904876-1904882(2019).

[37] S.R. Das, R.N.P. Choudhary, P. Bhattacharya, R.S. Katiyar, P. Dutta, A. Manivannan, M.S. Seehra, Structural and Multiferroic Properties of La-Modified $BiFeO_3$ Ceramics. *Journal of Applied Physics,* **101** ,34104 (2007).

CHAPTER 5

Switchable macroscopic polarization ($Ba_{0.9}Sr_{0.1}TiO_3$) induced polysulfides adsorption in sulfur cathode for high energy density Li-S batteries.

5.1 Abstract

In this chapter we are reporting electrochemical performance of $Ba_{0.9}$ $Sr_{0.1}TiO_3$ (BS1T)doped sulfur/carbon black/PVDF composites having polarization of 14.58 $\mu C/cm^2$ as cathode material for Li-S batteries. BS1T particles have been synthesized using sol-gel and solid-state techniques. Ferroelectric materials have attracted much attention due to their unique polarization. It is found that spontaneous polarization caused by asymmetric crystal structure offers opportunities in electrochemical properties of materials. The spontaneous polarization helps to build up an electric field and induces macroscopic charges on the surface of ferroelectrics. In consideration of the fact that polysulfides are heteropolar can be anchored in the cathode due to internal field originated from spontaneous polarization of BS1T particles. The fabricated composite cathodes of $S_{40}BS1T_{40}CB_{10}PVDF_{10}$ tested in terms of structural, electronic, morphological, and electrochemical characteristics. X-ray diffraction spectra confirms tetragonal symmetry (c/a=1.0073), Raman spectroscopic study confirms Raman modes ($A_1(TO_1)$, $A_1(TO_2)$, $A_1(TO_3)$ and $A_1(LO_3)$) of the tetragonal orientation for BS1T modified composites. All the compositional cations are observed from SEM images confirm homogeneous distribution of BS1T in the sulfur cathode system. BS1T doped S/CB/PVDF composite cathodes improve the electrochemical performance and show high capacity of the order of 1080 mAh/g which retains to 395 mAh/g after 100^{th} cycles @ 100 mA/g. The capacity retention

attributes polysulfides effectively suppressed via intercalation of BS1T ferroelectric particles in the sulfur cathode for high energy density Li-S batteries.

5.2 Introduction

Lithium-sulfur (Li-S) batteries deliver theoretical capacity of 1675 mAh/g and energy density up to 2600 Wh/kg, which is five times higher than that of lithium-ion batteries [1-3]. The practical implementation is still puzzled by several problems involving the insulating nature of sulfur, large volume variation upon cycling and dissolution behavior of intermediate polysulfides [4-6]. Ferroelectric materials have attracted much attention due to their unique ferroelectric, piezoelectric, and other physical properties, which have facilitated the widespread applications in electronics, communications, medical diagnostics, and electrochemical devices. Recently, it is found that "spontaneous polarization," caused by the asymmetric crystal structure, offers new opportunities in the field of electrochemistry [7]. The spontaneous polarization helps to build an internal electric field and induces macroscopic charges on the surface of ferroelectrics. The polysulfides are heteropolar and will be chemisorbed on the surface of ferroelectric particles [8]. Wei et al. reported that ferroelectric barium titanite ($BaTiO_3$) could effectively anchor polysulfides by the built-in electric field arising from the spontaneous polarization. By applying $BaTiO_3$ as a cathode additive, the electrochemical performances of assembled cell were remarkably improved, which shows the prospect of spontaneously polarized materials in lithium-sulfur battery [9]. Tripathi et.al. reported that adding $BiFeO_3$ (BFO) nanoparticles to C-S composite cathodes, polysulfides can easily be trapped in the regular cathode materials because of the intrinsic internal electric field of BFO [10]. The specific capacity and energy density of electrode materials are strongly related to the diffusion of

ions/electrons. Perovskite based metal oxides have emerged as active materials in energy storage and conversion devices owing to their high chemical and thermal stability properties. Barium strontium titanate ($BaSrTiO_3$) an eminent perovskite oxide has been widely used as active material in super capacitors due to its thermal stability, high redox active properties, and tetragonal structure. The polarized nanoparticles can accelerate the transfer of Li-ions, which eliminates the shortage of Li-ions at the surface of anode. It is expected that the BST particles having spontaneous polarization and high conductivity by providing free carriers doped in S/CB/PVDF composite cathodes may solve the polysulfide formation effect and could enhance the stability of sulfur cathode for Li-S batteries.

5.3 Experimental

5.3.1. Materials & method

Sulfur (S, purity 99.5%), Carbon black (99.00%), N-Methyl 1-2-pyrrolidone (NMP 98%) were purchased from Sigma Aldrich and used without further purification. $Ba_{0.9}Sr_{0.1}TiO_3$ (BS1T) where in BST_x (x = 0.4) samples were prepared by high-energy ball milling and solid-state reaction method. The stoichiometric ratio of starting raw materials $BaCO_3$ (99.997%), $SrCO_3$ (99.998%), and TiO_2 (99.988%) were mixed along with isopropanol using planetary ball milling (Pulverisette Fritsch Planetary Mill). The aluminum (Al) foil (25μm thickness and purity 99.45%), Lithium foil, (0.75×19mm, 99.9%) and polypropylene separator celgard®2400:thickness:25 μm), Bis(trifluoromethyl sulfonyl)imide lithium salt (LiTFSI; 98+%), lithium nitrate ($LiNO_3$; anhydrous, 99.999%), 1,2-dimethoxyethane (DME; 99+%), 1,3-dioxolane (DOL; 99.5%) were purchased from Alfa Aesar and used without further purification for the preparation of 1M LiTFSI as the electrolyte. The ball milling was suspended for 20 min after every 1 h of milling to cool

down the milling system. The mixed slurries were dried on a hot plate at 100 ℃ overnight and pulverized thoroughly using a motor and pestle. The powder was screened using a mesh of 150 μm size to obtain a fine powder of almost uniform particle size. The powder was pre-calcined at 850 ℃/4 h, followed by thorough pulverization and calcined at 1150 ℃ 2 h at a ramp rate of 5 ℃/min. The sulfur (S), BS1T, carbon black (CB) and PVDF were mixed. The slurry of S/BS1T/CB/PVDF composite was prepared in NMP via ball milling and coated on aluminum foil of thickness (25μm) via doctor blade. After drying in vacuum oven (40 ℃) till 15 hrs. electrodes were cut into disc of 13 mm for cathode. The polypropylene (PP) separator (Celgard®2400) was used. The coin cells (CR2032) were assembled in an Ar-filled glove box (MBraun, USA) with H_2O, and O_2 <0.1ppm.

5.4 Characterization

The X-ray diffraction (XRD) measurements were carried out using a Rigaku Smart Lab X-ray diffractometer equipped with CuKα radiation (λ = 1.5418 Å) operated in a Bragg-Brentano (θ–2θ) geometry at 40 kV and 44 mA. The crystal structure and phase purity of the compounds were checked in a slow scan mode using a 2θ step size of 0.05^0. The analyses of the XRD patterns were carried out using FullProf suite software 7.70 (Version April 2022). Raman spectroscopy studies were carried out employing a HORIBA Jobin Yvon micro-Raman spectrometer (model: T64000) equipped with a 50× long working distance objective lens in a back-scattering geometry (2θ = 180^0) using a 514.5 nm line of an Ar+ ion laser (Coherent, Innova 70-C). Raman spectra with improved signal-to-noise ratio were measured by optimizing the laser power and acquisition time.

The surface morphology of the crack-sintered pellets was studied using scanning electron microscopy (SEM) (model: JEOL/MP) equipped with a backscattered electron

detector operating at an accelerating voltage of 20 kV and 3300X magnifications. SEM-based energy dispersive X-ray spectra (EDS) (model: JSM-IT500HR-JEOL) were measured from the crack surface of the sintered pellets to infer their chemical compositions. Galvanostatic charge-discharge curves were measured using MTI battery tester at different current densities within the voltage range 1.5-3.2 V (Vs Li^+/Li). The cyclic voltammetry @ 0.1mV/s was used for the testing of cycling performance and stability of the cathode material. Electrochemical impedance spectroscopy (EIS) was performed on symmetric cells using an Arbin-32MTS Pro battery tester at open circuit potential (OCP) with a signal amplitude of 10 mV, in a frequency range from 1 MHz to 50 Hz.

5.5 Results & discussion

5.5.1 X-ray diffraction

Figure 5.1. shows the XRD spectra of carbon black, $Ba_{0.9}Sr_{0.1}TiO_3$, sulfur and $S_{40}BS1T_{40}CB_{10}PVDF_{10}$ composites. All the diffraction peaks of $S_{40}BS1T_{40}CB_{10}PVDF_{10}$ composite are assigned to perovskite type structure of $BaSrTiO_3$ (JCPDS# 01-074-1296) indicating no significant change between $BaSrTiO_3$ and $S_{40}BS1T_{40}CB_{10}PVDF_{10}$ composites. A low content of sulfur and carbon black in between 10^0 to 26^0 is observed. However, variation in the intensity of peaks indicates the lack of long-range order due to sulfur confinement into carbon and BS1T. The size of sulfur particles is ~20–25 nm, and that of carbon is 30–40 nm, as estimated from the Scherrer formula [11-13].

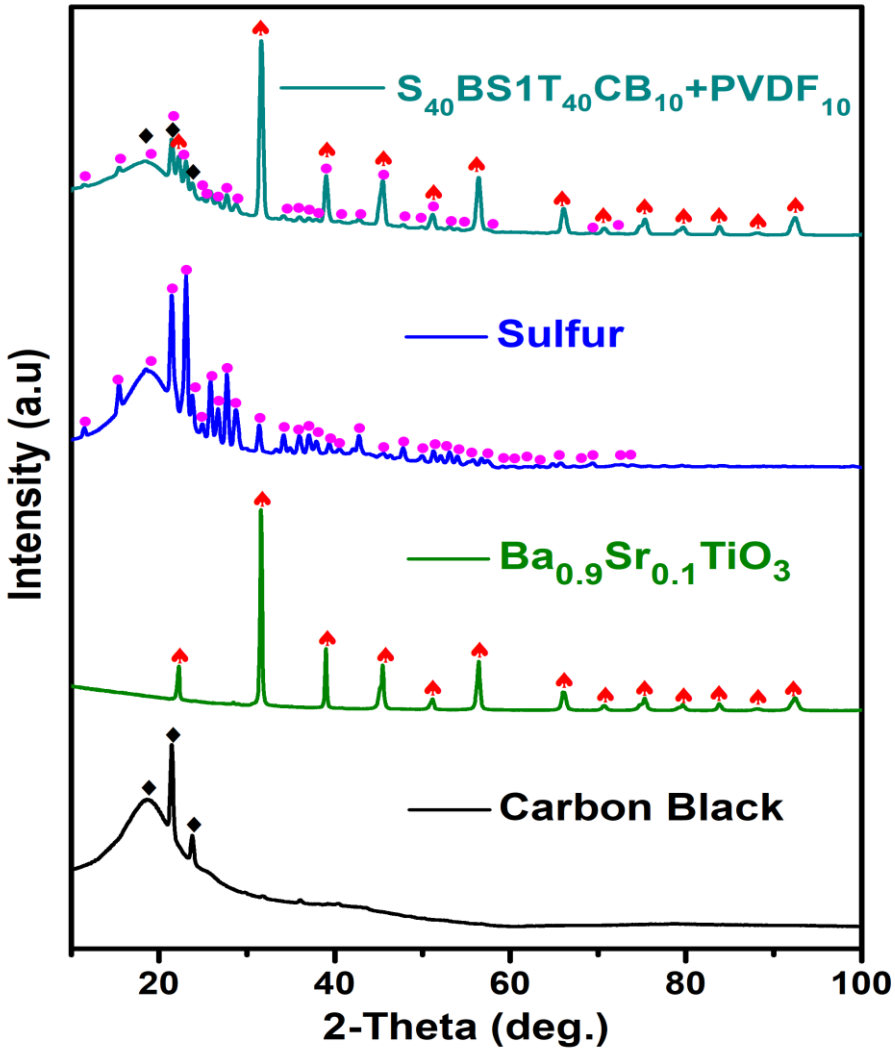

Figure 5.1. *X-ray diffraction spectra for carbon black, $Ba_{0.9}Sr_{0.1}TiO_3$, sulfur and $S_{40}BS1T_{40}CB_{10}PVDF_{10}$.*

5.5.2 Raman analysis

Figure 5.2 shows Raman spectra for sulfur, $Ba_{0.9}Sr_{0.1}TiO_3$ and $S_{40}BS1T_{40}CB_{10}PVDF_{10}$ composite, which exhibited signals corresponding to sulfur and layered carbons and composite particles. The D-band at 1350 cm^{-1} refers to the defects and disorder of the carbon structure, while the G-band at 1568 cm^{-1} corresponds to the presence

of sp^2 hybridized carbon like structure of graphene [14]. Raman signals for sulfur and BST are shown in the inset of Figure 5.2. The peaks observed in Raman spectrum of sulfur are located at 42 cm^{-1}, 165 cm^{-1} and 220 cm^{-1} showing characteristics of S_8 bending where sulfur atoms oriented.

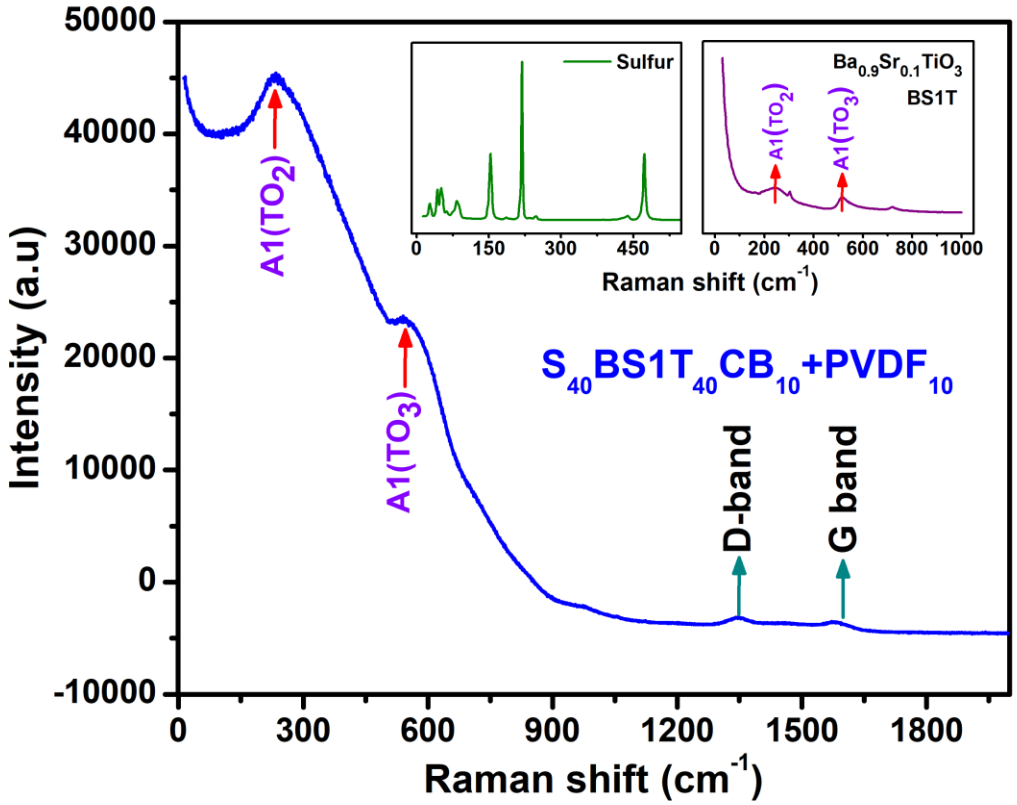

Figure 5.2. *Raman spectra for sulfur, $Ba_{0.9}Sr_{0.1}TiO_3$ and $S_{40}BS1T_{40}CB_{10}PVDF_{10}$ composites.*

5.5.3 Ferroelectric polarization (P-E)

Figure 5.3 shows ferroelectric polarization (P-E) hysteresis loop for $Ba_{0.9}Sr_{0.1}TiO_3$ composite. Normally ferroelectric materials induce permanent dielectric polarizability [15] via which suppression of polysulfide intermediates is expected. The ferroelectric characteristics, for pristine BS1T with a remnant polarization (Pr) of 14.7 µC/cm^2. The

spontaneous polarization induced by ferroelectric materials provide an internal electric field and increases chemisorption with heteropolar reactive [16].

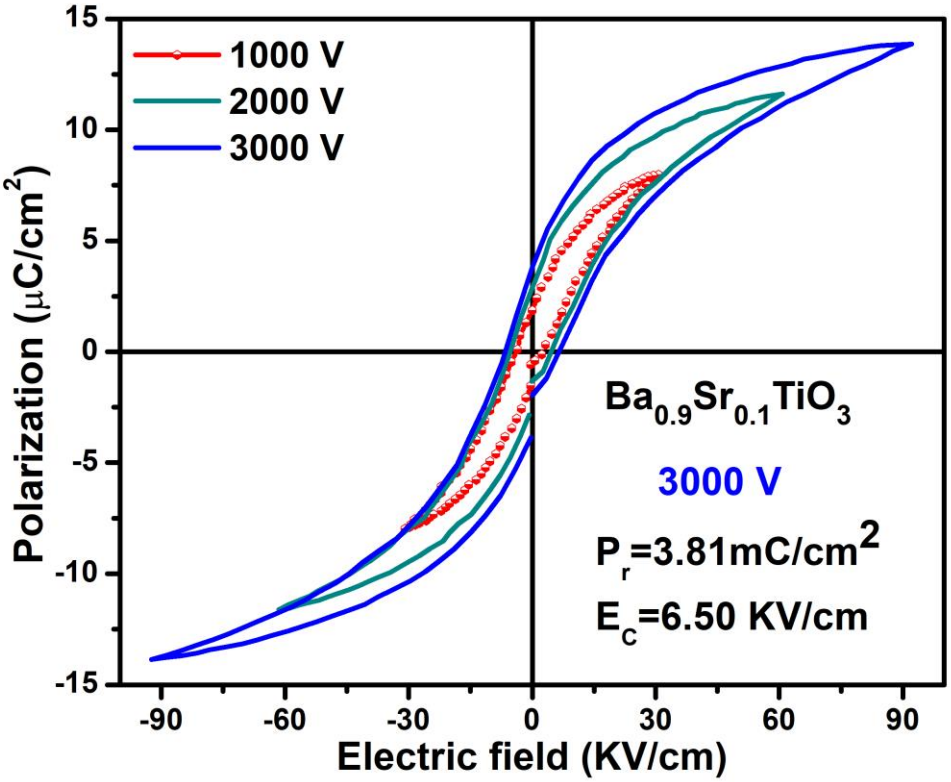

Figure 5.3. *Ferroelectric (P–E) hysteresis loop for $Ba_{0.9}Sr_{0.1}TiO_3$ composite.*

5.5.4 SEM analysis

Figure 5.4 show SEM images & EDAX spectra for pristine $Ba_{0.9}Sr_{0.1}TiO_3$(BS1T), sulfur and $S_{40}BS1T_{40}CB_{10}PVDF_{10}$, composites respectively. It has been observed that sulfur serves as glue like particles and in this case, the BS1T particles are uniformly distributed throughout the composite network intercalated with carbon black [17]. Carbon black partially embeds in the sulfur and the remainder wraps around the sulfur matrix as a protective layer [18]. This network structure showing the close contact between conductive carbon black and sulfur, may be an excellent electron pathway for insulating sulfur and adsorption sites for soluble polysulfides.

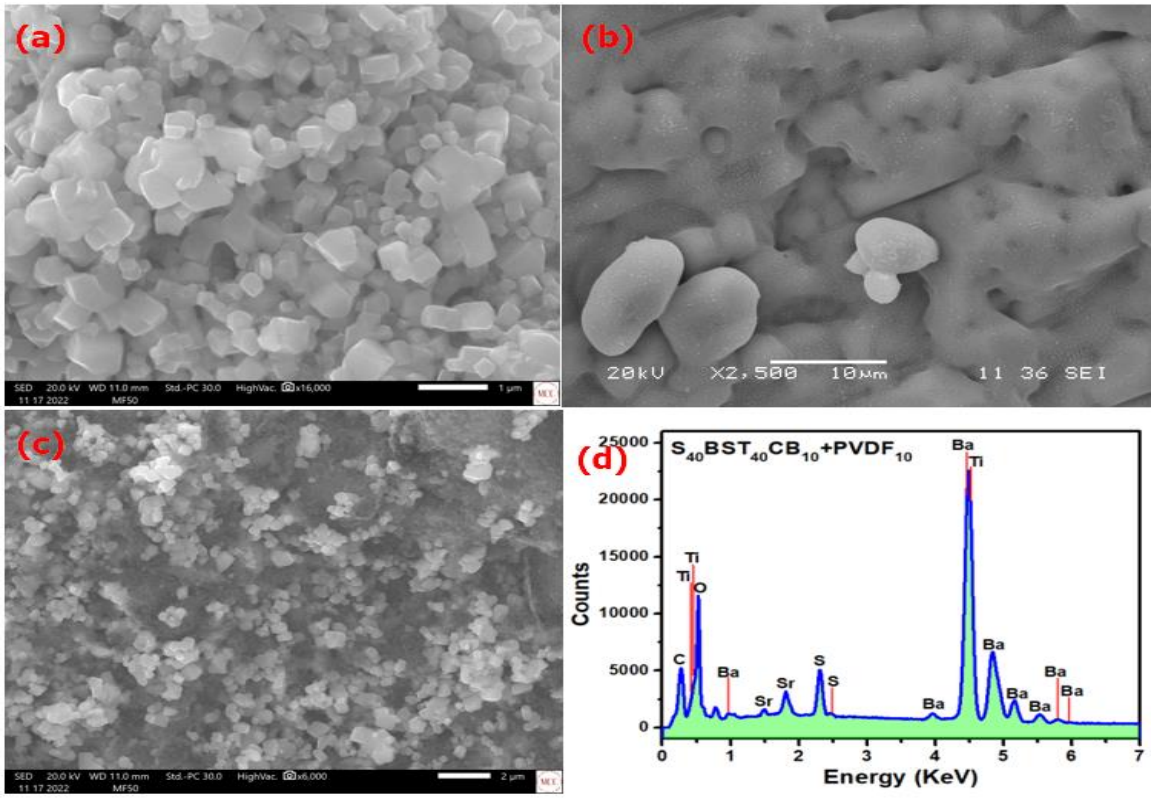

Figure 5.4. *SEM images of (a) $Ba_{0.9}Sr_{0.1}TiO_3$(BS1T), (b) Sulfur, (c) $S_{40}BS1T_{40}CB_{10}PVDF_{10}$ and (d) EDAX spectrum of $S_{40}BS1T_{40}CB_{10}PVDF_{10}$ composites.*

5.6 Electrochemical performance

Figure 5.5.(a-d) show charge-discharge**,** cycling profiles, cyclic voltammetry response and EIS spectra for S/BS1T/CB/PVDF composite cathodes @ 100 mA/g using commercial separator (PP). The observed specific discharge capacity for intercalation of BST (40wt%) in the S/BS1T/CB/PVDF composite cathode at 1st cycle is 1080 mAh/g and 395 mAh/g after 100th cycle. It has been found that when spontaneous polarized BST particles are added into the cathode, the dissoluble heteropolar polysulfides are most likely absorbed around the nanoparticles due to the induced internal electric field, attributes the control of reactions from S_8 to Li_2S_2 or Li_2S_4 , also the strong polarization of the ferroelectric nanoparticles influences distribution of Li-ions, yielding diffusion pathways

in the electrolyte/active material, which accelerates the transfer speed of Li-ions, might eliminating the concentration gradient of Li-ions near to the deposition surface. Thus, the internal electric field of the ferroelectric BS1T particles, played an important role to inhibit LiPSs shuttling leading to an improvement of the cycle stability of Li-S batteries. Fig.5.5(c), shows cyclic voltammetry (CV) curve for $S_{40}BS1T_{40}CB_{10}PVDF_{10}$ composite cathode after charge-discharge @0.1mV/s. Generally, in Li-S batteries cathode materials before and after cycling show two reduction peaks, in which higher one corresponds to the transformation of elemental sulfur (S_8) into long chain polysulfides (Li_2S_n, n>4) and the lower one belongs to the conversion of long-chain polysulfides into short chain polysulfides ((Li_2S_n, n<_4) as well as the end product of lithium sulfide (Li_2S) [19]. It has been observed that the composite cathode of $S_{40}BS1T_{40}CB_{10}PVDF_{10}$ shows oxidation peak at 2.5 V & 2.66V however reduction peaks are in between 2.0V & 2.3V. The alteration in the kinetics might be due to ferroelectric nanoparticles coupling & reversible transformation of Li_2S to short/long chain LiPSs and finally to S_8 [20].

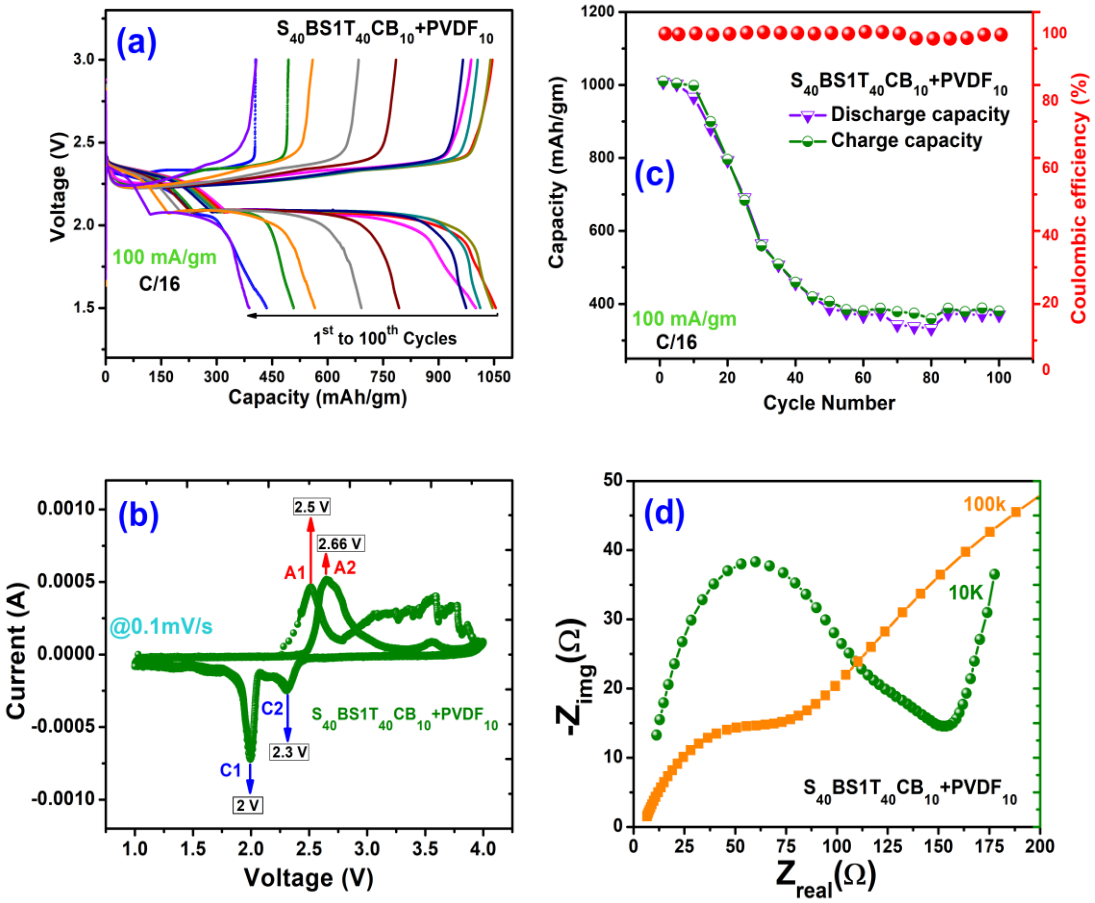

Figure 5.5. *Electrochemical performance of $S_{40}BST_{40}CB_{10}PVDF_{10}$ (a) charge-discharge profiles (b) cycling voltametric response (c) Coulombic efficiency (d) Electrochemical impedance spectroscopy (Nyquist plots).*

Figure 5.5 (d) showing the Nyquist plots of $S_{40}BS1T_{40}CB_{10}PVDF_{10}$ composite cathode. Electrochemical impedance spectroscopy (EIS) was performed on symmetric cells of $S_{40}BS1T_{40}CB_{10}PVDF_{10}$ using an Arbin-32MTS Pro battery tester at open circuit potential (OCP) with a signal amplitude of 10 mV, in a frequency range from 1 MHz to 50 Hz. In the case of symmetric cells with the positive and blocking electrodes, We have confirmed that the active material, does not contribute to the resistance of the positive electrode, however due to inclusion of BS1T up to 40 wt.% and following RC(R)W circuit

model the interfacial parameters observed are as Rs (19.48Ω) C=5.47 μF R_{ct} (73.49Ω) and W(0.0221) showing the improved diffusion pathways for Lithium ions [21].

5.7 Conclusions

In summary, Perovskite based metal oxide ($BaSrTiO_3$) is an active additive material to modify sulfur cathode due to its high conductivity, spontaneous polarization, and redox properties. X-ray diffraction spectra of composite cathodes show an orthorhombic structure with particle size distribution of 20-26 nm, while Raman spectra substantiate efficient intercalation of BST with S/CB/PVDF composites. The surface morphology as observed from SEM images, showing interconnected network of composites, however spontaneous polarization observed from (P-E) hysteresis curves of BS1T composite is ~ 14.70 μC/cm^2. The Li-S batteries fabricated based on optimized hybrid cathodes like $S_{40}BS1T_{40}CB_{10}PVDF_{10}$ composite tested @100 mA/g showing specific capacity ~ 1080 mAh/g and retention up to 395 mAh/g after 100 cycles. The improvement and stability in capacity attributing the suppression of polysulfides via effective spontaneous polarization provided by the BS1T ferroelectric nanoparticles. It is suggested that the role of ferroelectric nanoparticles embedded in the cathode induces internal field, which controls the polysulfides formation as an adsorption center due to BS1T intercalated cathode in such batteries. It is also suggested that BS1T doped cathode microscopically render dipoles permanently polarized due to which polysulfides exposure to the electrolyte will be minimal. This strategy via inducing ferroelectric polarization within the cathode provides an opportunity and promising solution to control polysulfides formation and achieve improved capacity in the high energy Li-S batteries.

5.8 References

[1] P.G. Bruce, S.A. Freunberger, I.J. Hardwick, J.M. Tarscon, *Nat. mater.* **11,** 19(2011).

[2] A. Manthiram, Y.Z. Fu, S.H. Chung, C.X. Zu, Y.S. Su, *Chem. Rev.* **114**,11751(2014).

[3] X.B. Liu, Y.C. Liu, M. Feng, L.Z., Fan, J. Mater., *Chem A* **6**, 23621(2018).

[4] Z. Wang, M. Feng, H. Sun, G. Li, Q. Fu, H.B. Li, J. Liu, L.Q. Sun, A. Maugerd, C.M. Juliend, H.M. Xie, Z.W. Chen, *Nano Energy* **59**, 390(2019).

[5] G. Li, S. Wang, Y. Zhang, M. Li., Z. Chen., J. Lu., *Adv. Mater*. **30**, 1705590(2018).

[6] S.S. Zhang, *J. Power sources* **231**, 153(2013)153.

[7] J. Wang, B. W. van Eerd, T. Sluka, C. Sandu, M. Cantoni, X. K. Wei, A. Kvasov, L. J. McGilly, P. Gemeiner, B. Dkhil, A. Tagantsev, J. Trodahl, N. Setter, *Nat. Mater.* **14**, 985(2015).

[8] M. R. Morris, S. R. Pendlebury, J. Hong, S. Dunn, J. R. Durrant, *Adv. Mater.* **28**, 7123(2018).

[9] Y. Cui, J. Briscoe, S. Dunn, *Chem. Mater.* **25**, 4215(2013).

[10] B. Tripathi, R.K. Katiyar, Morell, A. Dixit, Ram S Katiyar, *Energies* **14**, 8362(2021).

[11] S. Zheng, P. Han, Z. Han, H. Zhang, Z. Tang, J. Yang, *Sci. Rep*. **4**, 4842(2014).

[12] B. Zhang, *Energy Environ. Sci*. **3,** 1531(2010).

[13] C.P.P. Wong, C.W. Lai, K.M. Lee, G.T. Pan, C.M. Huang, T.C.K. Yang, J.C. Juan, Jr. *Electrochemical Society* **168**, 080530(2021).

[14] Z. Zhang, G.C. Wang, Y.Q. Lai, J. Li, Z.Y, W. Zhang Chen, *J. Power sources* **300**, 157(2015).

[15] G.H. Haertling, *J. Am. Ceram. Soc*. **82**, 797(1999).

[16] D. Marmorstein, T.H. Yu, K.A. Strivel, F.R. Mc Larnon, J. Hou, *E.J. Cairns, J. Power Sources* **86**, 219(2000).

[17] H.J. Peng, G. Zhang, X. Chen, Z.W. Zhang, W.T. Xu, J.Q. Huang, Q. Zhang, *Angew. Chem*. **55,** 12990(1995).

[18] S. Li, T. Mou, G. Ren, J. Warzywoda, B. Wang, Z. Fan, *ACS Energy Lett* **2,** 481(2016).

[19] Y. Wang, Z. Wan, F. Zheng and Li Lu, *Advance. Science* **9**, 2105849(2022).

[20] Y Tian, G. Li, Y. Zhang, D. Luo, X. Wang, Y. Zhao, H. Liu, P. Ji, X. du, and J. Li, *Ad. Mater.* **20,** 1904876(2019).

[21] P. Vyroubal, T. Kazda, *Journal of Energy storage* **15**, 23(2018).

CHAPTER 6

Highlights and perspective

6.1. Overview

Sr-substituted BST_x (x=0.1, 0.3, and 0.7), dense polycrystal samples were prepared by the solid-state reaction method. Generating change in the perovskite structure ABO_3, the tetragonal anisotropy (c/a ratio) reduces with increasing Sr-substitution and approaches unity for x=0.7. Upon increasing Sr-content, a gradual reduction in the band gap of these compounds is found. Ferroelectric measurement on BST_x capacitors revealed a well-defined ferroelectric loop for x = 0.1 and 0.3, and relaxor behavior (slim loop) for x = 0.7. A recoverable energy density U_{dis} of ~19.5 J/cm^3 with an energy storage efficiency η of ~ 88% for an applied electric field of around 10.8 MV/cm. The present results on ferroelectric BST_x capacitors exhibit multifunctional properties with future perspectives leading to multifunctional properties whit useful for several energy storage applications. [1]

Polycrystalline $Ba_{0.7}Sr_{0.1}TiO_3$ (BS1T) ferroelectric nanoparticles doped in S/CB composite cathodes were prepared using a high energy ball milling and the solid-state reaction method. Ferroelectric polarization studies suggested the highest polarization of is ~14.58 μC/cm^2 for BS1T. The Li-S batteries fabricated based on optimized hybrid cathodes like $S_{50}BS1T_{30}CB_{10}PVDF_{10}$ & $S_{60}BS1T_{20}CB_{10}PVDF_{10}$ composites tested @100 mA/g & 200 mA/g with polypropylene (PP) separator showing specific capacities ~ 820 mAh/g & ~540 mAh/g respectively, with improved capacity retention up to 60%. And cathodes like $S_{40}BS1T_{40}CB_{10}PVDF_{10}$ composites tested @ 50 mA/g, 100 mA/g & 200 mA/g showing specific capacities ~1100 mAh/g improved capacity retention up to 70%. The improvement

in capacity retention is attributed to the suppression of polysulfides via effective spontaneous polarization provided by the ferroelectric nanoparticles. It is suggested that the role of ferroelectric nanoparticles embedded in the cathode controls the polysulfides formation as an adsorption center due to BS1T doped cathode in such batteries.

6.2. Perspective

6.2.1. Energy storage density in lead-free ferroelectric $Ba_{1-x}Sr_xTiO_3$ thin films capacitor.

Structure, phonon, and energy storage density in Sr^{2+}-substituted lead free ferroelectric $Ba_{1-x}Sr_xTiO_3$ (BST_x) thin films for x = 0.1, 0.3, and 0.7, prepared using RF sputtering techniques. Were investigated using x-ray diffraction, Raman, and ferroelectric polarization measurements as a function of temperature. The film is tetragonal for x =0.1 with large c/a ratio. The tetragonal anisotropy decreases upon increasing x, and it turns cubic for x > 0.3. All these structural and ferroelectric properties change due to change in the c/a ratio. Temperature dependent Phonon spectroscopy results (80-500 K) indicate decrease in tetragonal to cubic phase transition temperature upon x due to reduction in anisotropy. Overdamping of ~90 cm^{-1} E soft phonon mode and dramatic decrease of the intensity of ~160 cm^{-1} A-mode were observed around the tetragonal ferroelectric to cubic paraelectric phase (< 300 K). The energy storage density of these thin film capacitors was estimated using the measured polarization hysteresis loops and were compared. For x = 0.7, a larger energy storage density (U_{re}) ~29 J/cm^3 with efficiency of ~48 % was estimated at an applied voltage of 1.1 MV/cm. Nearly room temperature transition temperature T_c, larger dielectric constant, and high energy density values of our BST_x thin film capacitors indicate its possible application in high energy storage devices.

The preliminary results obtained show that the BST_x can be used for ultrahigh energy storage performance of Lead-free oxide multilayer film capacitor via interface engineering.[2] The importance of dielectric materials as capacitors have been extensively investigated in recent decades and will surely be further explored in the future for their potential capabilities for charge control and electrical energy storage and applications in advanced electrical and electronic systems. [3,4] Los capacitores de material dieléctrico para peliculas delgadas, para almacenamiento de energía dieléctrica han atraído una mayor atención debido a su velocidad de carga/descarga extremadamente alta y, por lo tanto, la densidad de potencia más alta entre los dispositivos de suministro y almacenamiento de energía eléctrica. [5] Most importantly, energy storage density, efficiency and thermal stability are the three key parameters for the performances of energy storage materials. By far, the majority of investigations on film capacitors have been focused on the properties at room temperature (RT).[6]

6.2.2. Anode Ba doped $SrTiO_3$ perovskite as anode for Li-ion batteries

In this study we are reporting the electrochemical performance of $Ba_{0.9}Sr_{0.1}TiO_3$ (BS1T) having polarization of 14.58 $\mu C/cm^2$ as an anode for Li-ion batteries. Perovskite structure (ABO_3) anode materials have received much attention because of their mixed electronic and ionic conduction behaviours that make the triple-phase boundary (TPB) extend to the entirely exposed anode surface. Among the variety of these oxides, $SrTiO_3$-based perovskite compounds are promising Ni-free anode candidates due to their high chemical stability at high temperatures under both oxidizing and reducing atmospheres, and strong resistance to carbon deposition. X-ray diffraction spectra confirm tetragonal symmetry (c/a=1.0073), Raman spectroscopic study confirms Raman modes ($A_1(TO_1)$,

$A_1(TO_2)$, $A_1(TO_3)$ and $A_1(LO_3)$) of the tetragonal orientation for BS1T. SEM images confirm homogeneous surface of BST having grain sizes (1-1.5 μm). Carbon black was used as the conductive additive PVDF as binder, $LiPF_6$ as an electrolyte for charge-discharge performance and contribution to the electrochemical properties of the cell in terms of lithium intercalation and de-intercalation. At slow discharge rate, a capacity of approximately 240 mAh g^{-1} achieved. It is found that Ba on $SrTiO_3$ surface helps to facilitate electron transfer thereby improving the capacity and rate performance of BS1T as Li-ion battery anode material.

These results show us that the BS1T is applicable for the development of lithium-ion batteries. For improving the negative electrode of lithium metal has serious problems as secondary battery use, since it does not have a long enough cyclic life and their safety aspects that need to be considered due to the dendrite formation on the surface of lithium metal electrode during charge/discharge cycles. To solve these problems a locking-chair concept has established, in which the intercalation phenomena has used as an anode reaction for lithium-ion secondary batteries. [7,8]

6.3. Synthesis

6.3.1. Thin films prepared using RF-sputtering deposition technique.

Insulators cannot be sputtered with standard DC glow discharge techniques because the accelerating potential cannot be directly applied and because the positive charge which accumulates on the surface during ion bombardment cannot be neutralized. Direct sputtering of insulators can be achieved by applying a high-frequency potential to a metal electrode behind the dielectric target. This technique was used to deposit thin insulating films. [9] Obtained BST_x films prepared by sputtering on Pt/TiO_2 /SiO_2 /Si substrates are

found to exhibit a capacitance change ~tunability! of nearly 4:1. Higher tunability has been attributed to the ~100% texturing of the BST_x films and is a result of the biaxial tensile stress imposed by Si on BST_x making the polar axis oriented in plane. [10]

6.3.2. Anode high-energy ball milling and solid-state reaction method.

The SCB/BS1T composite for the anode is obtained by a high energy ball milling method, ball milling is performed at 500 rpm for 10 hours. To obtain homogeneous nanometric order particles.[11] The composite obtained presents excellent characteristics to prepare the anodes for high energy density lithium-ion batteries.

6.3.3. Emerging applications

Solid-state dielectric capacitors, which store energy electrostatically, have attracted much attention recently due to their ultrafast charging-discharging speed and high-power density among all currently available electrical energy storage devices. [12] Capacitors with high energy storage density can be used widely in various fields, such as pulsed power systems, hybrid electric vehicles and high-frequency inverters. [13]

Anode-free solid-state lithium batteries are promising for next-generation energy storage systems, especially the mobile sectors, due to their enhanced energy density, improved safety, and extended calendar life. However, the inefficiency of lithium plating and stripping leads to rapid capacity degradation due to the absence of excess lithium inventory. [14]

6.4. Closing remarks

BST_{1-x} ceramics are widely studied ferroelectric materials with tunable ferroelectric to relaxor ferroelectric transition temperature by varying of Ba/Sr ratios. BST_{1-x} is a continuous solid solution of $BaTiO_3$ and $SrTiO_3$ over the entire range of concentrations. Functionally graded BST_{1-x} ceramics with a series of Ba/Sr ratios [1], are investigated, to further reduce the temperature coefficient and extend the maximum efficiency for capacitor applications. However, the present ceramic based capacitors have too low energy densities compared to the predominant marketable batteries or double layer capacitors.

Lithium-sulfur (Li-S) batteries are considered promising candidates for next-generation battery technologies, as they have high energy density. However, due to the use of a solid Li-metal anode and a liquid electrolyte, the current Li-S batteries face several issues in terms of Coulombic efficiency and cycling stability, which seriously impeded their development. Work was improving the characteristics of the battery considering that polar (BST_x) substances have good affinity towards polysulfide and can provide more stable reacting environment in the cathodic site, to trap polysulfide intermediates via induced permanent dielectric polarizability. It is expected that spontaneous polarization induced by asymmetric crystal structure of ferroelectrics provide internal electric fields and increase chemisorption with heteropolar reactivity.

6.5. References

[1] I. Castillo, K.K. Mishra, R.S. Katiyar, Crystal **13**, 63(2023).

[2] Z. Sun, C. Ma, M. Liu, J. Cui, L. Lu, J. Lu, X. Lou, L. Jin, H. Wang, J. Chun-Lin, Adv. Mater. **29**, 1604427(2017).

[3] Q. Li, L. Chen, M. R. Gadinski, S. H. Zhang, G. Z. Zhang, H. Y. Li, A. Haque, L. Q. Chen, T. N. Jakson, Q. Wang, *Nature* **523**, 576(2015).

[4] K. Han, Q. Li, C. Chanthad, M. R. Gadinski, G. Z. Zhang, Q. Wang, *Adv. Funct. Mater.* **25**, 3505(2015).

[5] Y. Zhao, X. H. Hao, Q. Zhang, *ACS Appl. Mater. Interfaces* **6**, 11633(2014).

[6] P. Victor, R. Ranjith, S. B. Krupanidhi, *J. Appl. Phys.* **94**, 7702(2003).

[7] Armand MB. In: Van Gool W, editor, Fast ion transport in solids, Elsevier, 1973, p. 665.

[8] J.J. Auborn, Y.L. Barberio, J. Electrochem Soc. **134**, 638(1987).

[9] P.D. Davidse, L.I. Maissel, Journal of Applied Physics **37**, 574(1966).

[10] P. Padmini, T. R. Taylor, M. J. Lefevre, A. S. Nagra, R. A. York, J. S. Speckb, Applied Physics Letter **75**, 3186(1999).

[11] A. Andrade, F.E. Beltrán, S.J. Sandoval, J.G. Hernández, Scripta Materialia **49**, 773(2003).

[12] W. Zhang, Y. Gao, L. Kang, M. Yuan, Q. Yang, H. Cheng, W. Pan, J. Ouyang, Acta Materialia **85**, 207(2015).

[13] Q. Zhang, L. Wang, G. Li, Y. Liu, Journal of Energy Storage **31**, 101721(2020).

[14] W.Z. Huang, C.Z. Zhao, P. Wu, H. Yuan, W.E Feng, Z.Y. Liu, Y. Lu, S. Sun, Z. H. Fu, J.K. Hu, S.J. Yang, J.Q. Huang, Q. Zhang, Adv. Energy Materials **12**, 2201044(2022).